ROYAUME DU MAROC
Université Mohammed V
- RABAT -
جامعة محمد الخامس
– الرباط –
Faculté des sciences
كلية العلوم
CENTRE D'ETUDES DOCTORALES - SCIENCES ET TECHNOLOGIES

N° d'ordre **3609**

THESIS

To obtain the: ***DOCTORATE***

Research structure: *Laboratory of condensed matter and interdisciplinary sciences*

Discipline: *Physical Science*

Specialty: *Condensed Matter Physics and Materials Science*

Presented and defended on ***26/03/2022*** *by:*

Jihad LABROUSSE

New 2D materials computational design for hydrogen storage applications

JURY

Youssef EL AMRAOUI	*PES, National Superior School of Arts and Crafts (ENSAM), University Moulay Ismail, Meknes*	*President*
Mohammed LOULIDI	*PES, Faculty of Sciences, Mohammed V-Rabat University*	*Rapporteur/Examiner*
Ahmed HOURMATALLAH	*PES, Higher Normal School (ENS) Sidi Mohammed Ben Abdallah Fes-University*	*Rapporteur/Examiner*
Rachid BENCHRIFA	*PES, Faculty of Sciences, Mohammed V-Rabat University*	*Rapporteur/Examiner*
Abdelilah BENYOUSSEF	*PES, Hassan II Academy of Sciences and Techniques-Rabat*	*Expert Examiner*
Hamid EZ-ZAHRAOUY	*PES, Faculty of Sciences, Mohammed V-Rabat University*	*Examiner*
Abdallah EL KENZ	*PES, Faculty of Sciences, Mohammed V-Rabat University*	*Thesis director*

Academic year: 2022/2023

Faculty of Sciences, 4 Avenue Ibn Battouta B.P. 1014 RP, Rabat-Morocco

Phone: +212(0) 37 77 18 34/35/38, Fax: +212(0) 37 77 42 61, http://www.fsr.ac.ma

ROYAUME DU MAROC
Université Mohammed V
- RABAT -
جامعة محمد الخامس
– الرباط –
Faculté des sciences
كلية العلوم

Jihad LABROUSSE[1]

Supervised by

Abdallah EL Kenz[2]

New 2D materials computational design for hydrogen storage applications

[1]E-mail:jihad_labrousse@um5.ac.ma

[2]E-mail: akenzele@yahoo.com

Laboratory of Condensed Matter and interdisciplinary Sciences (LaMCScI)

Acknowledgments

This thesis was carried out at the Laboratory of Condensed Matter and Interdisciplinary Sciences (LaMCScI) of Faculty of Sciences, University of Mohammed V-Rabat, Morocco under the supervision of Prof. **Abdallah EL KENZ**.

I owe a great deal of thanks to many people for their kind help during my PhD studies. First and foremost, many thanks to my supervisor Professor **Abdallah EL KENZ** for his invaluable guidance and support on everything from theoretical work to writing thesis. He is always generous with his time providing me with many inspiring discussions and much advice. I highly appreciate that he has given me the opportunities to participate in international scientific conferences, allowing me to learn a lot from other world-leading researchers and develop network for potential collaborations.

I would also thank the thesis committee for reviewing my work and giving their insightful and useful comments. It is an honor for me that they agree to judge this work.

I wish to thank Prof. **Youssef EL AMRAOUI** from National Superior School of Arts and Craft (ENSAM), Université Moulay Ismail Meknes, to be the president of the jury members of this thesis. And for his patience in revising my papers and thesis, for providing invaluable insight and constructive criticism to the work I have done.

I would like also to offer my thanks to Prof. **Mohammed LOULIDI** from Faculty of Sciences, University Mohammed V-Rabat, for reporting and reviewing this PhD thesis.

I would like also to thank Prof. **Ahmed HOURMATALLAH** From Higher Normal School (ENS), Sidi Mohammed Ben Abdallah Fes-University, for reporting and reviewing this PhD thesis.

I would also like to extend my thanks to Prof. **Rachid BENCHRIFA** from Faculty of Sciences, University Mohammed V-Rabat, for reporting and reviewing this PhD thesis.

I would like to express my very great appreciation, deep gratitude and sincere thanks to Prof **Abdelilah BENYOUSSEF**, from the Hassan II Academy of Sciences and Techniques-Rabat, for examining this thesis and also for his indispensable practical teaching and supervision, for extended discussions and valuable suggestions which have contributed greatly to the

improvement of the thesis. I take this opportunity to thank him for all the encouragements and supports that he gave me, on my research works, on my publications.

I would like to express my thanks to Prof. **Hamid EZ-ZAHRAOUY**, from Faculty of sciences, University Mohammed V-rabat, for examining this thesis.

I am grateful for the assistance offered by member of the hydrogen materials group: **Khalid BELASFAR**, from Faculty of sciences, University Mohammed V-rabat, for his useful discussions, contributions, and friendship.

Personal thanks and love to my family that supported me during these three years. Without their love and support I could never have achieved everything that I have in life.

Abstract

Hydrogen provides a clean, abundant, and most energy-efficient fuel without emissions when operated in a fuel cell or combustion engine, making it an ideal fuel. Nevertheless, hydrogen's enormous potential remains unrealized, mainly because of the problems associated with hydrogen storage and production on a commercial scale. There are many ways to store hydrogen, carbon-based materials being one of them, we chose to improve the transport, electronic and storage properties of graphene by building compact structures with graphene sheets. Physisorption of H_2 molecule on BC_7, BC_3, AlC_3, ZnC_3, and GeC_3, shows a large gravimetric capacity of 10.40 wt%, 10.51 wt%, 11.8 wt%, 7.73 wt% and 7.25 wt%, respectively. The hydrogenation/dehydrogenation (desorption) temperature for the previous surfaces was found as 177.00 K, 205.33 K, 173.35 K, 215.55 K, 224.25 K, respectively. The H_2 molecule desorption temperatures and gravimetric capacity indicates that the monolayers BC_7, BC_3, AlC_3, ZnC_3, and GeC_3 might work as a hydrogen reversible storage substrate. Hence, the findings reveal the previous substrates monolayers to be a prospective, effective, reversible and great gravimetric capacity for storing H_2 in feasible conditions.

Keywords : Monolayer, Hydrogen adsorption, First-principles calculation, Desorption temperature, Gravimetric capacity, Activation energy.

Résumé

Lorsqu'il est utilisé dans une pile à combustible ou un moteur à combustion, l'hydrogène est un combustible propre, abondant et très efficace sur le plan énergétique, sans émissions, ce qui en fait un combustible idéal. Néanmoins, l'énorme potentiel de l'hydrogène reste inexploité, principalement en raison des problèmes liés au stockage et à la production d'hydrogène à l'échelle commerciale. Il existe de nombreuses façons de stocker l'hydrogène, les matériaux à base de carbone étant l'une d'entre elles, nous avons choisi d'améliorer les propriétés de transport, d'électronique et de stockage du graphène en construisant des structures compactes avec des feuilles de graphène. La physisorption de la molécule d'H_2 sur BC_7, BC_3, AlC_3, ZnC_3, et GeC_3, montre une grande capacité gravimétrique de 10,40 % en poids, 10,51 % en poids, 11,8 % en poids, 7,73 % en poids et 7,25 % en poids, respectivement. La température d'hydrogénation/déshydrogénation (désorption) pour les surfaces précédentes a été trouvée à 177,00 K, 205,33 K, 173,35 K, 215,55 K, 224,25 K, respectivement. Les températures de désorption des molécules d'H_2 et la capacité gravimétrique indiquent que les monocouches BC_7, BC_3, AlC_3, ZnC_3 et GeC_3 pourraient fonctionner comme des substrats de stockage réversible de l'hydrogène. Par conséquent, les résultats révèlent que les monocouches de substrats précédentes constituent un moyen prospectif, efficace, réversible et de grande capacité gravimétrique pour le stockage de l'hydrogène dans des conditions réalisables.

Mots clés : Monocouche, adsorption d'hydrogène, calcul des premiers principes, température de désorption, capacité gravimétrique, énergie d'activation.

Résumé détaillé

En raison de la quantité limitée de combustibles fossiles et de ses effets sur le climat et l'écologie, l'exploration de sources d'énergie alternatives, propres, abondantes et durables devient une priorité mondiale. Bien que les énergies renouvelables, notamment l'énergie solaire, l'énergie éolienne et l'hydrogène, aient la capacité de satisfaire la demande énergétique actuelle, il reste à identifier des matériaux capables de stocker et/ou de transformer l'énergie de manière efficace et bon marché. L'hydrogène apporte une réponse soignée au creuset de l'environnement. En tant que vecteur énergétique très polyvalent, l'hydrogène est capable de fournir une option énergétique propre, complète, intégrée, multisectorielle et à faible coût pour contribuer à résoudre le problème environnemental et assurer l'avenir énergétique de la Terre. Néanmoins, l'adoption massive de l'hydrogène économique a été lente en raison d'une motivation insuffisante et des défis techniques liés au stockage de l'hydrogène. L'objectif de cette thèse aillait d'améliorer les conditions de stockage de l'hydrogène dans les matériaux à base de carbone, en particulier les matériaux à base de graphène. Selon la littérature, il est mentionné que, dans le département de l'énergie des États-Unis (DOE), pour que le stockage de l'hydrogène soit efficace au niveau industriel, l'énergie de liaison appropriée de l'hydrogène doit être comprise entre 0,2 eV et 0,6 eV pour chaque molécule d'hydrogène. Par conséquent, le graphène n'est pas un réservoir approprié pour les applications de stockage d'hydrogène en raison de la faible énergie de liaison qui se situe hors de la plage de 0,2 et 0,6 eV/H_2. Dans le cas de la physisorption, la VD (densité volumétrique) dépend de la possibilité de construire des structures compactes avec le graphène pour améliorer les chances d'être un candidat pour le stockage de l'hydrogène. Dans les premiers calculs, nous avons examiné la physisorption de la molécule H_2 sur la structure BC_7 par des calculs de premiers principes, nous avons trouvé que l'énergie d'adsorption d'Eads était proche de - 0.2081 eV, où la distance avec la plus grande stabilité est de 3.40 Å. L'adsorption de la molécule H_2 à différentes configurations de la structure BC_7 a conservé son comportement métallique. L'étude des chemins de diffusion entre les différentes configurations a révélé la capacité de la molécule d'hydrogène à se transmettre entre les sites, qui sont séparés par une faible barrière énergétique de 0,0022 eV. Il a été démontré que la couche de BC_7 peut adsorber 11 molécules de H_2, avec une capacité gravimétrique de 10,40 % en poids. La température d'hydrogénation/déshydrogénation (désorption) a été trouvée à 177,00 K. Les températures de désorption des molécules d'H_2 et la capacité gravimétrique indiquent que la monocouche BC_7 pourrait fonctionner comme un

substrat de stockage réversible de l'hydrogène. Par conséquent, les résultats révèlent que la monocouche BC_7 est un substrat de stockage d'hydrogène prospectif, efficace, réversible et de grande capacité gravimétrique dans des conditions réalisables. Nous avons effectué les mêmes calculs sur la surface de BC_3, il en ressort que l'énergie d'adsorption est d'environ - 0,3150 eV, alors que 3,10 Å est la distance stable la plus proche. Le calcul de la densité d'état montre que lors de l'adsorption de molécules de H_2 sur la surface de BC_3, celle-ci conserve son comportement semi-conducteur avec les deux méthodes : la méthode Marzarie Vanderbilt et la méthode Tetrahedron. Une étude des chemins de migration entre les différentes positions a montré la capacité de la molécule d'hydrogène à diffuser entre les positions, séparées par une petite barrière d'énergie s'élevant à 2,25 meV. Il a été démontré que la feuille de BC_3 possède la capacité d'adsorber 11 molécules d'hydrogène, avec une capacité gravimétrique de 10,51 % en poids, avec une température de désorption de 205,33 K. Selon les résultats, la feuille de BC_3 peut être une perspective très intéressante pour le stockage de l'hydrogène. Nous avons également étudié l'adsorption de la molécule d'hydrogène sur la monocouche d'AlC_3 à l'aide de calculs de premier principe, les calculs montrent que l'énergie d'adsorption Eads était d'environ -0,2189 eV, où la distance la plus stable était de 2,50 Å. L'adsorption de la molécule d'hydrogène à différentes positions sur la surface d'AlC_3 a maintenu son caractère semi-conducteur. L'examen des chemins de diffusion entre les différents sites a indiqué une capacité de la molécule d'hydrogène à migrer entre les sites, qui étaient espacés par une légère barrière énergétique de 0,0163 eV. Il a été démontré que la monocouche d'AlC_3 possède la capacité d'adsorber 16 molécules d'hydrogène, avec 11,8 % en poids de capacité gravimétrique, ainsi qu'une température de désorption de 173,35 K. D'après ces résultats, la monocouche d'AlC_3 pourrait être un candidat prometteur pour le stockage de l'hydrogène. Nous avons étudié l'interaction du substrat ZnC_3 et de la molécule H_2, les résultats ont révélé que l'énergie d'adsorption d'Eads était proche de - 0,3169 eV, où la distance avec la plus grande stabilité était de 3,30 Å. L'adsorption de la molécule H_2 à différentes configurations de la structure ZnC_3 a conservé son comportement métallique. L'étude des chemins de diffusion entre les différentes configurations a révélé la capacité de la molécule d'hydrogène à se transmettre entre les sites, qui étaient séparés par une faible barrière énergétique de 0,022 eV. Il a été démontré que la couche de ZnC_3 peut adsorber 17 molécules de H_2, avec une capacité gravimétrique de 7,73 % en poids. La température d'hydrogénation/déshydrogénation (désorption) est de 215,55 K. Les températures de désorption des molécules d'H_2 et la capacité gravimétrique indiquent que la monocouche de ZnC_3 pourrait fonctionner comme un substrat de stockage réversible de

l'hydrogène. Par conséquent, les résultats ont révélé que la monocouche de ZnC_3 est un substrat de stockage d'hydrogène prospectif, efficace, réversible et de grande capacité gravimétrique dans des conditions réalisables. Enfin, nous avons examiné la physisorption de la molécule d'H_2 sur la structure GeC_3 par des calculs de premiers principes, nous avons trouvé que l'énergie d'adsorption d'Eads était proche de - 0,3628 eV, où la distance avec la plus grande stabilité était de 3,30 Å. L'adsorption de la molécule d'H_2 à différentes configurations de la structure GeC_3 a conservé son comportement semi-métallique. L'étude des chemins de diffusion entre les différentes configurations a révélé la capacité de la molécule d'hydrogène à se transmettre entre les sites, qui étaient séparés par une faible barrière énergétique de 0,0042 eV. Il a été démontré que la couche de GeC_3 peut adsorber 17 molécules de H_2, avec une capacité gravimétrique de 7,25 % en poids. La température d'hydrogénation/déshydrogénation (désorption) est de 224,25 K. Les températures de désorption des molécules d'H_2 et la capacité gravimétrique indiquent que la monocouche de GeC_3 pourrait fonctionner comme un substrat de stockage réversible de l'hydrogène. Par conséquent, les résultats ont révélé que la monocouche de GeC_3 est un substrat de stockage d'hydrogène prospectif, efficace, réversible et de grande capacité gravimétrique dans des conditions réalisables. Grâce à cette découverte, nous avons amélioré les propriétés de transport, d'électronique et de stockage de la molécule d'hydrogène par rapport au graphène.

Contents

List of Figures

List of Tables

List of abbreviations

DoE	Department of Energy	CNTs	Carbon nanotubes
MOFs	Metal organic framework	PEM	Proton Exchange Membrane
GD	Gravimetric density	VD	Volumetric density
NEB	Nudged elastic ban	C_g	Gravimetric capacity
wt.	Weight	T_{des}	Desorption Temperature
ΔH	Formation energy	ΔS	Dehydrogenation entropy
DOS	Density of states	PDOS	Partial desnity of states
ab initio	First principal calculation	e	Charge of the electron
Ψ	Many-body wave function of electrons	k_F	Fermi wavevector
V_{ext}	External potential	$V_H(r)$	Hartree potential
$\hat{H}$	Hamiltonian operator	LDA	Local density approximation
GGA	Generalized gradient approximation	ΔE	Energies difference
DFT	Density functional theory	$\hbar$	Planck's constant devised by 2π
T	Temperature	T_b	Boiling point
T_m	Melting point	T_c	Critical temperature
PCT	Pressure-composition-temperature isotherms	p_{eq}	Equilibrium pressure
c_H	Concentration of hydrogen	SSA	Specific surface area
CAs	Carbon aerogels	AC	Activated carbon
SWCNT	Single-walled carbon nanotubes	CNF	Carbon nanofibers
MWCNT	Multi-walled carbon nanotubes	VdW	Van Der Waals
STM	Scanning tunnelling microscopy	∇^2	Laplacian operator
BO	Born-Oppenheimer approximation	$\hat{H}_{elec}$	Electronic Hamiltonian
Ψ_{elec}	Electronic wave function	E_{elec}	Electronic energy
E_{total}	Total energy	E_{nuc}	Nucleus energy
T_e	Kinetic energies of the electrons	V_{ee}	Electron electron potential
TF	Thomas-Fermi	$n(r)$	Electron density
E_{TF}	Thomas-Fermi energy	HEG	Homogeneous electron gas
m_e	Charge of the electron	$\mathcal{E}_k$	Free-electron energy state
E_{TFD}	Thomas-Fermi-Dirac energy	μ	Lagrange multiplier
HK	Hohenberg-Kohn	V_{int}	Internal potential

$s(r)$	Spin density	E_{xc}	Exchange-correlation energy
PBE	Perdew, Burke, and Ernzerhof	PW91	Perdew and Wang
PAW	Projector Augmented Waves	Φ_j , $\widetilde{\Phi}_j$, $\tilde{p}_j$	All-electron partial waves
PWSCF	Performed using the software package Quantum	QE	Quantum ESPRESSO
BZ	Brillouin zone	E_{cutoff}	Energy cutoffs
H	Enthalpy	G	Gibbs free energy
TST	Transition State Theory	RB	Reaction barrier
MEP	Minimum energy path	E_f	Formation energy
$D(\mathcal{E})$	Density of states in three dimensions	E_{ads}	Adsorption energy
E_{syteme}	Energy of the system	ρ	Charge density
E_{H_2}	Total energy of the hydrogen molecule	m	Molar masses
n	Atomic numbers	ΔE_{barr}	The diffusion barriers
$\Delta\rho$	Bader charge algorithm and the strain-charge-density distribution		

ESPRESSO opEn Source Package for Research in Electronic Structure, Simulation, and Optimization.

I dedicate this manuscript to My parents and My sisters and brother and brother’s wife.

General introduction

Energy storage: challenge and perspectives

The global human population surpassed 7.7 billion in early 2018 and is predicted to grow to 80 million annually within 2050 [1]. Human population growth is concurrently sustained by a steady growth rate of economic energy usage. In fact, the viability from both our current economic patterns as well as our overall quality of living skills are tied squarely on the capability to reach energy, a strong link is present regarding the energy supply and the overall nation's development [2]. The U.S. IEA [3, 4] indicates that the use of energy is increasing across all primary purpose industries. Nevertheless, improvements in effectiveness, which are signified by reductions in fuel intensity [5]. This shift was reinforced by a large growth in the world economy of oil, gas and coal, which satisfied the majority of the energy requirement increase. More than 70% of global energy requirement increases were served by oil, natural gas, and coal; the renewables provided nearly all of the rest [6]. The economy based on fossil fuels is being affected by unfettered greenhouse gas emissions and raw material constraints. Excessive dependence on fossil fuels for today's energy demands is causing both atmospheric pollution as well as planetary heating. Nearly 70% of CO_2 emissions growth is due to the combustion of fossil fuels such as oil, coal, and gas, with the highest contributions coming from industry and buildings [6-8]. Consequently, worldwide CO_2 emissions associated with energy have risen in 2017 by 1.4% [9], achieving a high of 32.5 Gt. This increase follows three years of emissions stabilization. In order to turn around emissions increases, all nations must elevate both the level of attenuation efforts and their ambition levels, provided pathways to decarbonization are compatible with the 1.5°C climate goals and well under the 2°C target [10]. Within the framework of enhancing the world' s answer regarding the climate change challenge, building a viable future of energy is the most significant global challenge we currently face. To achieve a successful transition to energy, forms of energy that are alternative to fossil fuels are needed. The use of renewable energies produces theoretically low levels of emissions. Specifically, renewable electricity produces minimal CO_2 emissions, in particular relative to fossil fuels like coal [11]. Therefore, this makes renewable energies a special tool in the struggle to reduce global temperature rise. As a matter of fact, renewable energies are often criticized

due to their reduced energy consumption efficiency in comparison to fossil fuels. The costs of production are also frequently regarded as greater in the near future. Most importantly, their availability is much more insecure. This requires building complicated storage systems or batteries that need a lot of extra natural energy resources and add to the environmental pollution of renewable energies. The original use of hydrogen was within the aerospace sector as a vehicle fuel. Along with other state-of-the-art technologies, research and advances in hydrogen storage, transportation and utilization in large scale projects have revealed hydrogen's potential for use as an energy vector. Today, it is viewed as an alternative future fuel to fossil fuels in general, and oil in particular, because of many factors, such as the finite offer of readily obtainable stores, national safety, as well as the impact on the environment [12]. It has potential applications in a wide variety of fields across all economic sectors, such as: electricity, industry, transportation, and buildings. Worldwide, scientists are attempting to improve the cost-effectiveness of producing, storing, transporting as well as using the fuel hydrogen for applications as varied as space heating and transportation. By 2030, the Hydrogen Council suggests that 230-250 TWh of surplus wind and solar energy might be turned over to hydrogen [13]. It proposes a potential for hydrogen to supply close to one-fifth of all energy use by 2050, reducing carbon pollution by approximately six billion tons relative to the present [13]. Furthermore, it will contribute to addressing the atmospheric pollution afflicting so many developed nations. Because of the finite amount of fossil fuels and its effects on the weather and ecology, the exploration of alternative, clean, abundant and sustainable energy sources is becoming a global priority. Although renewable energies including solar, wind and hydrogen have the ability to satisfy the current energy demand, ongoing issues remain the need to identify materials that are capable of storing and/or transforming energy efficiently and cheaply. The hydrogen provides a neat answer to the crucible of the environment. Being a highly versatile energy carrier, H_2 has the capability to provide a comprehensive, integrated, multi-sectoral, at low cost, clean energy option to help solve the environmental issue and ensure the Earth's energy future. Nonetheless, the mass adoption of economic hydrogen has been slow owing to insufficient motivation as well as the technical challenges involved in storing hydrogen. The goal of this thesis was to enhance hydrogen storage conditions in carbon-based materials, particularly graphene-based materials. Graphene has lately received enormous attention due to its many applications. Notably, graphene represents a 2-dimensional (2-D) material which is inert chemically [14]. Due to its outstanding properties in electronics, graphene became widely known. The 2-D crystalline lattice structure leads to a massless fermion-like behavior of the

electrons, where the velocity of light is substituted by a Fermi speed of about 106 m/s. Graphene electrons exhibit large mobility of charge carriers. Because of its great properties, it is considered to be a prospective material for numerous applications, for example, gas sensors, potential electrode materials and ultra-high frequency transistors. Lately, it was proven that the sorption capacity of graphene layers is more efficient compared to activated carbon [15-18]. Earlier investigations have shown some evidence that graphene can provide a suitable material for the storage of small molecules [19-21]. Employing DFT (density functional theory) calculations, Hong-ping Zhang et al. examined the interactions among a small molecule and a Ti-, Zn-, Zr-, Al- and N-doped graphene intrinsic layers [22], and discovered that the Ti-, Al-, Zr-, Zn-doped graphene layer is able of adsorbing the H_2 molecules. Milad Ghanbari et al. examined the capability of graphene as hydrogen storage by Si and/or Ge doping [23], and discovered that the Si, Ge-doped graphene is able to store a lot of hydrogen molecules. Understanding the interaction among graphene, X elements, and hydrogen would be interesting.

Research aims and scope

As soon as hydrogen has been manufactured in a cost-effective and eco-friendly manner, the issue of storing it has to be addressed. Techniques must be devised not only to transport it, but above all for storing it. The weight of hydrogen is extremely high, approximately triple compared to gasoline, yet the volume of hydrogen is extremely small, with liquid hydrogen approximately quadruple compared to gasoline. This objective is hard to reach since these physical features render it hard for large amounts to be stored safely without occupying a lot of space. In the solid storage field, several types of materials are potential for storing hydrogen. However, the advantages and disadvantages are always there, and the selection of a particular technology is based on the type of issue at hand so that the drawbacks would have less effect on the global application.

Research questions

The principal question here remains of how to efficiently store hydrogen and relocate it, what kind of storage approach works best, can hydrogen be stored safely in a hydride system?

Research Aim

Our research's objective is to develop a new carbon based 2D materials with high capacity to store hydrogen at ambient temperature and pressure. In addition, we aim to identify methods to design a high efficiency storage system using carbon based 2D materials devices and to develop strategies to achieve this goal in the future.

Specific objectives

The aim of the present work is to give a full review of the existing literature and the industrial applications related to energy storage systems based on 2D materials and to highlight the shortcomings of these systems in terms of improvement, that can be split into two parts: stress engineering and simulations. The principal aims targets are:

- Enhance the gravimetric capacities.
- Increase reversibility.
- Realization the systems Stabilization.
- Achieving the less activation energy of molecules diffusion.
- Enhancing the desorption temperature.

Structure of this thesis

The thesis consists of three chapters:

- The first chapter, referred to as a literature review, provides an overview of hydrogen storage methods, as well as the results of the comparative evaluation of hydrogen storage in carbon-based materials, particularly the construction of compact structures with graphene, to improve the possibility of being a candidate for hydrogen storage.
- The second chapter consists of a theoretical implementation using density function theory. A detailed description of the methodological code employed for this research is also provided in this chapter.
- The third chapter is devoted to the results and discussion of the research findings. We compared the BC_7 layer to graphene and discussed the characteristics of the BC_7 layer as a hydrogen storage material. We studied the interaction between the hydrogen

molecule and the XC_3 layers (X=B, Al, Zn and Ge), using the density functional theory (DFT) analysis of the first principle.

- Finally, the main conclusion gives a brief summary on our results. It includes a discussion of the impact of our findings to future research for the uses of graphene-based materials as solid-state hydrogen storage material.

Chapter I: Review on hydrogen storage investigations

1 Hydrogen storage methods

The storage of hydrogen, as outlined earlier, represents a significant key enabling mechanism to advance hydrogen and fuel cell technologies for such applications that include resort energy, mobile energy, as well as transportation. Nevertheless, the hydrogen's small density at ambient temperature results in a small amount of energy required per unit volume. Hence, it is necessary to find improved methods of storage in order to reach a greater energy density. The purpose of this section is to examine the different issues surrounding hydrogen storage and to outline the pros and cons of the various available techniques for hydrogen storage.

1.1 Hydrogen

1.1.1 History

The first chemical component listed in the periodic table is hydrogen and has the symbol H, an atomic number of 1 and the atomic weight of 1.00794. This element is the lowest in the periodic table and represents the highest abundance chemical elements in the world. Henry Cavendish found hydrogen in 1766 [24] when he mixed metals with acids. Subsequently, Antoine Lavoisier named it "Hydrogen" [1], due to its ability to convert to water when burnt. However, in 1932, Harold Urey announced the finding of a stable isotope, deuterium (^{2}H or D) whose atomic weight is 2. In natural hydrogen, this isotope is found in 0.015% [25]. A couple of years after, in 1932, an unstable isotope, tritium (^{3}H), with an atomic weight of 3, has been produced by Ernest Rutherford's group [26].

1.1.2 Hydrogen properties

The gas hydrogen does not have any color or odor. It ignites readily. When burned, it ignites with a light blue color, nearly impossible to see, the fumes being lighter than air. It can form compounds with most components and occurs naturally in water as well as in many organic compounds. The significant characteristics of both atomic hydrogen and molecular hydrogen (H_2) are summarized in **Table 1.1**.

Table 1.1: Atomic and Molecular Hydrogen properties.

Atomic Hydrogen

Atomic number	1	Atomic radius, non-bonded (Å)	1.10
Electron configuration	$1s^1$	Electron affinity (eV)	0.7542
Density (g cm^{-3})	0.000082	Ionization energies (eV	13.595
Isotopes	1H, 2H, 3H	Electronegativity (Pauling)	2.1

Molecular Hydrogen

Bond distance (Angstrom)	1H, 2H, 3H	Dissociation energy (25°C, kJ mol^{-1})	435.93
Ionization potential (eV)	15.427	Density of solid (g cm^{-3})	0.08671
Density of liquid (-252.78 °C,g cm^{-3})	0.07099	Heat of combustion to water (kJ mol^{-1})	-241.82

1.1.3 Phase diagram

Under normal conditions, hydrogen is in a gaseous state. It has one of the lowest melting and boiling points of any material. It becomes liquid under 20 K at atmospheric pressure. At such pressure, it is 800 times denser as a gas at ambient temperature. The processes for liquefying gases use quite complicated procedures combining a cold intake and adiabatic relaxation [27]. The earliest hydrogen liquefaction was achieved from Claude employing a multi-stage split cycle [28]. Initially, it is chilled from room temperature down to 230 K by means of a mechanically operated refrigeration unit, and subsequently down to 80 K by means of an exchange of liquid nitrogen. Then, the hydrogen is subjected to compression-extension processes to reduce the temperature further prior to being subjected to Joule-Thompson expansion, resulting in liquification [28]. However, other methods may be envisaged as Brayton's cycle that uses liquid helium having a lower liquefaction temperature compared to hydrogen or magneto metric cycle refrigeration. The solid state of hydrogen is located under its 259°C (14 K) melting point and at atmospheric pressure. A hydrogen phase diagram is presented **in Fig. 1.1**, showing a threefold point at -259.1°C and 0.07 bar and a critical point at -239.8°C and 13 bar. Under atmospheric pressure, the boiling point (T_b) is -253 °C and the melting point (T_m) is -259 °C. A fuel's boiling point is a critical metric since it determines the temperature up to which it needs to be chilled in preparation for storage and liquid use [28].

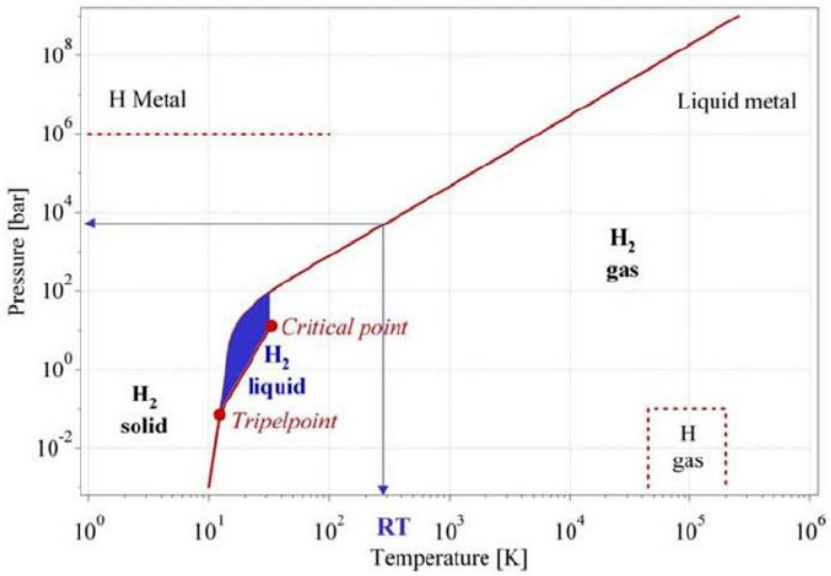

Fig. 1.1: The hydrogen primitive phase diagram.

1.2 Technical Objectives of DOE

Previous to investigating methods for hydrogen storage, a successful storage method can be defined for transportation by characterizing or quantizing the features involved in any system. Clearly, the volumetric and gravimetric elevated energy densities are compelling for use in mobile settings [29]. Currently, the most frequently occurring mobility fuels are gasoline and diesel, which can be used as a reference. These fuels have varying energy densities due to complex mixtures and different total mixtures present in the trade [30]. Nevertheless, typical values are close to 38 wt%, or 35 MJ L^{-1} [31]. Neat H_2 at room temperature and pressure provides brilliant measures but mediocre energy volumetric densities of 120 MJ kg^{-1} (100 wt%) and 0.01 MJ L^{-1}, respectively [32]. In addition, for perfect technical storage, security is significant, particularly for mainstream applications. The poisonousness, ignitability, danger of explosion or projection, etc. are not advisable. The United States Department of Energy (DOE) system goals for hydrogen Storage help guide investigators in determining the needs for the system to achieve commercial storage of hydrogen [33]. The following **Table 1.2** outlines the DOE's performance objectives for light-duty vehicle hydrogen storage systems for a range of approximately three hundred miles [34]. Such technical goals are established for 2020 and 2025. They are equivalent to existing fuel system storage in capacity, price, and operable characteristics. In terms of hydrogen reversible storage, the system gravimetric capacity is projected to be 6.5% by weight and the volumetric capacity of the system is expected to be 6.1

MJ L^{-1}. To satisfy this requirement, the key questions related to the production of the storage of hydrogen are as follows [32-35]:

- It is necessary to reduce the weight and volume of the thermal parts;
- Operating temperature range from -40 to 60°C;
- Service life of 1,500 cycles;
- Charge/discharge rate of 3 to 5 minutes.

Table 1.2: The U.S. DOE hydrogen storage system performance targets [33, 34].

Storage Parameter	**System Gravimetric Capacity (wt %)**	**System Volumetric Capacity (MJ L^{-1})**	**Cost $/kWh**
2020	4.5	2.9	10
2025	5.5	3.6	9
Ultimate	6.5	6.1	8

1.3 Existing technologies for hydrogen storage

1.3.1 Compressed Gaseous Hydrogen

At the storage reservoir, the simplest approach to decreasing a gas's volume, at constant temperature, is to raise the gas's pressure. It is regarded as a suitable solution for storing hydrogen because of the comparative easiness of gaseous hydrogen, its ability to refuel quickly, its outstanding properties of dormancy and its small impact on the infrastructure. In this state, H_2 is confined within pressure reservoirs. A higher pressure reflects a greater quantity of the stored hydrogen. In terms of their construction, gaseous reservoirs are classified into four main categories (**Fig. 1.2**) [36,37]:

- Type I: cylindrical metal reservoir (pressure limited to 50 MPa).
- Type II: (unlimited pressure) reservoir consisting of a metallic shell for mechanical strength, shrunk by continuous resin-impregnated fibers.

- Type III: (for P<45MPa) tank containing a metallic envelope to retain the hydrogen and a resin impregnated continuous fiber envelope for mechanical strength.
- Type IV: tank (for P<100MPa) made of a non-metallic shell to retain hydrogen and a resin-impregnated continuous fiber shell for mechanical latency.

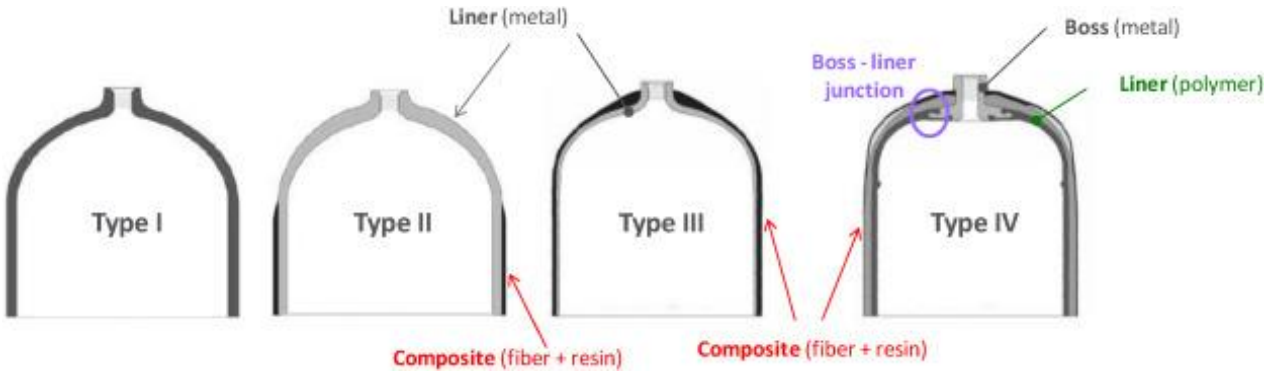

Fig. 1.2: Various types of the compressed hydrogen reservoir [36].

The choice of the shell (liner) that comes near to the hydrogen is important for every kind of reservoir. For Type I, the liner directly absorbs the mechanical stresses; a high yield strength material (steel) is thus favored. For Type III and IV reservoirs, the liner serves as a barrier for hydrogen. Therefore, a substance with low permeability to hydrogen is chosen (aluminum in the case of type III). Reservoirs are generally cylindrical in shape although they may also be polymorphic or toroidal. Hydrogen has a density of 42 kg m^{-3} at a pressure of 700 bar, compared to 0.090 kg m^{-3} at standard pressure and temperature. Currently, most vehicle producers have chosen the solution of storing gas at high pressure. Using this method, it is possible to store the amount of hydrogen needed for a car powered by a fuel cell to drive 500 to 600 km from one reservoir to the next.

1.3.2 Storage of cryogenic liquids

The liquid hydrogen at a reduced temperature is known as cryogenic liquid hydrogen. Cryogenic hydrogen is stored in tanks made up of multiple thermal isolation layers provided by a double wall vacuum as well as by insulating and metallic layers reflective of the thermal radiation.

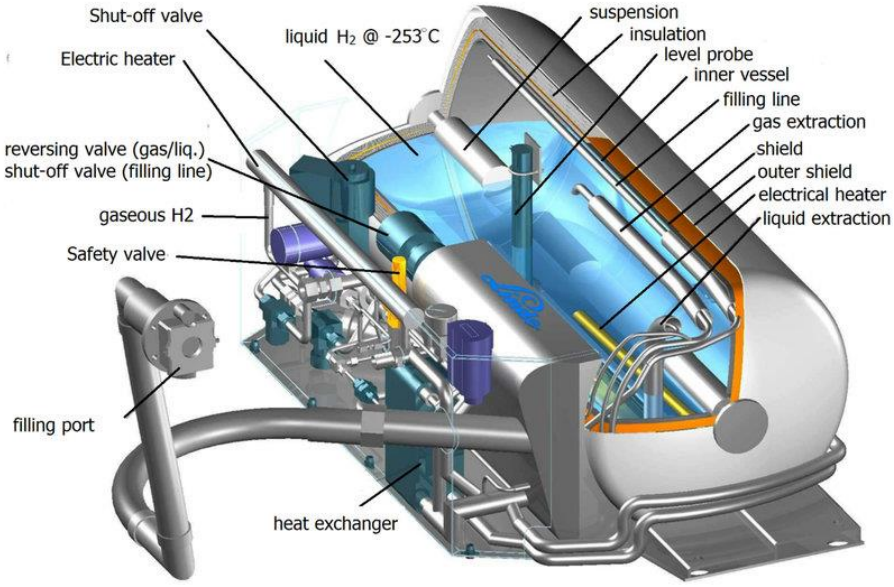

Fig. 1.3: Cryogenic reservoir (or cryostat) designed by linde [38].

The entire system is covered by an envelope made of stainless steel or composite materials (see **Fig. 1.4**) [39]. The process of liquefying hydrogen is when refrigerated to a temperature less than -252.87°C and at 1.013 bar, the density of liquid hydrogen is close to 71 kg m^{-3}. At such a pressure, 5 kg of hydrogen could be stored in a 75 L reservoir [40]. The critical temperature is -240 °C. The critical pressure is 13 bar. In consideration of storing liquid hydrogen at such a temperature, the reservoirs must be completely isolated (**Fig. 1.3**). For the moment, storing hydrogen in liquid form is limited to particular ultra-high technology uses like space transportation.

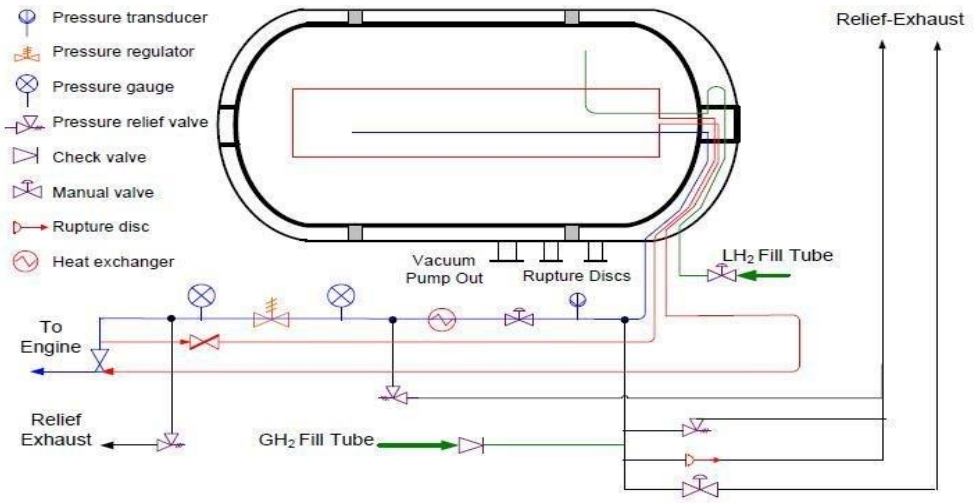

Fig. 1.4: LLNL Gen-3 cryogenic compressed hydrogen storage reservoir system design schematic [39].

1.3.3 Cry-compressed hydrogen

Cryo-compression is a hybrid technology involving a fusion of low temperature and pressure in order to improve the quantity of storable hydrogen by volume and prevent the energetic cost of hydrogen liquefaction. Compressed hydrogen gas at cryogenic temperature is significantly denser compared to gas reservoirs compressed under ambient temperature. An example of a LLNL Gen-3 cryogenic compressed reservoir system prototype is shown in **Fig. 1.4**. Such novel reservoirs reportedly are employed for hydrogen storage under temperatures as low as 80 K and under pressures ranging from 200 to 400 bar [41]. Such an arrangement necessitates further elaboration of pressure-insulated composite reservoirs. Alternatively, cold gaseous hydrogen reservoirs needing lower refrigeration might be feasible. The optimal pressure and temperature combination within the range of 80-200 K should be envisaged.

In short, the hydrogen under its form of a gas, has a density of about 0,09 kg m^{-3}. For a vehicle to reach a 400 km endurance, it would be difficult to accumulate it under ambient pressure. A mass of hydrogen of 4 kg is required, that is to say a volume of 45000 L. Using a present reservoir, the distance covered would be 600 m. Note that the fuel of gasoline was selected between others because of its ratio amount/volume. Clearly, hydrogen can never replace gasoline in this regard, although it can attempt to approach it, notably through elevated pressure: according to Boyle's rule, augmenting a gas's pressure decreases the volume of the gas at a constant temperature. Hydrogen in its liquid form has a density of 70.8 kg m^{-3}, rendering it preferable to storage in liquid form than gaseous storage. However, the primary shortcoming is the number of secondary systems needed to achieve a liquid form. Typically, hydrogen has to be supplied under temperature of approximately -253°C and pressure reaching 10 bar. That implies very high thermally isolated reservoirs, thus voluminous, to preserve it at such temperature and prevent evaporation waste. Nevertheless, parasitic evaporation, about 3% daily, is still possible. Besides, hydrogen liquefaction is an operation that requires a lot of energy: about 40% of the energy included in the gas.

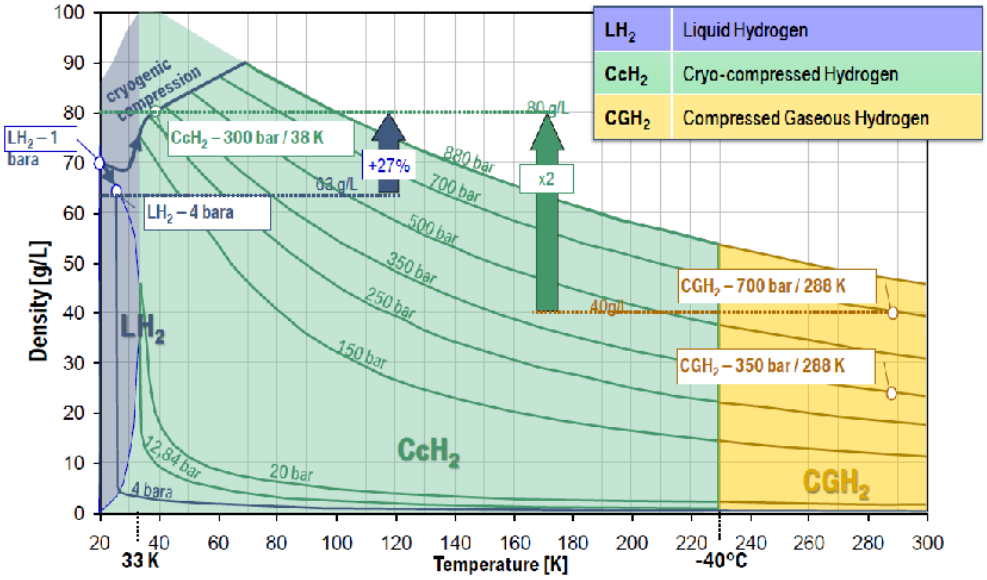

Fig. 1.5: Density of hydrogen as a function of pressure and temperature, according to BMW [42].

1.4 Procedures in development and research

Materials-based storage of hydrogen provides an attractive substitute for the earlier examined approaches (gaseous, liquid, and hybrid storage approaches). This method is separated into 3 categories: primarily, complex metal hydrides; secondly, metallic hydrides; and lastly surface storage systems (sorption materials). The majority of such storage approaches remain under the process of development, and many university researchers have been working on this issue.

1.4.1 Complex metal hydride

Such a compound category is a complex metal hydride whose overall formulation as $M(XH_n)_m$, in which M is usually a metal cation as with X a metallic or nonmetal component that establishes a bond with H to either ionically or covalently. The complex metal hydride $M[XH_n]_m$ is hydrogen-rich and able to selectively split into H_2, making them potential light-weight hydrogen storing components. The major complex hydride series regarded as attractive for storing hydrogen include alanates (based on the anion $[NH_2]^-$), amides (based on the anion $[AlH_4]^-$) as well as borohydrides (based on the anion $[BH_4]^-$) (see **Fig. 1.7**). Contrary to hydride intermetallics, metallic complex hydrides are composed mostly of fairly low weight components, which enables them to have a fairly high gravimetric capacity of hydrogen. Regrettably, the majority of complex hydrides need fairly elevated temperatures to be

thermolytically dehydrogenated, with relatively insignificant amounts being dehydrogenated reversibly, usually in the case of an additive or catalysts.

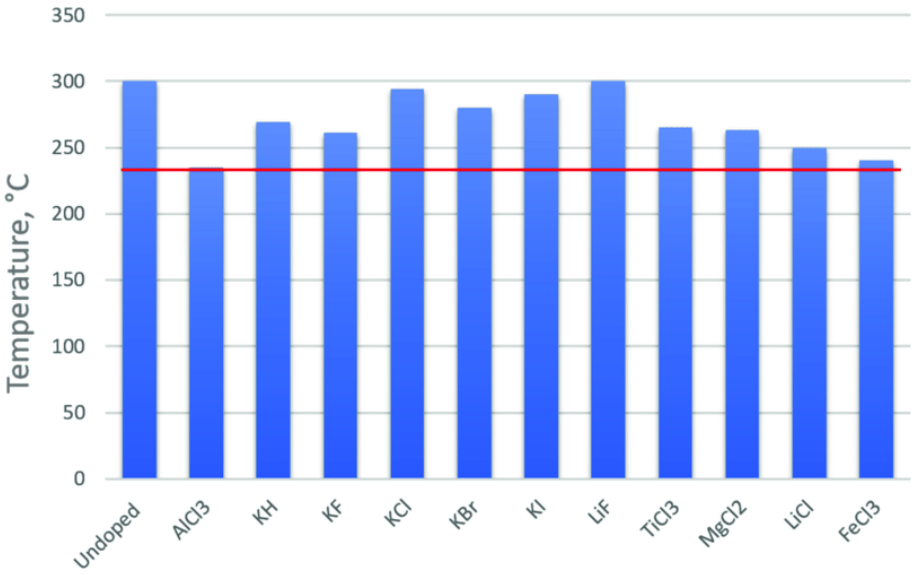

Fig. 1.6: Desorption temperature versus each additive

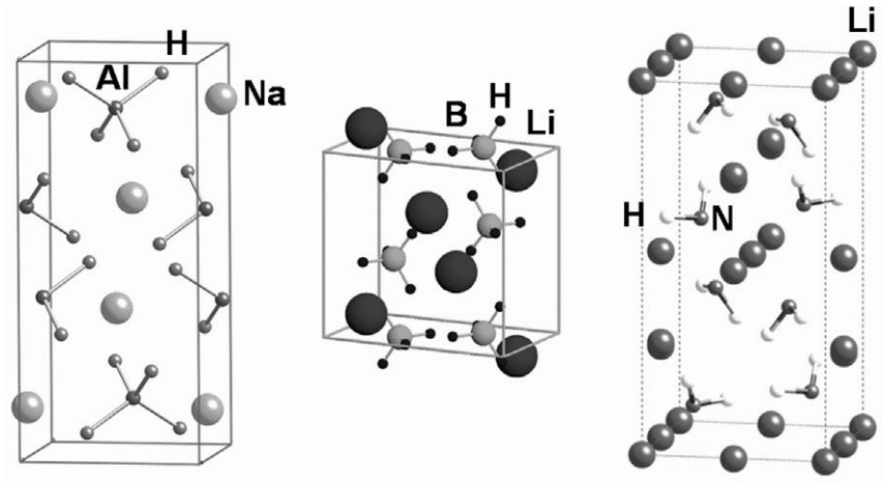

Fig. 1.7: Structure of amide, borohydride, and alanate.

Alanates

Alanate has the following chemical expression: $M(AlH_4)_n$. In gravimetric terms, alanates are able of storing a high hydrogen quantity. Details of alanate hydrogen capacities are given in **Table 1.3**. Alkanates of alkali metals decay to the intermediate hydride phases M_3AlH_6 as listed below.

Table 1.3: Theoretical Hydrogen Capacity of Alanates.

Material	**$LiAlH_4$**	**$NaAlH_4$**	**$Mg(AlH_4)_2$**	**KAlH4**	**$Ca(AlH_4)_2$**
H-capacity (mass%)	10.5	7.4	9.3	5.7	7.8

It is estimated that $LiAlH_4$ desorbs about 8.0mass% of hydrogen using 2-step reactions. Both the first and second processes of dehydrogenation involve exothermal as well as endothermal reactions, respectively [43,44].

$$3LiAlH_4(s) \rightarrow Li_3AlH_6(s) + 2Al(s) + 3H_2(g) \quad (5.3 \text{ mass\%, } 473 \text{ K}), \quad (1.1)$$

$$Li_3AlH_6(s) \rightarrow 3LiH(s) + Al(s) + (3/2)H_2(g) \quad (2.7 \text{ mass\%, } 503{-}553 \text{ K}). \quad (1.2)$$

Despite the fact that the hydrogen has a very attractive capacity, both the hydride formation as well as the decomposition of $LiAlH_4$ are barely reversible, while only the second reaction is expected to become thermodynamically reversible. Therefore, in attempt to enhance the reversibility, multiple researchers are investigating catalysts or synthesis approaches for $LiAlH_4$ [45,46]. LiH and Al are mechanically ground both with and without $TiCl_3$ for 24h in H_2 gas atmosphere at 1 MPa pressure at ambient temperature in order to recover $LiAlH_4$. It is possible to produce a small quantity of $LiAIH_4$ directly by the chemical-mechanical reaction with concomitant formation of Li_3AlH_6 [47].

The $NaAlH_4$ hydrogen desorption reaction [48] can be characterized as follows:

$$3NaAlH_4(s) \leftrightarrow Na_3AlH_6(s) + 2Al(s) + 3H_2(g) \quad (3.7 \text{ mass\%, } 458 \text{ K}), \quad (1.3)$$

$$Na_3AlH_6(s) \leftrightarrow 3NaH(s) + Al(s) + (3/2)H_2(g) \quad (1.8 \text{ mass\%, } 538 \text{ K}) \quad (1.4)$$

The primary $NaAlH_4$ decomposition reaction indicates a 3.7 wt% hydrogen desorption and the entire quantity of hydrogen desorption is achieved up to 5.5 wt% in the secondary step, in which the NaH decomposition needs a significantly elevated temperature. The reactions could be enhanced by a small quantity of Ti catalyst, as documented by Bogdanovic et al. Ti-doped $NaAlH_4$ has outstanding kinetic and cyclic characteristics which are significantly nearer to the properties needed for convenient hydrogen storage materials [48-50].

$KAlH_4$ decomposes seamlessly to KH and Al at no catalyst and stores reversibly hydrogen of approximately 3.5 wt% (hydrogen theoretical capacity is about 4.3 wt%) at 523-623K under 0.1 MPa of hydrogen, as previously investigated by Morioka et al [51]:

$$3KAlH_4(s) \leftrightarrow K_3AlH_6(s) + 2Al(s) + 3H_2(g) \quad (2.9 \text{ mass\%}), \quad (1.5)$$

$$K_3AlH_6(s) \leftrightarrow 3KH(s) + Al(s) + (3/2)\, H_2(g) \quad (1.4 \text{ mass\%}). \quad (1.6)$$

Contrary with aforementioned alanates, $Mg(AlH_4)_2$ of alkaline earth metal alanate decomposes with no formation of the intermediate phase $M(AlH_6)$. Fichtner et al. recorded that $Mg(AlH_4)_2$ dehydrogenation occurs via the undermentioned reactions [52]:

$$Mg(AlH_2)_2(s) \rightarrow MgH_2(s) + 2Al(s) + 3H_2(g) \quad (7.0 \text{ mass\%}, 383{-}473 \text{ K}) \quad (1.7)$$

$$MgH_2(s) \rightarrow Mg(s) + H_2(g) \quad (2.3 \text{ mass\%}, 513{-}653 \text{ K}), \quad (1.8)$$

$$2Al(s) + Mg(s) \rightarrow (1/2)\, Al_3Mg_2(s) + (1/2)\, Al(s) \quad (673 \text{ K}). \quad (1.9)$$

$Mg(AlH_4)_2$ decomposes at 7.0 mass % hydrogen desorption at 383-473K. At 513-653K, more hydrogen is desorbed from MgH_2 to generate Mg. Subsequently, the Mg produced is converted to Al at 673K to form Al_3Mg_2.

Amide

The complex hydrides depicted in terms of the formula $M(NH_2)_n$ are referred by the term "amides." The calculated theoretical hydrogen capacities of the amides, $LiNH_2$, $NaNH_2$, $Mg(NH_2)_2$, KNH_2, and $Ca(NH_2)_2$, are presented in **Table 1.4**.

Table 1.4: Theoretical Hydrogen Capacity of Amides.

Material	**$LiNH_2$**	**$NaNH_2$**	**$Mg(NH_2)_2$**	**KNH_2**	**$Ca(NH_2)_2$**
H-capacity (mass%)	8.78	5.15	7.15	3.66	5.59

Of these, $LiNH_2$ and $Mg(NH_2)_2$ decomposition is presented as follows:

$$2LiNH_2(s) \rightarrow Li_2NH(s) + NH_3(g), \quad (1.10)$$

$$Mg(NH_2)_2(s) \rightarrow MgNH(s) + NH_3(g) \quad (1.11)$$

Amides desorb NH_3 as the primary desorption gas to form imides for example Li_2NH and MgNH within the temperature range of 473 to 673K. Hence, even though amides have high hydrogen capacities, it is hard to employ them alone as materials for hydrogen storage.

Borohydride

The complex hydrides consisting of Mn^+ and $(BH_4)^-_n$ are called " Borohydrides". For hydrogen storage materials, borohydrides are very interesting due to their exceedingly elevated capacities of hydrogen owing to the elevated composition of hydrogen in the anion, as illustrated in **Table 1.5**.

Borohydride dehydrogenation reactions are carried out whereby binary hydrides MH_n and boron B or metal borides MB_l (l can be 2 or 6) are formed, according to M^{n+} cation, as illustrated below:

$$2LiBH_4(s) \rightarrow 2LiH(s) + 2B(s) + H_2(g), \qquad (1.12)$$

$$3Ca(BH_4)_2(s) \rightarrow 2CaH_2(s) + CaB_6(s) + 10H_2(g). \qquad (1.13)$$

Table 1.5: Theoretical Hydrogen Capacity of Borohydrides.

Material	**$LiBH_4$**	**$NaBH_4$**	**$Mg(BH_4)_2$**	**KBH_4**	**$Ca(BH_4)_2$**	**$Al(BH_4)_3$**
H-capacity (mass%)	18.4	10.6	14.8	7.4	11.5	16.8

Suitable $LiBH_4$ in a typical borohydride desorbs three hydrogen atoms in three steps as shown below [53]:

$LiBH_4(s) \rightarrow LiBH_{4-x}(s) + (x/2)H_2(g)$ (0.3 mass%, 383 K), (1.14)

$LiBH_{4-x}(l) \rightarrow "LiBH_2"(l) + ((1 – x)/ 2)- H_2(g)$ (8.7 mass%, 753 K), (1.15)

$"LiBH_2"\ (l) \rightarrow LiH(s) + B(s) + (1/2)H_2(g)$ (4.5 mass%, >873 K). (1.16)

As temperature is elevated, a structural transition occurs at 378K from orthorhombic to tetragonal with a small quantity of hydrogen (0.3 mass%) being released. Over the fusion point of 553K, the primary hydrogen desorption is disclosed at 593K, followed by an incremental 1.0 mass % hydrogen liberation. While heating to 873K, approximately 7.7 mass % hydrogen is desorbed around 753K as secondary hydrogen desorption. The overall quantity of hydrogen desorbed is approximately 9.0 mass% at 873K, equivalent to half the theoretical $LiBH_4$ hydrogen capacity. Therefore, the final product has a composition nominally "$LiBH_2$" as indicated in equation (1.15). According to Züttel et al. the process of hydrogen desorption may be catalyzed by SiO_2 addition [54]. In such cases, 9.0 wt% hydrogen is desorbed at lower 673K, with the quantity of hydrogen desorbed being achieved up to 13.5 wt% at increased temperature. According to the latest research, the desorption reaction of hydrogen in $LiBH_4$ is reversible,

whereby the final products, LiH and B, absorb hydrogen at 963K and 200bar so as to form $LiBH_4$ [55]. The reaction mechanism of absorption and desorption of hydrogen for $LiBH_4$, however, remains to be understood. Moreover, $LiBH_4$ is quite stable for on-board application as the enthalpy shift of the reaction was found to be around 67.0kJ/mol H_2 [56]. In the last few years, there have been various efforts to synthesize and investigate different types of borohydrides consisting of alternative M^{n+} (= Al, Sc, Zr, Ti, Zn, etc.) and $(BH_4)^-_n$ for their hydrogen storage characteristics [57,58].

1.4.2 Metal Hydrides

An alternative solution is the storage of hydrogen in a solid form. i.e., reversible metal hydrides. Some metals or alloys react naturally with hydrogen in the following way:

$$M + xH_2 \Leftrightarrow MH_{2x} + \text{heat} \qquad (1.17)$$

The resulting product from this reaction is a metal hydride with heat. (Exothermic reaction). There are three types of hydrides, according to the type of bonding of the hydrogen to the metal: ionic, covalent and metallic hydrides.

Process for forming a metal hydride

The process of hydration of an intermetallic composite material is an exothermic reaction. It is characterized by a straightforward combination of the intermetallic composite and hydrogen through the subsequent stages:

1. Hydrogen gas transport among the pores;
2. Hydrogen molecules adsorption at the substrate;
3. Chemisorption and dissociation of hydrogen molecules in atoms;
4. Hydrogen atoms diffusion into the solid phase;
5. Hydride formation.

The various steps may be described as sequential or synchronous. Concerning the process of desorption, it may be simply defined as the inverse of the mechanism of absorption just mentioned.

Pressure-composition-temperature isotherms (PCT)

The majority of binary metallic hydrides were synthesized via a solid-gas reaction among hydrogen and the metal. As illustrated by idealized isotherms of pressure-composition (**Fig. 1.8**), a solid hydrogen solution within the metal at small hydrogen pressure p_{H2} develops, in that H inhabits positions interspersed within the host metal lattice (α phase). On reaching the equilibrium pressure p_{eq}, a metallic hydride (β-phase, occasionally termed α′) develops that maintains the pressure constant until the α-phase is completely transformed to β-phase by the end of the shelf area. The shelf area temperature and pressure establish the requirements to make metallic hydrides and to reversibly store hydrogen in such materials. The concentration of hydrogen (c_H) at the tip of the shelf and the length of the shelf area define the peak hydrogen absorption and the capacity needed to store hydrogen reversibly, respectively. Within the β single-phase area subsequent to the shelf, again the pressure drastically elevates along with only slight compositional changes. This area can be attended by further shelf areas with increasing pressures. Beyond a critical temperature T_c, the biphasic area vanishes and the concentration of hydrogen within the metal hydride may change steadily. The enthalpy of metal hydride formation ΔH, which is usually negative, and the reaction entropy ΔS may be obtained from a van't Hoff curve $\ln p_{eq}$ vs $1/T$ by using the formula $\ln p_{eq} = \Delta H/RT - S/R$ (R, gas constant; **Fig. 1.8**, right).

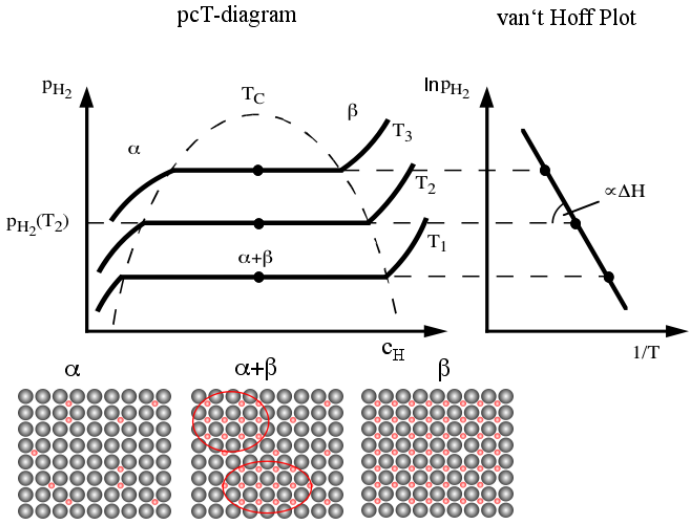

Fig. 1.8: Schematic P-C-T-diagram and van't Hoff plot. The α-phase is the solid solution phase, the β-phase the hydride phase. Within the (α + β) two phase regions both the metal-hydrogen solution and the hydride phase coexist [59].

The various types of metal hydrides

Metallic hydrides have received rising attention as a candidate material for in-vehicle hydrogen storage due to hydrogen adsorption/desorption reversibility and their elevated hydrogen density. However, the practical application of metallic hydrides is hindered by their comparatively elevated temperature of dehydrogenation (>300 °C) and lower properties in hydrogenation-dehydrogenation cycles. Certain metallic hydrides liberate hydrogen at the comparatively low temperatures as well as pressures needed for fuel cells. For instance, it is possible for $LaNi_5H_6$ to liberate hydrogen at proton exchange membrane (PEM) fuel cell running temperatures (1-10 atm and 25-100 °C), although its gravimetric capacity is insufficient (∼1.4 wt%) and its price is too expensive for vehicular applications [60,61].

In comparison to traditional metallic hydrides (MH_x, M=Li, Na, Al, Mg, etc.), the complex metallic hydrides provide an opportunity to enhance the gravimetric capacity of hydrogen. With the addition of titanium dopants, the sodium alanate ($NaAlH_4$) can reversibly store and liberate hydrogen with low temperature (∼150 °C) [62,63]. Nevertheless, the complex metallic hydrides continue to provide comparatively small capacity for hydrogen and low hydrogen uptake and liberation rates. For instance, the maximum theoretical gravimetric capacity of the sodium alanate material (not the system) would be 7.4 wt% hydrogen, compared to current real material capacities as low as 3 to 4 wt%. Furthermore, the kinetics of hydrogen liberation would be too low for automotive uses [64,65].

Lately, both amides and imides have gained attention because of their great capacity for hydrogen storage [65,66]. Global dehydrogenation of lithium amide ($LiNH_2$) and hydride (LiH) is demonstrated as:

$$LiNH_2 + LiH \rightarrow Li_2NH + H_2 \qquad (1.18)$$

Consisting of two steps as below:

$$2LiNH_2 \rightarrow Li_2NH + NH_3 \qquad (1.19)$$

$$NH_3 + LiH \rightarrow LiNH_2 + H_2 \qquad (1.20)$$

Within the given reaction, 6.5 wt% of hydrogen may be absorbed / desorbed theoretically at 285 °C through the two stages provided by equations (1.19) and (1.20). This value, in turn, is beyond the range of the waste heat usage window of a PEM fuel cell. One way to reach this temperature value on board vehicles is through a burner sacrifice of some of the hydrogen, a cost, volume, weight, and efficiency penalty for the system. A further issue with such a system

is ammonia formation occurring as a byproduct which poisons the catalyst of the PEM fuel cell [67-69].

Theoretical material-based H_2 capacities for different hydrides, such as metal, complex metal, and chemical hydrides, have been listed in **Table 1.6**. Many different types of metal hydrides have been investigated as hydrogen storage media. Although, the higher hydrogen liberation characteristics (yield and kinetics) are obtained under temperature conditions significantly greater than PEM fuel cell operating conditions, as noted in the preceding discussion. Numerous attempts to improve dehydrogenation kinetics have been devoted to ball milling, doping of additives, alloys with other components, nanotechnology, and confinement in porous materials (**Table 1.7**). A summary of the effects of different additive doping on the dehydrogenation activation energies is given in **Table 1.7** for a number of chosen metal hydrides. A common approach to finding activation energy from starting temperature changes using varied heating regimes is the Kissinger method [70]. In a further consideration, efficient management of heat within the system is significant in enhancing system efficiency. Although, these issues are exceeded, this approach is not expected to achieve DOE's goals within the predictable timeframe. By way of example, sodium alanate, among the most prospective metal hydrides, is considered to contribute only 1.2 wt% H_2 and 12 g H_2 per liter to the system, which is well under DOE goals (**Table 1.2**).

Table 1.6: Theoretical hydrogen capacities of selected hydrides [71].

Hydride	Compound	Gravimetric H_2 content (wt%)
Metal hydrides	LiH	12.6
	NaH	4.2
	CaH_2	4.8
	MgH_2	7.6
Complex metal hydrides	$LiAlH_4$	10.6
	$NaAlH_4$	7.4
	$Mg(AlH_4)_2$	9.3
	$LaNi_5H_6$	1.4

Chemical hydrides	$LiBH_4$	18.4
	$NaBH_4$	10.6
	NH_3BH_3	19.8

Table 1.7: Comparison of activation energies of pristine and doped metal hydrides.

Metal hydride	Additive	1st stage (kJ mol^{-1})	2nd stage (kJ mol^{-1})	References
MgH_2	Pristine	111–166		44–46
	Fe– (e.g., Fe, Fe_2O_3, Fe_3O_4, $FeCl_3$)	112–130		45,47,48
	Mo– (e.g., MoO_2, MoS_2)	87–101		44
	Ti– (e.g., $TiCl_3$, TiH_2, TiO_2)	58–97		49–51
$LiAlH_4$	Pristine	81–122	101–181	52–54
	Fe_2O_3	54	86	55
	K_2TiF_6	78	91	56
	$MnFe_2O_4$	67	76	57
	Ni– (e.g., $NiCo_2O_4$, $NiFe_2O_4$)	54–79	71–95	58,59
	Ti– (e.g., $TiCl_3$, TiH_2, TiN, TiO_2)	39–88	69–93	54,60,61
$NaAlH_4$	Pristine	116–118	121–149	62,63
	Ce– (e.g., CeB_6, $CeCl_3$, CeF_3, CeO_2)	69–112	97–109	64,65
	K_2TiF_6	100	88	66
	Nb_2O_5	65	86	62
	Ti– (e.g., Ti, $TiCl_3$, TiN, TiO_2)	74–99	98–130	62,67– 69

1.4.3 Sorption materials

The adsorption of a gas like hydrogen onto a solid, or physisorption, means that the density of that gas at the solid material surface is enhanced due to the existence of intermolecular

strengths. Such adsorption is enhancing with the gas's pressure the smaller the temperature and the greater the area of interaction with the solid. Physisorption is entirely reversible: it reduces as the pressure is reduced and/or as the temperature enhanced. It is based on the interaction of van der Waals among hydrogen molecules and carbon materials. The energy of interaction among the solid material and hydrogen molecules may be calculated as [72]:

$$E = \frac{\alpha_{H_2}\,\alpha_{substrate}}{R^6} \qquad (1.21)$$

In which α is the polarizability and R is the interaction distance. The hydrogen storage capacity based on physisorption may be estimated as the summation of solid surface adsorption and split pore compression. Hydrogen adsorption happens in the micropores in which an adsorbed hydrogen phase density is greater as compared to the non-adsorbed gas phase over the critical point. However, the capacity of the adsorbent material to store hydrogen may be measured in terms of micropore specific surface area (SSA), which is the physisorption capability of the lower nanoscale materials having a high specific surface area due to the weak Van der Waals forces existing among the adsorbate and thus the adsorbent. The combination of both a long-range engagement term and a short-range repulsion term gives rise to a shallow minimum in the potential energy curve at a distance of approximately one molecular radius from the gas molecule, this minimum energy usually matches 1^{-10} kJ mol^{-1} [73, 74]. Because the forces implied within the interaction that occurs among the adsorbate and the adsorbent are very small, the physisorption normally occurs only at lower temperatures. Since there is no energy barrier to keep the molecule approaching the surface from getting into the physisorption sink, then the process is inactivated and fast kinetics are typical of physical adsorption.

Metal-Organic Frameworks MOF's

Metal-organic frameworks (MOFs) represent the primary porous media that have been extensively studied for hydrogen conservation. Due to their extremely large pores and highly developed substrates, they are able to store large quantities of hydrogen at cryogenic temperatures. MOFs represent porous crystalline frameworks composed of two components: secondary construction elements (clusters or metal ions) enclosed within organic molecules (linkers). MOFs are synthesized through the solvothermal reaction of metallic ions with different carboxylic acids. Different metallic sources have been employed in MOFs synthesis, like Ni, Zn, Cr, Mn, Cu, Ni, rare earth metals and alkaline metals. Various kinds of MOFs were discovered during the last 20 years depending on amount of coordination of secondary building

units, bonding type, various synthetics as well as size of the pores [75, 76-80]. Metallic framework building blocks as well as organic linkers may be arranged in nearly limitless combinations to produce novel materials. Consequently, some kind of unique structural features may be obtained by adjusting the basic materials depending upon their particular application. The adsorption of hydrogen molecules on carbon nanostructured materials or metal organic frameworks (MOFs) has been demonstrated by Dillon et al [81]. While these materials possess a potentially great gravimetric capacity, since they need large surface areas (4000 m g^{-2}), their volumetric hydrogen storage capacity is probably weak [81, 82]. Nevertheless, a benefit of such materials is low hydrogen fixation and release of the gas is not expected to necessitate high temperatures. There are scientific attempts to further investigate the development and modification of MOFs for storing hydrogen. Nevertheless, it should be noted that cryogenic conditions (77 K) at ambient pressure (1 bar) are impractical [81, 82] (**Fig. 1.9**).

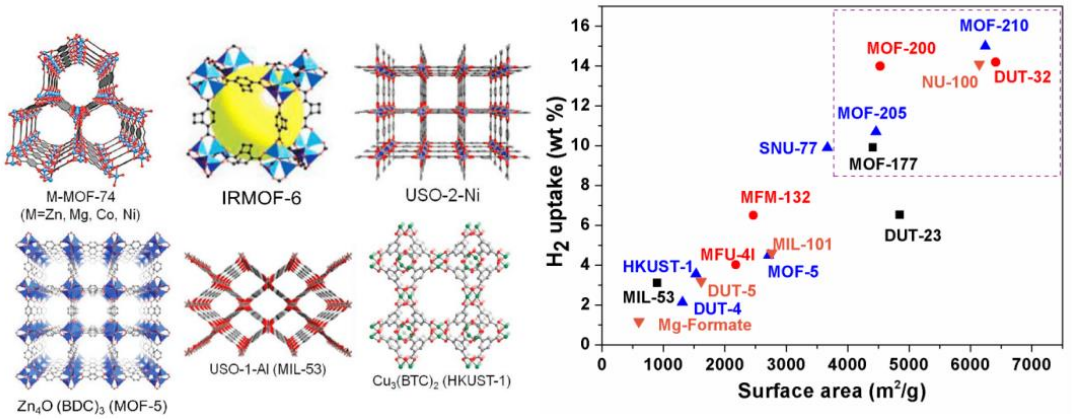

Fig. 1.9: Common samples: Porous MOFs made by multiple research teams (left) [78], H_2 absorption capacities at 77 K as a function of the surfaces of certain highly porous MOFs (right) [83].

Carbon based materials

Carbon aerogels (CAs) represents a further category of porous carbonaceous materials presenting significant surface areas and high mesopore volumes, which are extremely costly to dry supercritical. based on organic aerogels. They are composed of interlinked carbon nanoparticle clusters varying in diameter from 3 to 20 nm. Due to their microporosity, low density and high surface area, carbon aerogels are promising materials as hydrogen storage adsorbent application.

Graphite is sp^2 hybridization with a sheet structure in which all atoms are loosely linked together and existing in one plane, and are held apart by van der Waals forces to the sheets on

top and bottom. Although highly polarizable, the graphite has a small capacity for hydrogen storage because of its low interlayer spacing and small SSA. Graphite's interlayer spacing (3.354 Å) is significantly low for hydrogen molecule intercalation (4.06 Å) [84]. Consequently, multiple approaches to increase the interlayer distance, which can subsequently increase the SSA of graphite, have been studied. For instance, alkali metal or metal doping increases the interlayer distance and, thus, the capacity of hydrogen storage (Ni (0.92 wt%), Cu (0.97 wt%), Co (1.8 wt%), Al (3.48 wt%), Li (6.5 wt%) [85-89]). It has also been previously described that grinding of graphite nanofibers and graphite beads enhances the SSA owing to particle size decrease.

Activated carbon (AC) represents a form of treated carbon including graphite crystallites as well as amorphous carbon, manufactured using biomass resources, with a pore size typically below 1 nm, with an SSA of 3000 m^3 g^{-1} [90]. The hydrogen storage capacity experimentally measured depends also on the used material (doping, etc.), varying from 0.5 to 5 wt% [91]. ACs have a small density of mass and a large surface area. The low van der Waal forces enable hydrogen molecules to be physisorbed as they are adsorbed and diffuse through the pores of CAs [92]. Hydrogen adsorption at ambient temperature and 77.4 K was investigated on ACs with SSA of 2560 m^3 g^{-1}. The maximum experimentally determined capacity for hydrogen storage has been found to be 4.5 wt% at 77.4 K with elevated kinetics and reversibility of adsorption [93]. Bénard and Chahine also illustrated that adsorption of hydrogen in AC may be more successful compared to compressed gas at cryogenic temperature [94].

Fullerene represents a carbon molecule which can have a geometrical form resembling a sphere, an ellipsoid, a tubular shape (called nanotube) or a ring. Similar to graphite, fullerenes consist of hexagonal rings linked together, although they contain pentagonal and occasionally heptagonal rings, thus avoiding flatness of the layer. The third form of carbon is known as fullerenes [95]. The most prevalent is C_{60}, composed of 12 pentagons and 20 hexagons, with a form similar to that of a ball. According to C_{60} calculations, its theoretical capacity for hydrogen storage is up to 8 wt% using transition metals such as titanium and scandium [96].

Carbon nanotubes (CNT) represent an allotropic shape of the family of fullerenes. They consist of several layers of rolled up carbon atoms making a tube. This tube may or may not be sealed at its extremities by a half-sphere. A difference is made among the single-walled carbon nanotubes (SWCNT) and the multi-walled carbon nanotubes (MWCNT) [97, 98]. Hence,

CNTs' hydrogen storage capabilities mostly rely on their structure, pretreatments, geometry, structural defects, operating pressure, temperature, etc.

Carbon nanofibers consist of cylindrical graphene layers arranged in a specific geometry. The CNF structures may be shaped at high temperatures using a combination of gases containing carbon and hydrogen. They may be also shaped from hydrocarbons alone by the use of nickel and iron containing alloys as catalyst. Various kinds of CNFs with varying morphology, crystal structure and form are feasible by changing the catalyst nature and geometry and the reaction conditions. The hydrogen enters the CNF nanopores shaped by the CNF sheets and the CNT interior by shaping a layer intercalated of hydrogen.

Graphene is a single layer of graphite that has been isolated from a thicker part or grown into a single layer. Graphene is composed of carbon atoms arranged in a hexagonal pattern to form a flat, sheet-like structure. The atoms are spaced 1.42 Å apart with a bond angle of 120° to form a honeycomb-like pattern of a single layer of atoms. This structural arrangement gives graphene excellent thermal conductivity (3000 W m^{-1} K^{-1}), mechanical stiffness (1060 GPa), optical transparency (>90%), and charge carrier mobility (2000-20,000 cm^2 V^{-1} s^{-1}) [99-104]. Due to its outstanding properties in electronics, graphene has become widely known. The two-dimensional crystal structure of the lattice leads to a massless fermion-like behavior of the electrons, where the speed of light is replaced by a Fermi speed of about 106 m/s. The electrons in graphene exhibit high charge carrier mobility. Due to its great properties, it is considered a potential material for many applications, for example, gas sensors, potential electrode materials and ultra-high frequency transistors. Recently, it has been proven that the sorption capacity of graphene layers is more efficient than that of activated carbon [105-108].

Hydrogen can basically be adsorbed on graphene in two different ways: either by physisorption, i.e., interacting by Van Der Waals (VdW) forces, or by chemisorption, i.e., by forming a chemical bond with the C atoms. Physisorption usually happens with hydrogen in molecular form. The H_2 binding energy was theoretically evaluated in the range 0.01-0.06 eV [109,110], this large spread of values depending on the fact that London dispersion forces are very elusive and difficult to represent. Despite that, it is clear that the binding of molecular hydrogen is very weak and requires therefore low temperatures and high pressures to ensure reasonable storage stability. It was shown by a simple empirical argument that in the most favorable conditions (high pressure and low temperature) H_2 can form a uniform compact monolayer on the graphene sheet, corresponding to GD (gravimetric density) of 3.3% [111] (doubled if the two sides are

considered). Chemisorption of molecular hydrogen on graphene presents rather high barriers of approximately ∼1.5eV [112], because it requires the dissociation of H_2 (dissociative adsorption). Conversely, the chemisorption of atomic hydrogen is a rather favorable process: indeed, commonly accepted values for H binding energy and chemisorption barriers are ∼0.7eV and ∼0.3eV, respectively. These values were extracted from several experimental studies on highly oriented graphite [113,111], and from theoretical studies mainly based on Density Functional Theory (DFT) with model systems mimicking graphite [114,115,116,117] or graphene [118]. More recent scanning tunnelling microscopy (STM) experiments have focused on atomic-scale imaging of adsorption and clustering phenomena of hydrogen atoms on graphite [119,120,121,122]. The theoretical studies have shown, in particular, that adsorption of the first H atom locally modifies the graphene structure favoring further H binding, with a collective stabilization effect [123,124]. The formation of "dimers" of H on the graphene surface was shown to bring up to ∼1eV gain in energy with respect to isolated bound H [125,126]. Atomic hydrogen absorption on epitaxial graphene on SiC was also investigated by STM showing formation of dimer structures, preferential adsorption of protruding graphene areas and clustering at large hydrogen coverage [127,128].

Fig. 1.10 represents a gravimetric vs volumetric density diagram for several hydrogen storage systems including the graphene-based ones. The line tends to the value of liquid hydrogen for large sized nanotubes. In general, nanostructured physisorption based graphitic systems occupy the area below this line. The oblique shaded strip represents the optimal physisorption within graphene multilayers with spacing nearly double than in graphite (and density nearly one half). Different storage densities in this case correspond to different pressure and temperatures. The vertical dark red strips represent adsorption in decorated or functionalized graphene. These systems have been mostly studied at the level of a single layer, for this reason only the gravimetric density is well defined, while the volumetric density range has been roughly estimated considering variable inter-layer spacing 2-4 times that of graphite. The same criterion has been used to estimate the volumetric density for chemisorption in multilayers (blue rectangle); for this system the gravimetric density has a sharp right edge, corresponding to the maximum loading with 1:1 stoichiometry of C and H (∼8%). The storage properties of systems based on material different from graphene (different metal hydrides (including MgH_2), hydrocarbons, N- and B- hydrides) are also reported as shaded areas in red, violet and green. The DOE targets (for 2015 and ultimate) are indicated with green stars. The constant density lines are in grey. From the point of view of hydrogen storage, the maximum GD reachable in

graphene with chemisorption is 8.3% (=1/12), i.e., even larger than the "ultimate" goal of DOE (see **Fig 1.10**). The orange line represents the optimal relationship for physisorption in nanotubes (the dots correspond to different sizes). This corresponds to the formation of a completely saturated graphene sheet, with 1:1 C vs H stoichiometry, namely "graphane", whose stability was first hypothesized in a DFT based theoretical study [129], and subsequently studied in experiments [130]. The experimental work, in particular, showed one side hydrogenation of a graphene sheet and its reversibility by thermal annealing. Graphane is a strong insulator and removal of hydrogen in selected regions can lead to a controllable band-gap opening [131,132,133]. As in the case of physisorption, the VD (volumetric density) depends on the possibility of building compact structures with graphene (or graphane) sheets. The energy profiles for the processes of adsorption of hydrogen on graphene are summarized in **Fig. 1.11**. **Fig. 1.11** represents the energy level diagram for the graphene-hydrogen system. The energy is in eV per H atom, i.e., to obtain the values per H_2 each energy and barrier value must be doubled. Values of energy levels and barriers are deducted both from experimental and theoretical evaluations with average values taken when different values are available. The reference level is the pristine graphene plus unbound molecular hydrogen.

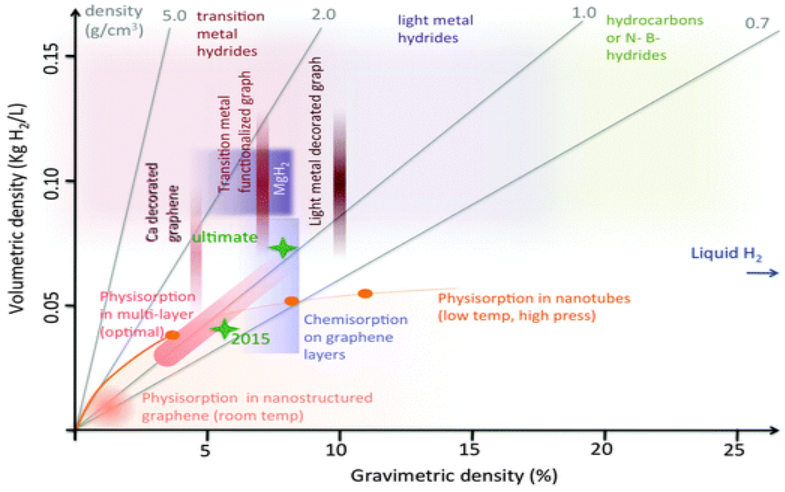

Fig. 1.10: Gravimetric vs volumetric density diagram for several hydrogen storage systems including the graphene-based ones [134].

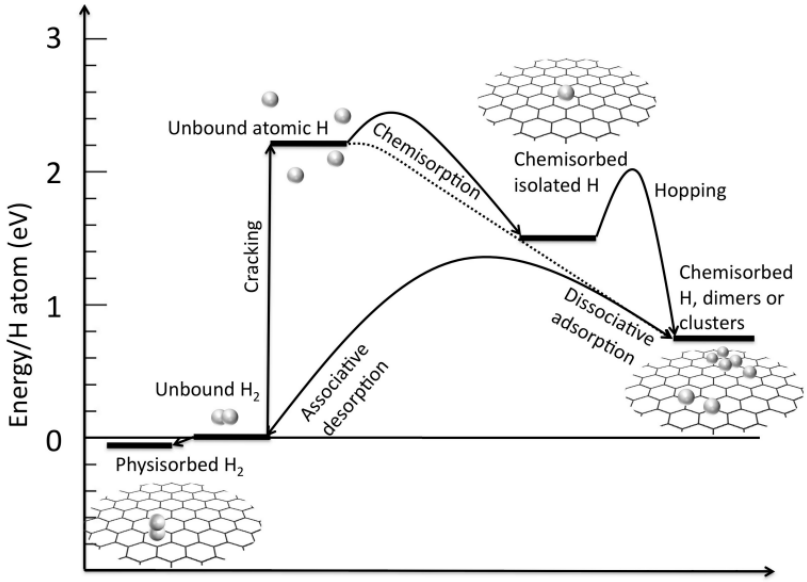

Fig. 1.11: Energy level diagram for the graphene-hydrogen system [134].

Chapter II: Theory and modeling

2 Density Functional Theory: Concepts and Methods

2.1 Introduction

The comprehension of the properties of material necessitates the investigation of phenomena ranging from the macroscopic to the microscopic scale. These include atomic and molecular objects, electrons and atomic nuclei. A valuable tool for examining physics and chemistry on such scales is the density functional theory (DFT), and the exact applications of this theory rely on the approximation of the electron-electron interaction energy. The objective of this chapter is to describe the modeling of the physical issue at hand. As the DFT theory is mainly concerned with the Schrödinger equation, we shall present different approximations and ways of solving it.

2.2 Theory

2.2.1 The Schrödinger equation

In physics, specifically quantum mechanics, the Schrödinger equation, formulated in 1926 by Austrian physicist Erwin Schrödinger, is an equation that describes how the quantum state of a physical system changes in time. It is as central to quantum mechanics as Newton's laws are to classical mechanics. In the standard interpretation of quantum mechanics, the quantum state, also called a wavefunction or state vector, is the most complete description that can be given to a physical system. Solutions to Schrödinger equation describe not only molecular, atomic and subatomic systems, but also macroscopic systems, possibly even the whole universe [135].

The most general form is the time-dependent Schrödinger equation, which gives a description of a system evolving with time. For systems in a stationary state, the time-independent Schrödinger equation is sufficient. Approximate solutions to the time independent Schrödinger equation are commonly used to calculate the energy levels and other properties of atoms and molecules.

The many body form of the time independent Schrödinger equation consisting of M nuclei and N electrons is written as:

$$\hat{H}\Psi_i(\overrightarrow{r_1}, \ldots, \vec{r}_N, \overrightarrow{R_1}, \ldots, \overrightarrow{R_M}) = E\Psi_i(\overrightarrow{r_1}, \ldots, \vec{r}_N, \overrightarrow{R_1}, \ldots, \overrightarrow{R_M}), \quad (2.1)$$

where $\hat{H}$ denotes the Hamiltonian, and Ψ_i denotes the wave function in terms of all the electronic (r) and nuclear coordinates (R). The Hamiltonian $\hat{H}$ in equation (2.1) which represents total energy consisting of different kinetic and potential energy terms can be written as:

$$\hat{H} = -\frac{1}{2}\sum_{i=1}^{N}\nabla_i^2 - \frac{1}{2}\sum_{A=1}^{M}\frac{1}{M_A}\nabla_A^2 - \sum_{i=1}^{N}\sum_{A=1}^{M}\frac{Z_A}{r_iA} + \sum_{i=1}^{N}\sum_{j>i}^{N}\frac{1}{r_{ij}} + \sum_{A=1}^{M}\sum_{B>A}^{M}\frac{Z_A Z_B}{R_{AB}} \quad (2.2)$$

A and B represent M nuclei, i, j denote the N electrons in the system and ∇^2 is the Laplacian operator. The first two terms in equation (2.2) are the kinetic energies for the electrons and the nuclei, respectively. The remaining three terms constitute the potential energy part of the total energy and represent coulombic interactions in order: electron-nuclei attractions, electron-electron and the nucleus-nucleus repulsions. In principle, the above equation is applicable to any physical system regardless of size (i.e., from atoms to a whole crystal). In practice, however, a complete analytical solution is impossible for most real-life systems, since the number of variables to deal with is determined by the $3(M + N)$ degrees of freedom. If we consider the benzene molecule, then there are in total 12 atomic nuclei and 42 electrons. The time independent Schrödinger equation for a single benzene molecule consequently becomes a partial differential eigenvalue problem in 162 variables. Since the exact solution of the Schrödinger equation is formidable to solve for almost every real system, various approximations have to be made.

2.2.2 The Born-Oppenheimer Approximation

As shown in last section, the computation of the energy and wavefunction of an average-size molecule is a formidable task which has to be alleviated by approximations. The Born-Oppenheimer (BO) approximation [136] permits us to separate the electronic and nuclear motions. The justification for this is the difference between masses of nuclei and electrons. Because nuclei are much heavier than electrons, their coordinates are assumed to evolve classically. In basic terms, it allows the wavefunction of a molecule to be broken into its electronic and nuclear (vibrational, rotational) components. After exclusion of nuclear terms, equation (2.2) takes the form:

$$\hat{H}_{elec} = -\frac{1}{2}\sum_{i=1}^{N}\nabla_i^2 - \sum_{i=1}^{N}\sum_{A=1}^{M}\frac{Z_A}{r_iA} + \sum_{i=1}^{N}\sum_{j>i}^{N}\frac{1}{r_{ij}} \qquad (2.3)$$

The solution of the equation (2.1) with the electronic Hamiltonian of equation (2.3) above gives the electronic wave function Ψ_{elec} and the electronic energy E_{elec} for a particular configuration of the M nuclei. Therefore, the electronic Schrödinger equation is reduced to

$$\hat{H}_{elec}\Psi_{elec} = E_{elec}\,\Psi_{elec}\,. \qquad (2.4)$$

The total energy of the system is obtained by including the constant nuclear repulsion term of the complete Hamiltonian as equation (2.2):

$$E_{total} = E_{elec} + E_{nuc}, \qquad (2.5)$$

Where

$$E_{nuc} = \sum_{A=1}^{M}\sum_{B>A}^{M}\frac{Z_A Z_B}{R_{AB}} \qquad (2.6)$$

Even after this simplification, the task of solving the electronic Schrödinger wave equation remains challenging.

2.2.3 Hartree-Fock approximation

The Hartree-Fock approach attempts to solve the electronic Schrödinger equation approximately, and supposes that the wave function may be approached by a single Slater determinant consisting of one spin orbital for each electron. The aim of the Hartree-Fock approach is to generate as good wave functions as possible for one electron so that the correct wave function can be approached for a multiple electron system. In such cases, the Hel operator is regarded as consisting of 3 operators (the kinetic operator, the electron-core interaction and the interaction among all the electrons):

$$H_{elec} = T_e + V_{ee} + V_{en} \qquad (2.7)$$

Hartree's approach

This approximation is based on substituting the interaction of every electron with every other electron by the interaction of an average field formed by the nuclei and all other electrons, i.e., each electron is independently moving in an average field formed by all other electrons and

nuclei [137-139]. This allows us to substitute the $1/r_{ij}$ type potential that relies on the coordinates of both electrons by a term describing the electronic interaction that relies on each isolated electron's coordinates. Therefore, in this approach, the correlations are negligible making it possible to state:

$$\Psi_H(\{r\}) = \Psi_1(r_1)\,\Psi_2(r_2)\ldots\Psi_N(r_N) \qquad (2.8)$$

Definition of Hartree Potential

The Hartree potential or Coulomb potential V_H is determined by [137]:

$$\mathrm{V_H(r)} = \int \mathrm{dr'}\,\frac{\mathrm{n(r')}}{|\mathrm{r}-\mathrm{r'}|} \qquad (2.9)$$

This equation defines the electron interaction at a position r with an electron cloud of density $\mathrm{n(r')}$. We emphasize that, the approximation equation of Hartree disregards the wave function antisymmetry, since the electron is a fermion then the total wave function needs to be antisymmetric with regard to the exchange between any two particles that is disregarded by Hartree.

Hartree-Fock Method (1930)

In order to re-establish the neglected wave function antisymmetric in the Hartree equation, Pauli's exclusion rule was suggested by Fock. The electronic wave function is thus described in terms of a Slater determinant [140-142]:

$$\Psi(\mathrm{r_1},\ldots\mathrm{r_n}) = \frac{1}{\sqrt{\mathrm{n!}}}\begin{vmatrix} \psi_1(\mathrm{r_1}) & \psi_1(\mathrm{r_2})\ldots\psi_1(\mathrm{r_n}) \\ \psi_2(\mathrm{r_1}) & \psi_2(\mathrm{r_2})\ldots\psi_2(\mathrm{r_n}) \\ \vdots & \vdots \\ \psi_\mathrm{n}(\mathrm{r_1}) & \psi_\mathrm{n}(\mathrm{r_2})\ldots\psi_\mathrm{n}(\mathrm{r_n}) \end{vmatrix} \qquad (2.10)$$

Where $\frac{1}{\sqrt{\mathrm{n!}}}$ represents the normalization constant. Such an approximation gives useful results, especially in molecular physics. On the other hand, the solution of the equation system (2.10) is still hard for solids.

2.2.4 Thomas-Fermi-Dirac approximation

The predecessor to DFT was the Thomas-Fermi (TF) model proposed by Thomas [143] and Fermi [144] in 1927. In this method, they used the electron density $n(r)$ as the basic variable

instead of the wavefunction. The total energy of a system in an external potential $V_{ext}(r)$ is written as a functional of the electron density $\mathrm{n(r)}$ as:

$$\mathrm{E_{TF}[n(r)] = A_1 \int n(r)^{5/3} dr + \int n(r) V_{ext}(r) dr + \frac{1}{2} \int \int \frac{n(r) n(r')}{|r - r'|} dr dr'} \qquad (2.11)$$

Where the first term is the kinetic energy of the non-interacting electrons in a homogeneous electron gas (HEG) with $A_1 = \frac{3}{10}(3\pi^2)^{2/3}$ in atomic units ($h = m_e = e = \frac{4\pi}{\varepsilon_0} = 1$). The kinetic energy density of a HEG is obtained by adding up all of the free-electron energy state $\mathcal{E}_k = \frac{k^2}{2}$ up to the Fermi wavevector $k_F = [3\pi^2 n(r)]^{1/3}$as:

$$t_0[n(r)] = \frac{2}{(2\pi)^3} \int_0^{k_F} \frac{k^2}{2} \, 4\pi k^2 dk = A_1 n(r)^{5/3} \qquad (2.12)$$

The second term is the classical electrostatic energy of the nucleus-electron Coulomb interaction. The third term is the classical electrostatic Hartree energy approximated by the classical Coulomb repulsion between electrons. In the original TF method, the exchange and correlation among electrons was neglected. In 1930, Dirac [145] extended the Thomas-Fermi method by adding a local exchange term $\mathrm{A_2 \int n(r)^{4/3} \, dr}$ to equation (2.11) with $\mathrm{A_2 = -3/4(\frac{3}{\pi})^{1/3}}$, which leads equation (2.11) to:

$$\mathrm{E_{TFD}[n(r)] = A_1 \int n(r)^{5/3} dr + \int n(r) V_{ext}(r) dr + \frac{1}{2} \int \int \frac{n(r) n(r')}{|r - r'|} dr dr'}$$
$$\mathrm{+ A_2 \int n(r)^{4/3} \, dr} \qquad (2.13)$$

The ground state density and energy can be obtained by minimizing the Thomas-Fermi-Dirac equation (2.13) subject to conservation of the total number (N) of electrons. By using the technique of Lagrange multipliers, the solution can be found in the stationary condition:

$$\mathrm{\delta\{ E_{TFD}[n(r)] - \mu(\int n(r) dr - N)\} = 0} \qquad (2.14)$$

Where μ is a constant known as a Lagrange multiplier, whose physical meaning is the chemical potential (or Fermi energy at T=0 K). equation (2.14) leads to the Thomas-Fermi-Dirac equation,

$$\frac{5}{3}A_1\, n(r)^{2/3} + V_{ext}(r) + \int \frac{n(r')}{|r-r'|}\, dr' + \frac{4}{3}A_2\, n(r)^{1/3} - \mu = 0 \qquad (2.15)$$

which can be solved directly to obtain the ground state density.

The approximations used in Thomas-Fermi-type approach are so crude that the theory suffers from many problems. The most serious one is that the theory fails to describe bonding between atoms, thus molecules and solids cannot form in this theory [146]. Although it is not good enough to describe electrons in matter, its concept to use electron density as the basic variable illustrates the way DFT works.

2.3 The density functional theory

2.3.1 The Hohenberg-Kohn (HK) Theorems

DFT was proven to be an exact theory of many-body systems by Hohenberg and Kohn [147] in 1964. It applies not only to condensed-matter systems of electrons with fixed nuclei, but also more generally to any system of interacting particles in an external potential $V_{ext}(r)$. The theory is based upon two theorems.

The HK theorem I:

The ground state particle density $n(r)$ of a system of interacting particles in an external potential $V_{ext}(r)$. uniquely determines the external potential $V_{ext}(r)$, except for a constant. Thus, the ground state particle density determines the full Hamiltonian, except for a constant shift of the energy. In principle, all the states including ground and excited states of the many-body wavefunctions can be calculated. This means that the ground state particle density uniquely determines all properties of the system completely.

Proof of the HK theorem I:

For simplicity, here **I** only consider the case that the ground state of the system is nondegenerate. It can be proven that the theorem is also valid for systems with degenerate ground states [148]. The proof is based on minimum energy principle. Suppose there are two different external potentials $V_{ext}(r)$. and $V_{ext}'(r)$ which differ by more than a constant and lead to the same ground state density $n_0(r)$. The two external potentials would give two different Hamiltonians, $\hat{H}$ and $\hat{H}'$, which have the same ground state density $n_0(r)$ but would have

different ground state wavefunctions, Ψ and Ψ', with $\hat{H}\Psi = E_0\Psi$ and $\hat{H}'\Psi' = E_0{}'\Psi'$. Since Ψ' is not the ground state of $\hat{H}$, it follows that:

$$\begin{aligned} E_0 &< \langle \Psi' | \hat{H} | \Psi' \rangle \\ &< \langle \Psi' | \hat{H}' | \Psi' \rangle + \langle \Psi' | \hat{H} - \hat{H}' | \Psi' \rangle \\ &< E_0{}' + \int n_0(r)[V_{ext}(r) - V_{ext}{}'(r)]dr \end{aligned} \qquad (2.16)$$

Similarly

$$\begin{aligned} E_0{}' &< \langle \Psi | \hat{H}' | \Psi \rangle \\ &< \langle \Psi | \hat{H} | \Psi \rangle + \langle \Psi | \hat{H}' - \hat{H} | \Psi \rangle \\ &< E_0 + \int n_0(r)[V_{ext}{}'(r) - V_{ext}(r)]dr \end{aligned} \qquad (2.17)$$

Adding equation (2.16) and (2.17) lead to the contradiction

$$E_0 + E_0{}' < E_0{}' + E_0 \qquad (2.18)$$

Hence, no two different external potentials $V_{ext}(r)$ can give rise to the same ground state density $n_0(r)$, i.e., the ground state density determines the external potential $V_{ext}(r)$, except for a constant. That is to say, there is a one-to-one mapping between the ground state density $n_0(r)$, and the external potential $V_{ext}(r)$, although the exact formula is unknown.

The HK theorem II:

There exists a universal functional $F[n(r)]$ of the density, independent of the external potential $V_{ext}(r)$, such that the global minimum value of the energy functional $E[n(r)] \equiv \int n(r)V_{ext}(r)\,dr + F[n(r)]$ is the exact ground state energy of the system and the exact ground state density $n_0(r)$ minimizes this functional. Thus, the exact ground state energy and density are fully determined by the functional $E[n(r)]$.

Proof of the HK theorem II:

The universal functional $F[n(r)]$ can be written as:

$$F[n(r)] \equiv T[n(r)] + E_{int}[n(r)] \qquad (2.19)$$

where $T[n(r)]$ is the kinetic energy and $E_{int}[n(r)]$ is the interaction energy of the particles. According to variational principle, for any wavefunction Ψ', the energy functional $E[\Psi']$:

$$E[\Psi'] \equiv \langle \Psi' | \hat{T} + \hat{V}_{int} + \hat{V}_{ext} | \Psi' \rangle \qquad (2.20)$$

has its global minimum value only when Ψ' is the ground state wavefunction Ψ_0, with the constraint that the total number of the particles is conserved. According to HK theorem **I**, Ψ' must correspond to a ground state with particle density $n'(r)$ and external potential $V_{ext}{}'(r)$, then $E[\Psi']$ is a functional of $n'(r)$. According to variational principle:

$$\begin{aligned} E[\Psi'] &\equiv \langle \Psi' | \hat{T} + \hat{V}_{int} + \hat{V}_{ext} | \Psi' \rangle \\ &= E[n'(r)] \\ &= \int n'(r)\, V_{ext}{}'(r)\, dr + F[n'(r)] \\ &> E[\Psi_0] \qquad (2.21) \\ &= \int n_0(r)\, V_{ext}(r) dr + F[n_0(r)] \\ &= E[n_0(r)] \end{aligned}$$

Thus, the energy functional $E[n(r)] \equiv \int n(r)\, V_{ext}(r) dr + F[n(r)]$ evaluated for the correct ground state density $n_0(r)$ is indeed lower than the value of this functional for any other density $n(r)$. Therefore, by minimizing the total energy functional of the system with respect to variations in the density $n(r)$, one would find the exact ground state density and energy.

The HK theorems can be generalized to spin density functional theory with spin degrees of freedom [149]. In this theory, there are two types of densities, namely, the particle density $n(r) = n_\uparrow(r) + n_\downarrow(r)$ and the spin density $s(r) = n_\uparrow(r) - n_\downarrow(r)$ where $\uparrow$ and $\downarrow$ denote the two different kinds of spins. The energy functional is generalized to $E[n(r), s(r)]$. In systems with magnetic order or atoms with net spins, the spin density functional theory should be used instead of the original one-spin density functional theory. DFT can also be generalized to include temperature dependence [150] and time dependence known as time-dependent density functional theory (TD-DFT) [151].

Although HK theorems put particle density $n(r)$ as the basic variable, it is still impossible to calculate any property of a system because the universal functional $F[n(r)]$ is unknown. This

difficulty was overcome by Kohn and Sham [152] in 1965, who proposed the well-known Kohn-Sham ansatz.

2.3.2 The Kohn-Sham equation

Although DFT has its conceptual roots in the Thomas-Fermi model, DFT was put on a firm theoretical footing by the two Hohenberg-Kohn theorems (H-K) [152]. The original H-K theorems held only for non-degenerate ground states in the absence of a magnetic field, although they have since been generalized to encompass these [153,154]. The Hohenberg-Kohn theorem consist of two main parts:

Theorem I: In a system of N interacting particles under the influence of an external potential $V_{ext}(r)$, the ground state electron density, $n(r)$, uniquely determines the potential, $V_{ext}(r)$. Since $n(r)$ determines $V_{ext}(r)$, then the full ground state Hamiltonian is known. Consequently, $n(r)$ completely determines all the properties of a physical system, such as the eigenfunctions, $\Psi_i(r_1; r_2; \ldots; r_N)$ and the eigenvalues, E_i. In other words, the first theorem states that the energy is a unique functional of the electron density:

$$E[n(r)] = F[n(r)] + \int V_{ext}(r)n(r)d^3r; \qquad (2.22)$$

Theorem II: There exists a functional $F[n(r)]$ for the ground state energy, for any given $V_{ext}(r)$. The global minimum of this functional defines the exact ground state energy of the physical system, and the density that minimizes the total energy is the exact ground state density, $n_0(r)$. The second theorem states that the ground state electron density, $n_0(r)$, minimizes the universal functional, F, such that the electronic energy reaches its minimum value of $E[n_0(r)]$:

$$E[n_0(r)] = F[n_0(r)] + \int V_{ext}(r)\, n_0(r)d^3r\,. \qquad (2.23)$$

It should be noted that $F[n(r)]$ depends purely on the electron density. It does not depend on the external potential, $\int V_{ext}(r)$.

2.3.3 Exchange and correlation functional

Density functional theory reduces the quantum mechanical ground state many-electron problem to self-consistent one-electron form, through the Kohn-Sham equations. The only undetermined component of the equation is the exchange-correlation energy functional, $E_{xc} = E_x + E_c$. This

exchange-correlation energy as a functional of the density must be approximated. In doing so, the local (spin) density approximation (LDA) has long been the standard choice [155] and it is written as:

$$E_{xc}^{LDA} = \int n(r)\varepsilon_{xc}[n(r)]d^3r. \qquad (2.24)$$

Although simple, the LDA results in a realistic description of the atomic structure, elastic, and vibrational properties for a wide range of systems. Yet the LDA is generally not accurate enough to describe the energetics of chemical reactions (heats of reaction and activation energy barriers), leading to an overestimate of the binding energies of molecules and solids in particular.

In the late 90's, Generalized gradient approximation (GGA) have overcome such deficiencies to a considerable extent [156–158] giving for instance a more realistic description of energy barriers in the dissociative adsorption of hydrogen on metal and semiconductor surfaces [159,160]. Gradient corrected or GGA functionals depend on the local density as well as on the spatial variation of the density:

$$E_{xc}^{GGA} = \int n(r)\varepsilon_{xc}[n(r)]F_{xc}[n(r), \nabla n(r)]d^3r. \qquad (2.25)$$

F_{xc} is dimensionless and numerous forms of it exist in literature. The most widely used forms in solid state physics are proposed by Perdew and Wang (PW91) [161] and Perdew, Burke, and Ernzerhof (PBE) [156]. The PW91 is always used in the calculations in the thesis.

Compared to LDA, GGA improves the binding energies, especially when there is chemical bonding between the atoms. The description of the geometries, however, is not universally better. Similar to LDA, screening of exchange hole is not fully taken into account in GGA. Consequently, GGA cannot account for noticeable improvements to the band gap problem or to the calculation of the dielectric constants. The chemical accuracy of the calculated energies is still too limited to achieve the desired chemical accuracy better than 1 kcal/mol or 50 meV/atom in general.

2.3.4 Methods for electronic structure calculations

Using **Fig. 2.1**, the Kohn-sham equation can be solved in a self-consistent manner. This figure consists of the following stages:

1. In the initial stage, an initial density is chosen in $n(r)$ according to the eigen-densities of the solid's free atoms.

2. Subsequently, we proceed to calculate the efficient Kohn-Sham based potential by employing the density determined in step one.

3. Thereafter, we solve the Schrodinger equation in order to obtain the system's wave functions.

4. The density is recalculated.

In the next sections, we discuss shortly some of the most common methods used to calculate the electronic structure of materials.

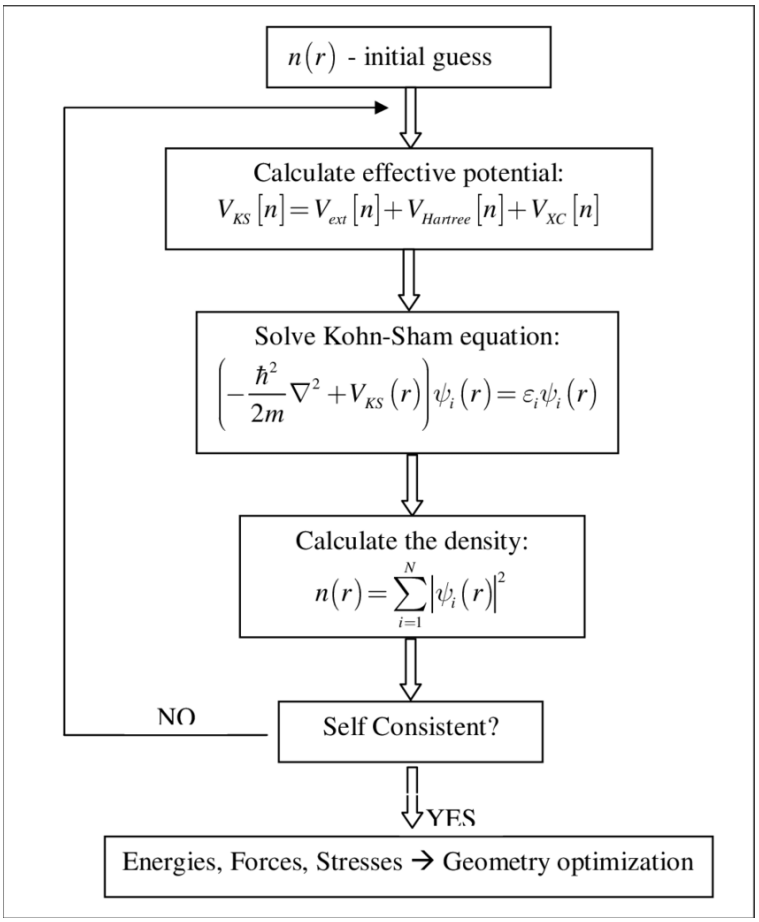

Fig. 2.1: Diagram representing the Kohn-Sham equation solved in a self-consistent way.

2.4 Bloch Theorem

In a condensed system the number of electrons can be assumed as infinite, which makes the solution of the Schrödinger equation very complicated. Felix Bloch, in year 1928, developed a

theorem that enables the consideration of only the electrons within the unit cell to solve the Schrödinger equation [162, 163]. The theorem states that the wave function of an electron within a perfectly periodic potential can be written as:

$$\psi_{nk}(r) = e^{ik.r}\, u_{nk}(r), \qquad (2.26)$$

where k is the wave vector analogous to that of the wave vector in the theory of free electrons, r is a position vector, and $u_{nk}(r)$ is a periodic function that satisfies the boundary condition, $u_{nk}(r) = u_{nk}(r + R)$. The corresponding energy eigenvalue is:

$$\mathcal{E}_n(k) = \mathcal{E}_n(k + K) \qquad (2.27)$$

where K is a reciprocal lattice vector. $\mathcal{E}_n(k)$ is a continuous function, and since the energies associated with the index, n, vary with wave vector, k, we speak of an energy band. All distinct values of $\mathcal{E}_n(k)$ are represented by k values within the first Brillouin zone of the reciprocal lattice.

2.5 Pseudopotential Approach

The majority of the properties of a physical system are determined by its valence electrons rather than its core electrons. Therefore, in an effort to simplify the computational cost of calculations the ionic cores can be treated as frozen in their atomic configurations. In other words, the core electrons are pre-calculated in an atomic environment and kept frozen in the course of the remaining calculations. The pseudopotential (also called effective potential) approach utilizes this idea by replacing the core electrons and the strong ionic potential with a weaker pseudopotential that acts on a set of pseudo wave functions. Although the general ideas behind the pseudopotential approach are similar, there are several procedures to construct pseudopotentials, such as norm-conserving [164–166] and ultrasoft [167, 168]. In this study we make use of the pseudopotentials constructed using the Projector Augmented Wave (PAW) method [169, 170] as will be discussed in the next section.

2.5.1 Projector Augmented Waves: PAW

In 1994, Peter Blöchl developed the so-called Projector Augmented Wave (PAW) method which combines the traditions of augmented wave methods and ultra-soft pseudopotentials into a unified description [169]. The most striking property of the PAW method is that the full all-

electron wave function is kept and therefore the wave functions within the core regions are recovered. Additionally, advanced algorithms are used for a more efficient solution of the generalized eigenvalue problem.

In an effort to overcome the computational costs resulting from all-electron calculations, Blöchl pointed out that the true wave function, Ψ and the pseudo wave function, $\widetilde{\Psi}$, can be linked by a linear transformation:

$$\Psi = T\widetilde{\Psi}, \tag{2.28}$$

$$T = 1 + \sum_j \left(|\Phi_j\rangle - |\widetilde{\Phi}_j\rangle\right)\langle \tilde{p}_j|. \tag{2.29}$$

The proposed transformation operator is shown above (equation (2.29)), where Φ_j , $\widetilde{\Phi}_j$, and $\tilde{p}_j$ are the all-electron partial waves, pseudo partial waves and PAW projector functions, respectively. Projector functions probe the character of the wave function, such as s, p and d-type. Applying this into the all-electron wave function equation one obtains the following expression:

$$|\Psi_n\rangle = |\widetilde{\Psi}_n\rangle + \sum_j \left(|\Phi_j\rangle - |\widetilde{\Phi}_j\rangle\right)\langle \tilde{p}_j|\widetilde{\Psi}_n\rangle. \tag{2.30}$$

As the projector functions are effectively operative only in the core regions, the all-electron wave functions are obtained from the pseudo wave functions by projecting out the core regions and replacing the pseudo partial waves by the all-electron partial waves. In principle, the functions Φ_j , $\widetilde{\Phi}_j$, and $\tilde{p}_j$ can be optimized self-consistently for each system. In practice, these functions are obtained from an atomic calculation and then frozen, such that their effect can be incorporated as a fixed pseudopotential. Consequently, the computational effort is now reduced to a great extent. The PAW technique is surprisingly accurate, i.e., almost comparable to the full all-electron methods.

2.6 QUANTUM ESPRESSO

The density functional theory calculations in my thesis are performed using the software package Quantum ESPRESSO (PWSCF) [171], which stands for op**E**n **S**ource **P**ackage for **R**esearch in **E**lectronic **S**tructure, **S**imulation, and **O**ptimization. It is freely available to researchers around the world under the terms of the GNU General Public License. The package

includes functions such as self-consistent calculations and atomic relaxation (pw.x), postprocessing (pp.x), atomic-projection (projwfc.x). This code is intended for electronic structure calculations using density function theory. It employs plane wave basis sets and a pseudopotential in its applications. Its functionality ranges from ground state energy and Kohn-Sham orbital calculations, to the calculation of atomic forces, stresses, and structural optimization, molecular dynamics on the ground state Born-Oppenheimer surface, Nudged Elastic Band (NEB) and Fourier String Method Dynamics. Quantum ESPRESSO is also capable of performing other calculations including phonon frequencies and eigenvectors at a generic wave vector, effective charges and dielectric tensors, electron-phonon interaction coefficients for metals, Infrared and Raman (non-resonant) cross-section etc. [172, 173]. The principal benefits of QE versus VASP within the scope of the present study are the following: primarily, QE is capable of identifying vibrational frequencies in both infrared and Raman active modes. Second, the QE mode assignment relies on vibrational frequency degeneracy (single, double or triple). Furthermore, QE shows you which irreducible representation a mode is belonging to. This facilitates the interpretation of Raman and infrared spectra results. Quantum Espresso is currently partitioned into several runners, carrying out various kinds of calculations, despite having several overlapping functions. In general, a singular feature set or Fortran 90 module carries out every particular assignment, although significant exceptions to this rule still exist, which reflect the varying background and design of many of the original constituents. In fact, Quantum Espresso was constructed by fusing and re-engineering various packages.

2.6.1 Sampling of Brillouin Zone

In principle, an infinite number of k-points are necessary to account for infinite number of electrons in a periodic system. Bloch's theorem (**Section 2.4**) reduces the problem of calculating an infinite number of electronic wave functions to a finite number of wave functions for an infinite number of k-points. In practice, one does not need an infinite number of k-points since the electronic wave functions will be almost identical for k-points that are very close to each other. Therefore, a single k-point will be sufficient to represent the wave functions over a particular segment of k-space. In general, structures with high symmetry can be sampled with a reduced k-point set, since it is sufficient to consider the k-points only within the irreducible part of the Brillouin zone. Metallic systems require dense set of k-points for a more accurate determination of Fermi level. There exist several methods to generate suitable k-point sets and

corresponding weights [174]. Using these k-point sets generated by such methods, an accurate approximation of the electronic potential and total energy can be possible at a reduced computational cost. The magnitude of the errors in the calculated results decreases by making use of denser k-point sets.

2.6.2 Convergence Tests

The choice of pseudopotential, cutoff energy for the plane wave basis, and k-points to span the Brillouin zone (BZ), are the three most important factors that determine the quality of the numerical calculations. As mentioned in **Section 2.5.1**, the PAW potentials provide accuracy at a reasonable computational effort. However, there is no global value for the plane wave cutoff energy or a set of k-points that works fine for every individual system. Reliable results can only be obtained if accurate cutoffs (E_{cutoff}) and dense k-points are used. E_{cutoff} purely depends on the chemical elements used in the calculations.

If the material of interest is composed of several chemical elements, then it is appropriate to set E_{cutoff} to that of the value of the element with the highest cutoff. As an example, **Fig. 2.2** shows the calculated total energy values for Li in atomic form (a), and bulk form (b), as a function of E_{cutoff}. Obviously, the E_{cutoff} need to be chosen from the region where the the variation in total energy is negligible while keeping in mind that higher cutoff values require more computational effort. For Li a value of $E_{cutoff} = 320\ eV$ will be an adequate choice. A Similar analysis also needs to be performed for k-point sampling. A system specific k-point mesh should be dense enough the BZ to acquire the convergence in total energy as in the case of E_{cutoff}.

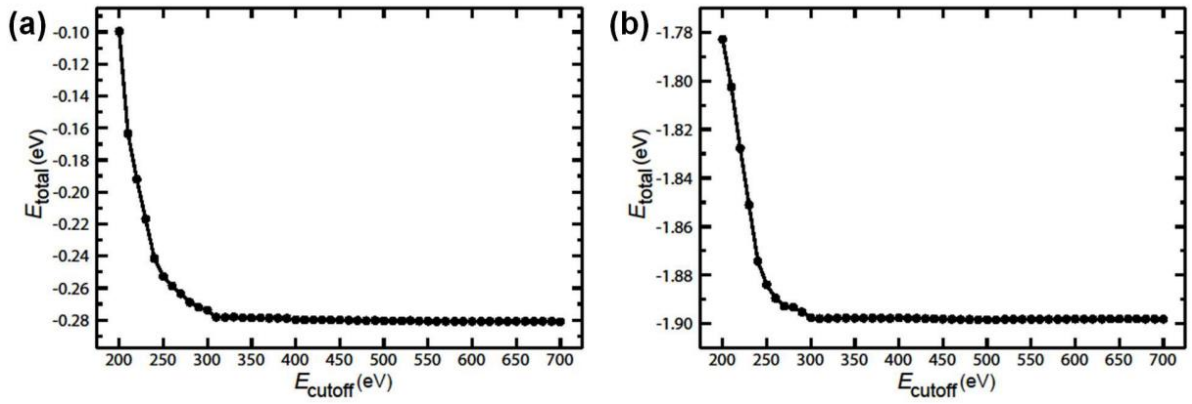

Fig. 2.2: The variation of total energies. E_{cutoff} used in calculation for Li in atomic form (a), and bulk form (b). The energies are given in units of electron volt and the calculated total energies are per Li [175].

2.6.3 Thermodynamics

Thermodynamics is defined as the branch of science that deals with conversion of energy into work and heat and its relation to macroscopic variables such as temperature, volume and pressure. To address the thermodynamics of chemical processes, such as chemical reactions, one can make use of the mathematical methods of Josiah Willard Gibbs [176]. The Gibbs free energy of a system is defined as:

$$G = H - T S, \qquad (2.31)$$

where H is the enthalpy, S is the entropy, and T is the temperature in units of kelvin. The change in the free energy of the system that occurs during a reaction measures the balance between the enthalpy and the entropy. Under constant temperature and pressure, if the change in the Gibbs energy from state A to state B is negative, then state B is said to be thermodynamically more stable than state A. At $T = 0K$, the change in Gibbs energy equals the change in enthalpy, $\Delta G = \Delta H$. The change in enthalpy is defined as the change in the internal energy of the system, ΔU, plus the work that the system has done on its surroundings, $P\Delta V$. Since moreover the change in PV for reactions involving solids is negligible, mostly it is sufficient to focus upon the change in energy, ΔU, where U corresponds to the ground state energy of a system as calculated by DFT.

The relationship then between temperature and free enthalpy is given by the law:

$$\Delta G = \Delta H - T\Delta S \qquad (2.32)$$

where ΔS is the entropy of the dehydrogenation reaction and ΔG the Gibbs standard energy which vanishes for a constant pressure at the decomposition temperature [177]. Thus, the temperature of desorption can be estimated by the following relation:

$$T_{des}=\Delta H/\Delta S. \qquad (2.33)$$

For most dehydrogenation reactions, the value of ΔS is estimated to be in the range $95<\Delta S<140$ J mol^{-1} K^{-1} [178]. Furthermore, under standard conditions of pressure and temperature, the entropy almost equal to $\Delta S=\Delta S(H_2)$ =130($\pm$10) J mol^{-1} K^{-1} [178].

2.6.4 Formation energy

To consider the synthesis of a crystal structure with a defect, we need to know if it is theoretically possible. For this, we calculate the energy of formation of the defect in the mesh. Indeed, creating a defect implies a change in the fundamental energy of the system and this energy difference is the enthalpy of formation of the defect. If this enthalpy of formation is negative then the defect is stable and spontaneous. Conversely, if it is positive then the defect will not form and two crystalline phases of different compositions will be present.

The Density Functional Theory and the chosen computational code are based on the principle of repeating the pattern infinitely to reproduce the periodicity of the structure. In order to limit the interaction between a defect and its replica in the neighboring meshes, we repeat the optimized ideal mesh several times in one or several directions of space. Thus we obtain an extended mesh (also called supercell or supermesh) in which the defect is added. This allows to decrease the interactions between the defects of the neighboring supercells and to have a percentage of defect in the mesh small enough and close to the experiment. The formation of a point defect in a semiconductor or insulator material can be seen as an atomic and electron exchange reaction between a host cell (i.e., a "perfect" reference cell) and atomic and electronic reservoirs. The energy required to create a point defect D in the q charge state is thus [179,180,181] :

$$E_{for}^{D,q}(\Delta E_F) = E_{tot}^{D,q} - E_{tot}^{host} + \sum_i n_i \mu_i + q\left(E_V^{host} + \Delta E_F\right) \quad (2.34)$$

The first two terms represent the energy difference between the cell with defect D of charge q and the host cell. The third term represents the energy of the atomic reservoir, with n_i the number of atom i and μ_i its chemical potential. The fourth term in the equation corresponds to the electronic reservoir, which represents the charge carrier energy in the Fermi level E_F. The formula can be summarized according to **Fig. 2.3**. The host lattice structure is obtained after a structural relaxation of the atomic positions and lattice parameters, while only the atomic positions are optimized in the cells with defect. To obtain the chemical potential μ_i of atom i, it is necessary to know μ_i^0 the chemical potential of hope i in its most stable configuration and $\Delta\mu_i$ its variation with the atmosphere at which the synthesis is performed.

$$\mu_i = \mu_i^0 + \Delta\mu_i \quad (2.35)$$

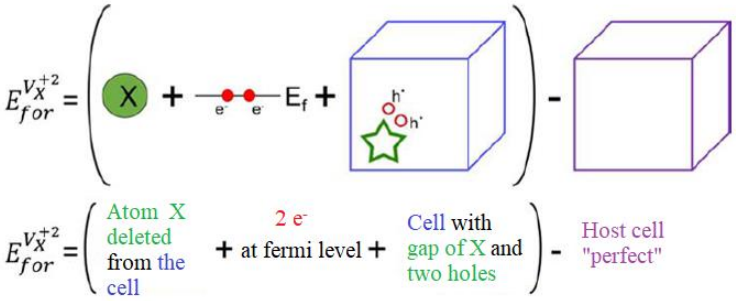

Fig. 2.3: Schematic representation of the formation energy of the gap-type defect of X with a charge state 2 e^-.

For a defect at a given crystallographic site, different charge states are possible. The points where the energies of two charge states are equal define the "transition levels". They are denoted ε (q/q') with q'< q and define the transition level for which the defect changes from a q charge state to a q' charge state. To contribute to the doping of the material, a defect must be stable in a non-neutral charge state, to inject charge carriers into the material. Moreover, if it is possible to have several charge states for a type of defect, only the defects with the lowest positive formation energy, therefore exothermic, will spontaneously create themselves in the material. Defects with negative formation enthalpies will induce a dopability limit (**Fig. 2.4**).

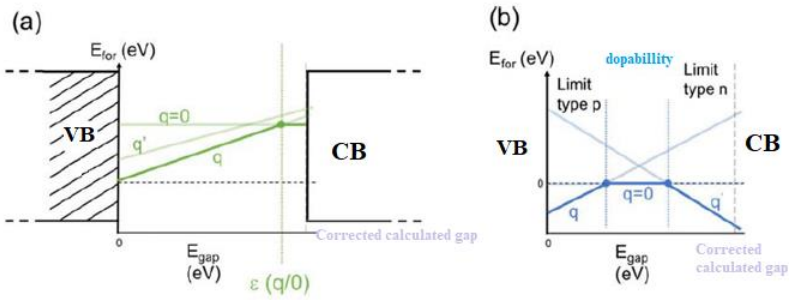

Fig. 2.4: Representation of defect formation energies, charge states and transition levels and (b) p and n dopability limit.

A clear way to determine whether a defect generates the desired doping for an application in optoelectronics is to examine the position of the transition levels.

If a defect has a shallow ε (q/q') transition level between two positive or neutral charge states with q < q', this means that, for any value of Fermi energy in the range, close to the edge of the BC, the defect will be in a positive charge state and thus participate in the n-type doping of the material, as schematized in **Fig. 2.5 -(b)**. It is then a shallow donor level. Conversely, if a defect

has a shallow ε (q/q') transition level and is between two negative or neutral charge states such that q > q', then this defect participates in the p-type doping of the material. In this case, it is a shallow acceptor level, simplified **Fig. 2.5- (c)**.

In the case where the transition level is in the middle of the gap, as shown in **Fig. 2.5- (a)**, then this level acts as a recombination center, detrimental to transport.

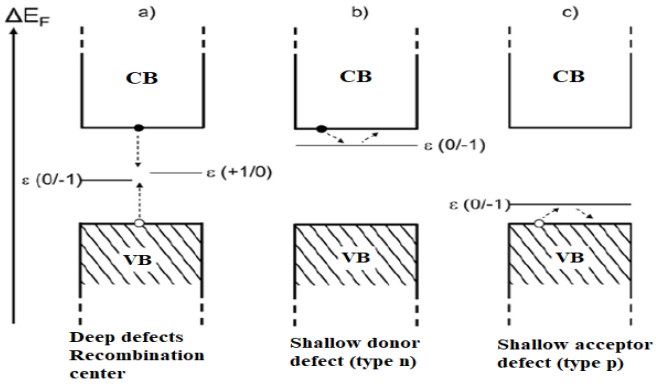

Fig. 2.5: position of defect transition levels in the gap, (a) deep and induce recombination centers, (b) shallow n-type transition level and (c) shallow p-type.

2.6.5 Kinetics

Thermodynamic calculations focus only on the initial and final states of a system and the path by which a change takes place is not taken into account. Intuitively, one might expect strongly exothermic reactions to occur spontaneously, but this is often not true, since many potentially favorable reactions are prohibited by substantial energy barriers. To have a better understanding of how chemical reactions take place, methods based on Transition State Theory (TST) [182] can be used. In principle, the transition rate between two stable equilibria is determined by the lowest energy barrier, also called the reaction barrier (RB). The nudged elastic band method (NEB), which is proposed by Jónsson and Henkelman [183–186], is one of the suitable ways to calculate the RBs. Once the transition states and the RBs are known, other important factors relevant to chemical kinetics, such as, diffusion rates k, and constants D, can be obtained from a vibrational analysis.

The set-up of a NEB calculation starts with a discrete representation of a path from the initial reactant configuration to the final product configuration. The coordinates of atoms for the initial and final configurations are kept fixed during the calculation. Based on these two stable structures, several intermediate configurations (the so-called images) are generated using a

straight-line interpolation. An optimization algorithm is then applied to these images, so that they are relaxed down towards the minimum energy path (MEP). A refinement of MEP and accordingly a more accurate value for the RB is obtained by using denser set of images during calculations. The details on theoretical background of the NEB method as well as its comparison to other saddle point searching methods can be obtained in Refs. [183–187].

2.6.6 Density of States: DOS

The number of states at each energy level that are available to be occupied is called the density of states (DOS). A zero DOS for an energy level means that no states can be occupied. On contrary, a high DOS for an energy level represents that many states are available for occupation. DOS delivers invaluable information about the bonding within solids and in classification of materials as metallic, semiconductor or insulators. Metals or semi metals have non-localized electrons and no gap (separation between valence and conduction band). Materials with a large gap ($\geq\ 4\ eV$) are called insulators, whereas systems with a smaller gap are categorized as semiconductors. In the representation of DOS the specific relation between $\mathcal{E}$ and k must be known to convert between energy and wavevector [168, 169]. In the case of a parabolic relation, such as applies to free electrons, or to electrons in a solid with an isotropic parabolic band structure, the energy is related to the wavevector as: $\mathcal{E} = \frac{\hbar^2}{2\mathrm{m}}\mathrm{k}^2$. Accordingly, the density of states in three dimensions is given by,

$$\mathrm{D}(\mathcal{E}) = \frac{1}{2\pi^2} \cdot \left(\frac{2\mathrm{m}}{\hbar^2}\right)^{3/2} \cdot \mathcal{E}^{1/2} \qquad (2.36)$$

Although DFT seems to systematically underestimate the band gap in insulators and semiconductors by about $30\ -\ 40\%$, it is successful in reproducing the shape of the DOS.

2.6.7 Charge Analysis

In order to make a quantitative conclusion, the identification of the number of electrons on a particular atom would be useful. However, there is no unique way to extract the number of electrons that are associated with a particular atom in a molecule, or in a solid. Many different schemes have been proposed, some are based on population analysis of wave functions (Mulliken population analysis [188], Coulson's charges [189]), and some others are based on partitioning of electron density distributions (Bader analysis [190], Hirshfeld analysis [191]). The charge density analysis of the materials discussed in this thesis are performed via the Bader

analysis [192, 193]. In this approach, molecules or solids are partitioned into atomic volumes, such that the flux of the gradient of the electron density vanishes at every point on the surfaces. That is for every point r_s on the surface $S(r_s)$,

$$\nabla n(r_s) \cdot u(r_s) = 0. \qquad (2.37)$$

where $u(r_s)$ is the unit vector normal to the surface at r_s. The charge density reaches a minimum between atoms, which defines a natural location to separate the atoms from each other. The electron density used in a Bader analysis is obtained via self consistent static DFT calculations based on the equilibrium structure.

Chapter III: Compact structures with graphene sheets for hydrogen storage applications

3 First principles study of BC_7 monolayer compared to graphene as an ultra-high-capacity sheet for hydrogen storage applications

3.1 Introduction

In order to improve the transport, electronic, and storage properties of the graphene sheet, we have designed the BC_7 monolayer by substituting a one carbon atom by boron atom. The BC_7 layer, a new sheet previously announced in 2005 by Lowther [194], is a metallic structure. It is distinguished from the BC_3 layer which is an indirect gap semiconductor. The question naturally arises: what are the characteristics of the BC_7 layer as a hydrogen storage material. In this study, we will compare the BC_7 layer and graphene as a hydrogen storage material.

3.2 Computational details

Here we have carried out first-principles computations through DFT (density functional theory), by means of a program code called Quantum Espresso (QE) [195]. The fundamental package consists of the PAW (projector augmented wave) approach for describing the pseudopotentials [196,197]. In order to construct the exchange-correlation portion, we employed the PBE (Perdewe-Burkee-Ernzerhof) model. Based on the adsorption of the H_2 molecule at BC_7 monolayer, we have built the unit cell, consisting of seven carbon atoms with one boron atom. The Tetrahedron [198] 5 x 5 x 1 grid cells have employed as a means of sample the Brillouin zone for the unit cell BC_7. The convergence threshold of the electrons is fixed at 10^{-10} Ry. The force convergence is assumed to be 10^{-5} (a.u). We used a 15.3 Å vacuum area vertical to the layer surface. The cutoff energy value of 50 Ry is considered for plane waves. The geometrically relaxed monolayer structure BC_7 is depicted in **Fig. 3.1**. The lattice parameter and link angle optimized for the structure are a = b = 5.0447 Å and 120°. Employing xcrysden and VESTA packages [199,200], the BC_7 and H_2BC_7 structures are depicted. To

obtain the diffusion energy, we employed the nudged elastic ban (NEB) approach [201] in order to identify the minima energy path (MEP) consistent with the hydrogen molecule migration pathways over BC_7 monolayer. Thus, the molecule has been constrained to move from the local minima towards a transition state (the saddle point).

We observed while the adsorption of a H_2 molecule at surface layer, the H_2 molecule is polarized with an electric field of the surface layer. Therefore, among the H_2 molecule and the layer there exist a dipolar interaction, in which an adsorbed H_2 molecule and the layer are connected via vdW interaction (van der Waals interaction). For this reason, we considered the vdW correction for our computations, employing Grimme's (DFT-D3) approach [202-204].

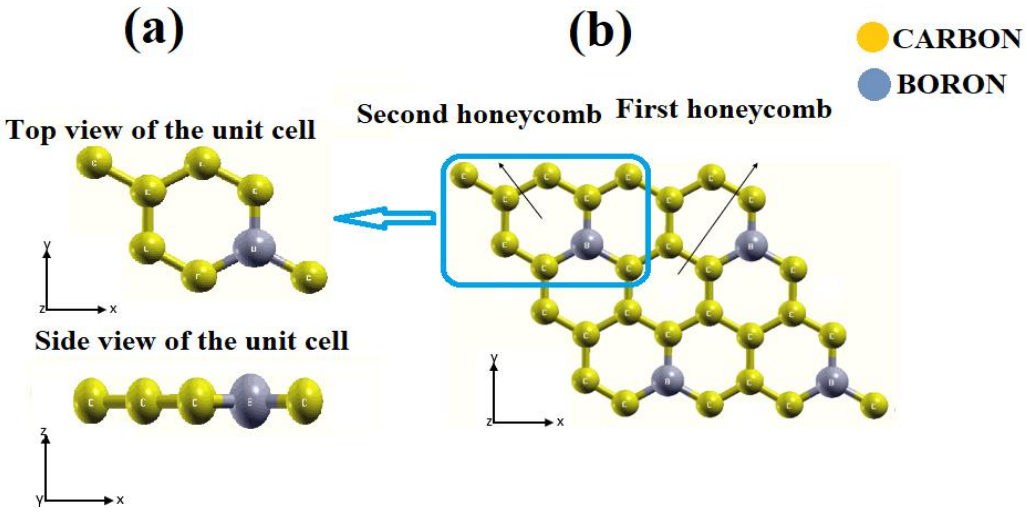

Fig. 3.1: The geometrically relaxed monolayer structure BC_7.

To compute the thermodynamic stability of BC_7 structure, the equation (3.1) was employed [205]:

$$E_f = E_{BC_7} - E_B - E_C \qquad (3.1)$$

wherein E_{BC_7} , E_C and E_B refer to the energies of the BC_7 sheet, the carbon as well as the boron pure, respectively.

The binding force of a H_2 molecule with the BC_7 layer was examined based on the energy of adsorption [206]:

$$E_{ads} = \left(E_{BC_7} + nE_{H_2} - E_{system}\right)/m \qquad (3.2)$$

Whereas "m" is the number of the adsorbed H_2. While E_{BC_7}, E_{H_2} and E_{system} refers to the total energy of the neat BC_7 layer, separated H_2 molecule into the identical layer and the adsorbed H_2 molecule onto the BC_7 layer, respectively.

The charge density difference as well as the Bader charge analysis have been studied the electronic density variation in a specific field, respectively in terms of the visualization and the calculation. Both the charge density difference and the Bader charge analysis were determined by assuming the charge density mean (charge) of both the composite and separate patterns. The density difference of charge as well as the charge analysis of Bader have been provided as terms in equations (3.3) and (3.4) [207], respectively. As these, they have been applied in order to find the apparent adsorption process happening in the total system.

$$\Delta\rho = \rho(BC_7–H_2) - \rho(BC_7) - \rho(H_2) \qquad (3.3)$$

$$\Delta Q = Q(BC_7–H_2) - Q(BC_3) - Q(H_2) \qquad (3.4)$$

In this, $\Delta\rho$ and ΔQ refer to the variations of the charge density and charge, respectively. Correspondingly, ρ_y and Q_y denote the charge density and charge of system y. The investigated systems in this article are the total BC_7-H_2 system, the BC_7 sheet, and the hydrogen molecule.

The gravimetric hydrogen storage capacity was calculated using equation (3.5):

$$C_g(\%) = \frac{n_H \times m_H}{(n_H \times m_H) + m_{BC_7}} \times 100 \qquad (3.5)$$

While m_{BC_7} $(m_{BC_7} = (m_C \times n_C) + (m_B \times n_B))$, m_C, m_B, m_H, refer to molecular masses of elements C, B and H, respectively. n_C, n_B, n_H refer to individual element atomic numbers C, B and H atomic numbers, respectively [208].

To verify the storage substrate (BC_7) is stable thermodynamically, the temperature of desorption has been computed based on equation (3.6):

$$T_D = \Delta H / \Delta S \qquad (3.6)$$

While ΔH denotes the H_2 adsorption formation energy on BC_7 sheet, ΔS signifies the entropy of desorption [209] that is supposed as approximately 130.7 J mol^{-1} K^{-1} [210].

3.3 Structure and stability of BC_7

The BC_7 layer structure can be viewed in **Fig. 3.1**. The computed unit cell is outlined with the solid blue line. Clearly, the primitive cell contains 7 atoms of carbon and 1 atom of boron. By way of expediency, the carbon hexagon and the carbon-boron hexagon are referred to as the first and second honeycombs, respectively. We find that the optimized lattice parameter is 5.0447 Å, a little higher compared to the value mentioned for graphene of 4.92 Å [211]. The computed Carbon-Carbon and Boron-Carbon bond lengths obtained in the second honeycomb are 1.4453 Å and 1.4943 Å, respectively, making it also somewhat longer compared to the length of the Carbon-Carbon bond of graphene which is 1.42 Å. Nevertheless, the bond lengths of Carbon-Carbon atoms in the first honeycomb were 1.4237 Å, which is almost equal to graphene's bond lengths (1.42 Å). Because of the atomic radius changes for such atoms, variations occur in the bond lengths. In order to further substantiate that the sheet BC_7 is thermodynamically stable, the energy of formation ($E_{f)}$ is computed using equation (3.1). We found that the computed E_f is approximately -12.58 eV/cell unit, signifies the thermodynamic stability of the BC_7 monolayer.

3.4 Interaction between BC_7 surface and H_2 molecule

3.4.1 Adsorption energy calculations

On the BC_7 layer, we regard the adsorption of single H_2 molecule. A total of 12 distinct adsorption locations on BC_7 sheet are possible, which are 6 vertical locations (Top C (T1), Top B (T2), C−C Bridge (B1), C−B Bridge (B2), C Hollow (H1), and C−B Hollow (H2)) and 6 parallel locations (Top C (T3), Top B (T4), C−C Bridge (B3), C−B Bridge (B4), C Hollow (H3), and C−B Hollow (H4)), as illustrated in **Fig. 3.2**. The partition of two hydrogen atoms has been considered as 0.7432 Å. The binding force of a H_2 molecule with the BC_7 layer was examined based on the energy of adsorption. Hydrogen molecule adsorption energies values of various physisorbed places were identified in **Table 3.1.** From **Table 3.1**, the adsorption energies are quite notable to fall within the region of -0.2 to -0.6 eV, making it the appropriate energy of adsorption for the storage of H_2 molecule based on DOE investigations [212]. Moreover, there is very little variation of adsorption energies for all relevant adsorption positions. The adsorption energy of position H1 (Carbon hexagon) is clearly the most stable one compared with other sites with a value of - 0.2081 eV. It implies the preference position of

the H_2 molecule adsorption is at H1 (Carbon hexagon) position, where the H_2 molecule is perpendicular to the surface. The total energy graphs are plotted in **Fig. 3.3** for the H_2 molecule approach the BC_7 layer for 12 separate positions. The H_2 molecule axis vertical to BC_7 surface can be seen **in Fig. 3.3-(a)** for T1, T2, B1, B2, H1 and H2 locations, whereas **Fig. 3.3-(b)** illustrates the H_2 molecule axis horizontal to BC_7 surface for T3, T4, B3, B4, H3 and H4 locations.

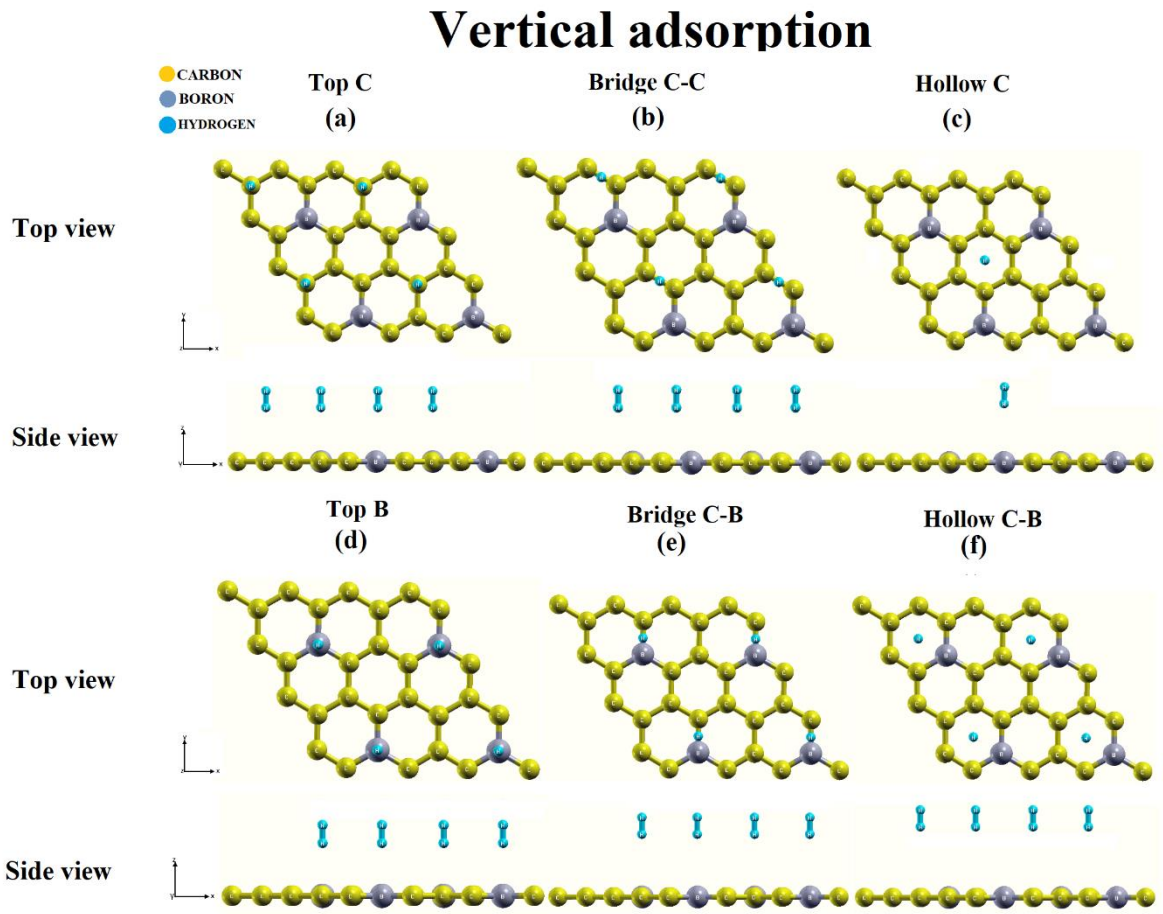

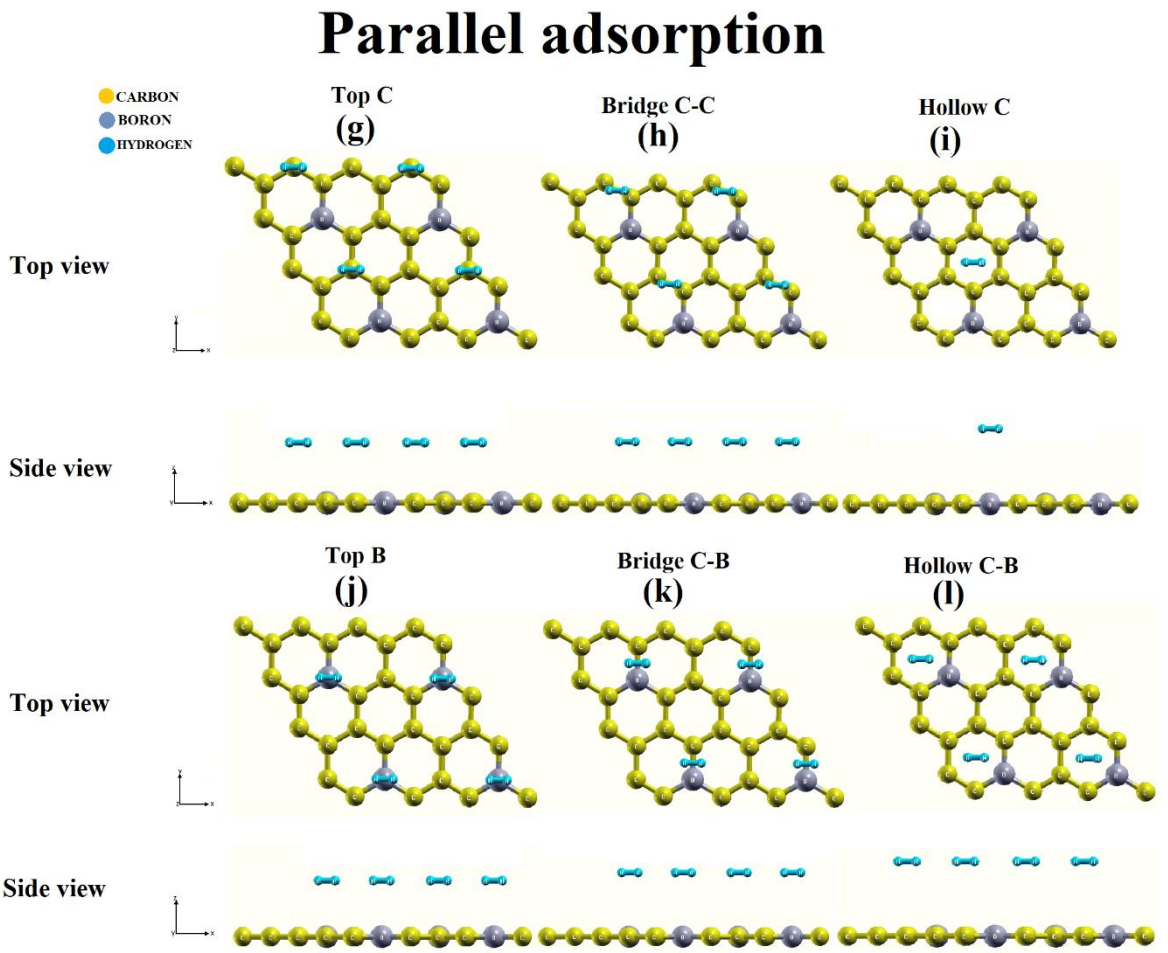

Fig. 3.2: The individual H_2 molecule adsorption at all possible position on BC_7 layer.

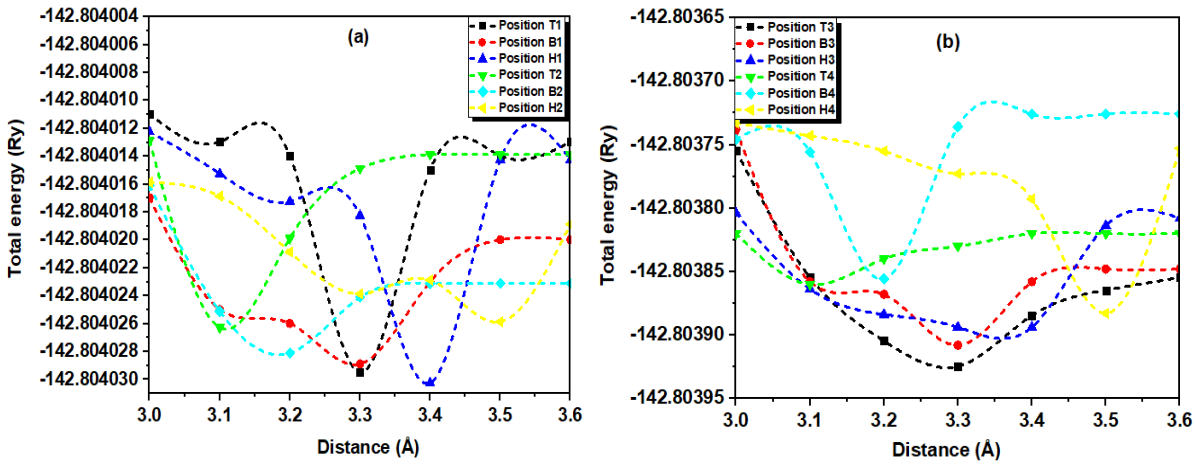

Fig. 3.3: Graph of total energy for a H_2 molecule moving towards BC_7 layer for 12 separate positions.

Table 3.1: The averaged calculated adsorption energies (E_{ads}) of H_2 adsorbed on BC_7 sheet compared to graphene.

		BC_7 monolayer					Graphene			
		Vertical adsorption			Parallel adsorption		Vertical adsorption		Parallel adsorption	
Adsorption sites		**E_{ads} (eV)**	**Distance (Å)**		**E_{ads} (eV)**	**Distance (Å)**	**E_{ads} (eV)**	**Distance (Å)**	**E_{ads} (eV)**	**Distance (Å)**
Top C	**T1**	- 0.2080	3.30	**T3**	- 0.2068	3.30	- 0.0267	3.30	- 0.0256	3.30
Top B	**T2**	- 0.2059	3.10	**T4**	- 0.2059	3.10				
Bridge C-C	**B1**	- 0.2075	3.30	**B3**	- 0.2062	3.30	- 0.028	3.20	- 0.0270	3.20
Bridge C-B	**B2**	- 0.2073	3.20	**B4**	- 0.2046	3.20				
Hollow C	**H1**	- 0.2081	3.40	**H3**	- 0.2060	3.40	- 0.028	3.35	- 0.0284	3.35
Hollow C-B	**H2**	- 0.2052	3.50	**H4**	- 0.2056	3.50				

3.4.2 Charge analysis

As a means to comprehend the nature of the adsorption mechanism of H_2 molecules at BC_7 layer, the charge density of H_2 molecules at BC_7 layer has been investigated and represented in **Fig. 3.4**. It can be observed from **Fig. 3.4** that there is electron depletion occurring on the bottom most hydrogen atom, while a buildup of charge is seen on the farthest hydrogen atom, leading to the hydrogen molecule having a polarization in charge. In addition, a mild charge shifted from BC_7 layer towards the H_2 molecule implies that there is physisorption of the H_2 molecule from the BC_7 sheet. From the charge shifting findings (**Table 3.2**), it was verified that there was a small charge transfer from BC_7 sheet to the H_2 molecule, owing to the interaction dipole-dipole caused by the region of gain or loss of electrons (Van der Waals linkage), by 0.01e for the Top-C atom and the Top-B atom, by 0.02e for the Bridge C−C atoms, the Bridge C−B atoms and the Hollow C−B hexagon, by 0.05e for the Hollow C hexagon. Therefore, owing to the interaction dipole-dipole caused by the region of gain or loss of electrons, it can be concluded that the H_2 molecules have been polarized because of the substrate's electric field. Therefore, there exist vdW interactions among H_2 molecules and BC_7 surface, resulting in significant adsorption of H_2 molecules at BC_7 surface.

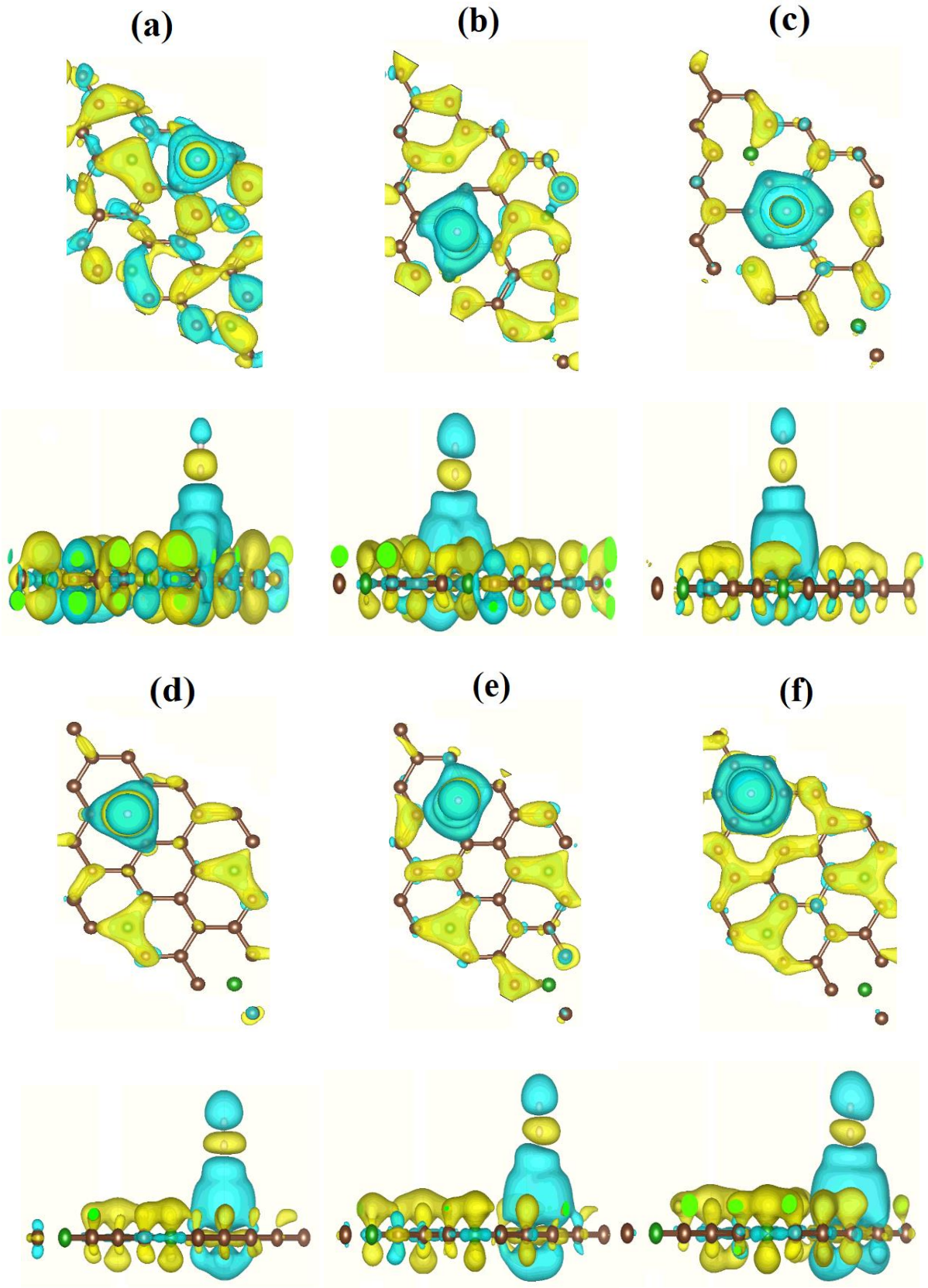

Fig. 3.4: Charge density difference of H_2 molecule adsorption at BC_7 sheet.

Table 3.2: Bader Charge Analysis of the adsorbed unique H_2 molecule at BC_7 sheet.

Adsorption site	ΔQ	
	H' (bottom atom)	H" (far atom)
Top C	0.99(+0.01)	1.01
Bridge C–C	0.98(+0.02)	1.02
Hollow C–C	0.95(+0.05)	1.05
Top B	0.99(+0.01)	1.01
Bridge C– B	0.98(+0.02)	1.02
Hollow C– B	0.98(+0.02)	1.02

3.5 Several hydrogen molecule adsorptions on BC_7 monolayer

3.5.1 Enhancement of hydrogen molecule and gravimetric capacity calculation

In order to enhance the capacity of hydrogen storage, we tried to adsorb some more hydrogen molecules at the surface of BC_7. Subsequently, we moved the systems to 2 molecules of hydrogen and allowed them to pass once again via the optimization of structure. In the same way, we placed 3, 4, 5, 6 and 7 molecules of hydrogen at BC_7 and relaxed the entire system. It was noted that a coherent pattern of change happens within the adsorption energy and the bond length of the H_2 molecule was slightly extended by 0.0088 Å. Well, now the adsorption is carried out with eleven hydrogen molecules (**Fig. 3.5**), when it became full saturated, the value of energy of adsorption achieved -0.2200 eV (see **Fig. 3.6**). Thereafter, when we further moved to the twelfth hydrogen molecule, the value of energy of adsorption got considerably lower up to -0.1117 eV, meaning that it is outside the range of typical 0.2 eV/H_2-0.6 eV/H_2 [212] (see **Table 3.3**). By using equation (3.5), the gravimetric capacity-based hydrogen storage capacity surpassed the H_2 request of 5.5 wt% to 10.40 wt%, which is largest compared to the previous one achieved in Ref. [213].

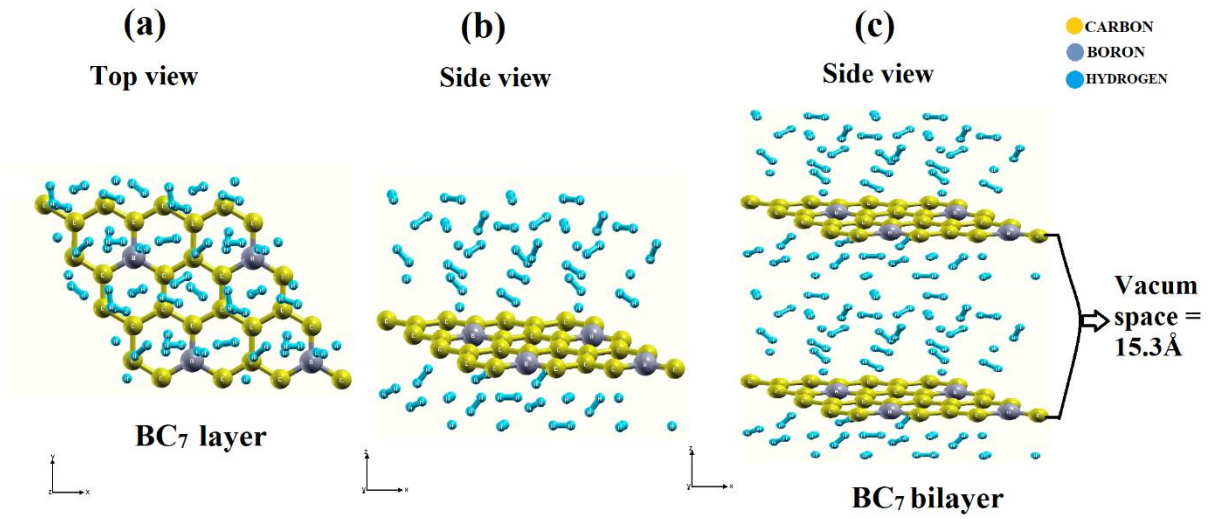

Fig. 3.5: The adsoprtion of eleven hydrogen molecules on BC_7.

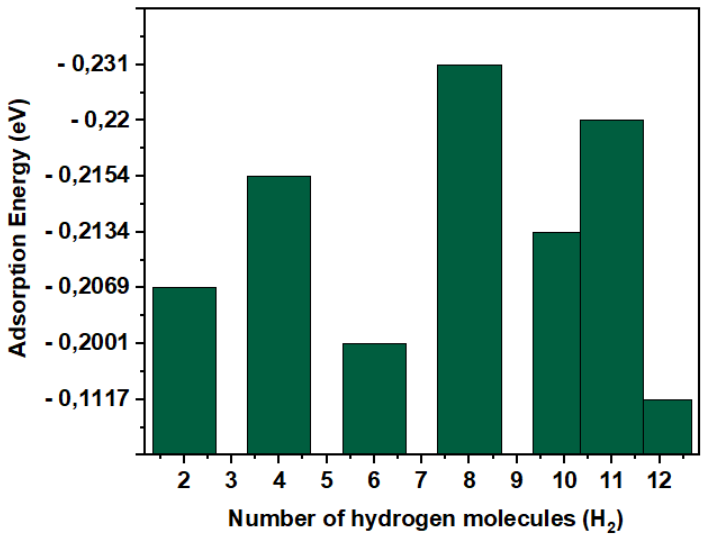

Fig. 3.6: Energy of adsorption versus the amount of hydrogen molecules adsorbed.

Table 3.3: The adsorption hydrogen molecules energies (eV) at BC_7 sheet, with the temperature of desorption T_D (K), and the formation energy ΔH (kJ mol^{-1} K^{-1}).

H_2	BC_7 monolayer				Graphene	
	E_{ads} (eV)	Adsorbate height (Å)	ΔH (kJ mol^{-1} K^{-1})	T_D (K)	ΔH (kJ mol^{-1} K^{-1})	T_D (K)
2^{nd} H_2	- 0.2069	3.40-3.40	- 19,97	166,45	-1.5681	54.71
4^{th} H_2	- 0.2154	3.32-3.32	- 20,79	173,29		
6^{th} H_2	- 0.2001	3.35-3.35	- 19,32	160,981		
8^{th} H_2	- 0.2310	3.41-3.41	- 22,30	185,84		

10^{th} H_2	- 0.2134	3.25-3.25	- 20,60	171,680
11^{th} H_2	- 0.2200	3.49	- 21.24	177.00
12^{th} H_2	- 0.1117	4.67	- 1.784	89,86

3.5.2 Dehydrogenation temperature

Following the confirmation of the structural properties of the H_2 molecule physisorption at BC_7 surface, the thermodynamic properties of this physisorption were examined, including the system stability and the temperature of desorption. Therefore, using the usual thermodynamic equation (3.6), the desorption temperature T_D of the hydrogen molecule was calculated, the providing finding are reported in **Table 3.4**.

Table 3.4: The obtained values of the energy of formation ΔH (kJ mol^{-1} K^{-1}) and temperature of desorption T_D (K).

	H_2/BC_7	**H_2/graphene**
ΔH (kJ mol^{-1} K^{-1})	-21.24	-1.5681
T_D (K)	177.00	54.71

It is observed from **Table 3.4** that H_2/BC_7 possesses a greater thermodynamic stability than H_2/ graphene, based on the values of enthalpies. Consequently, the BC_7 monolayer improved the weak temperature of desorption of pure graphene.

3.5.3 Reversible storage of hydrogen molecule

Hydrogen reversible uptake/release at normal room conditions is highly significant with regard to the application of storage of hydrogen in the field of practical use. Specifically, the desorption temperature (T_D) increases with the adsorption energy for hydrogen molecules (**Fig. 3.7**). Here, in the current research, the desorption temperature (T_D) for diverse adsorption numbers of hydrogen molecules on the BC_7 surface sheet was calculated according to equation (3.6), and detailed in **Table 3.3**. It is observed that the desorption temperature for a variety of systems at various hydrogen numbers varies between about 160 and 177 K, with T_D averaging approximately 177 K. We find that with 11 adsorbed hydrogen molecules, their average adsorption energy is about -0.22 eV, so the calculated T_D is 177 K. This computed desorption temperature value is considerably larger (>5 times) when measured against the critical point of

hydrogen (33.25 K). This discovery proposes that monolayer BC_7 might be able to operate effectively as a hydrogen reversible storage material with a temperature of 177.00 K. Thus, BC_7 sheet improved the weak T_D of graphene.

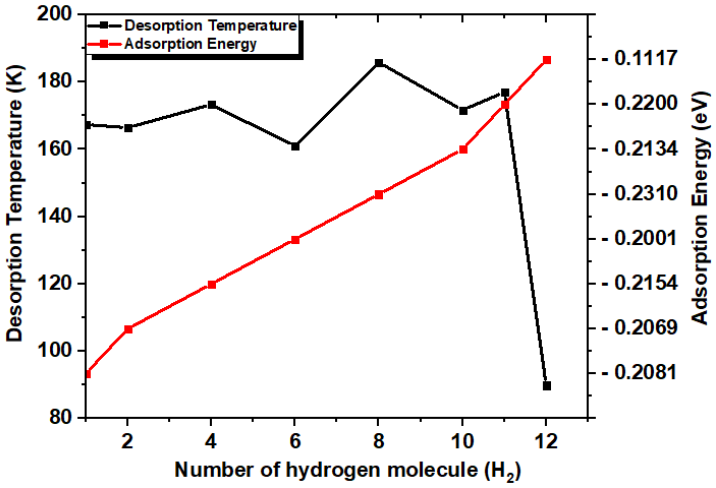

Fig. 3.7: Hydrogen molecules adsorption average for reversible storage at BC_7 layer.

3.6 Density of states

In order to investigate the electronic characteristics of BC_7 sheet, we have graphed the Density of States (DOS) prior to and after the physisorption. As described above, a polarization mechanism (Dipolar-Dipolar interaction) has been used for the physisorption of H_2 molecule. Computation of DOS has verified that hydrogen interacts strongly with the BC_7 structure. According to the total density of states (**Fig. 3.8-(a)**) prior to physisorption, the sheet BC_7 performs in a metallic manner owing to electrons existing at the Fermi level (E_f). The substrate remains metallic after physisorption (**Fig. 3.8-(b)**). Thus, the adsorption of hydrogen does not alter the substrate's character (van der Waals). Based on the partial density of states after adsorption, we can observe a hybridization of C−2p and H−1s states in the valence band. Normally, the higher the electron is moved towards the negative energy, more stable the system is [206,214]. Consequently, we may report the stability of our system after adsorbing eleven hydrogen molecules, owing to the displacement to negative energies of the atomic states.

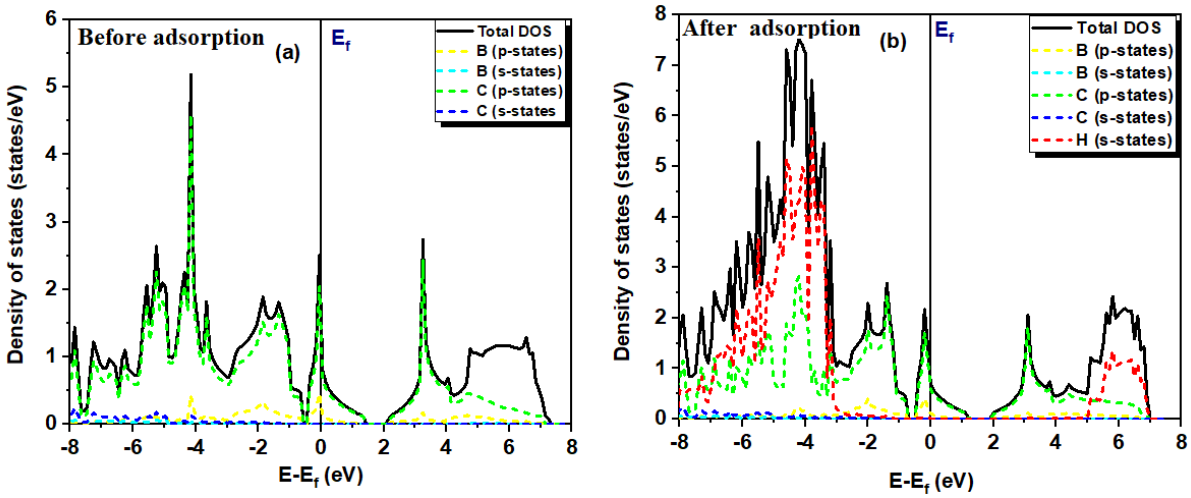

Fig. 3.8: The Density of States (DOS) prior to and after the physisorption of H_2.

3.7 Diffusion of hydrogen molecule on BC_7 monolayer

The diffusion capabilities of hydrogen have been investigated in order to study the migration of hydrogen molecules at BC_7 sheet. Using the NEB process [201], we studied the H_2 molecule diffusion path at BC_7 surface from the primary physisorption site to the transition site, we have graphically represented the barrier results in **Fig. 3.9**, and numerically are given in **Table 3.5**. The obtained barriers found are fairly low in comparison with graphene [215,216] and thus the adsorbed molecules can be quite mobile at BC_7. The main change occurring in these barriers is pattern migration. We can notice from the results that the hydrogen molecule may be able to diffuse more smoothly across the conducted area ("zigzag" sense) rather than across the straight sense in the proximity of (0.0022 eV).

Table 3.5: The energy barriers of H_2 molecule diffusion on BC_7 layer from diverse beginning to ending positions

First state	Primary intermediate state	Second intermediate state	Final state	Diffusion direction	Activation energy (eV) (BC_7)	Activation energy (eV) (Graphene)
H1	**T1**	**T1**	**H1**	Zigzag (**Fig. 3.9 – (a)**)	0.0056	≈ 0.014 [217]
H1	**B1**	**B2**	**H1**	Straight (**Fig. 3.9– (b)**)	0.0039	≈ 0.010 [218]
H1	**T2**	--	**H1**	Zigzag (**Fig. 3.9– (c)**)	0.0022	
H1	**B2**	**B2**	**H1**	Zigzag (**Fig. 3.9– (d)**)	0.032	
H1	**H2**	--	**H1**	Straight (**Fig. 3.9– (e)**)	0.034	

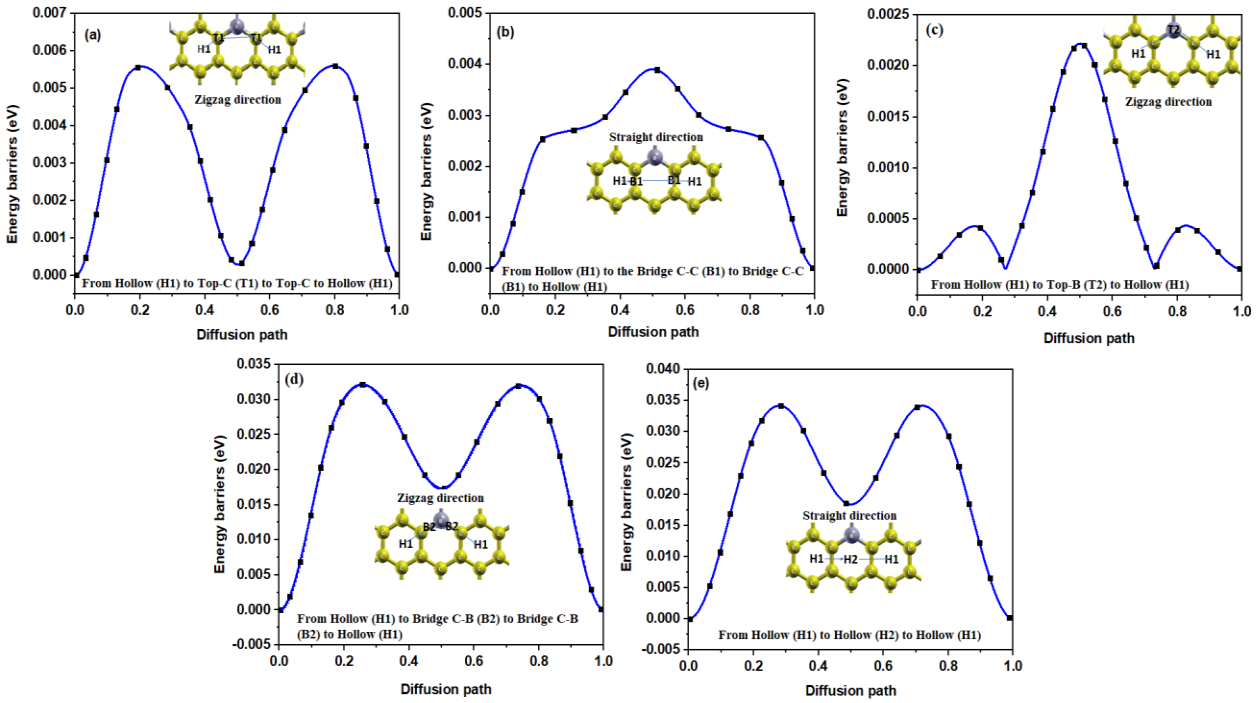

Fig. 3.9: H_2 molecule diffusion path at BC_7 surface from the primary physisorption site to the transition site.

3.8 Conclusion

The structural, transport, electronic, and storage characteristics of the hydrogen on BC_7 monolayer have been systematically examined via DFT. In our DFT investigation involving vdW correction, the BC_7 sheet has strong binding to hydrogen molecules, which means that it has enhanced the low binding energy of graphene. An investigation of the adsorption energy of the system reveals high binding between BC_7 sheet and hydrogen molecules. We also conclude from the Bader charge analysis that there is a transfer of charge between the substrate and the molecule (the polarization mechanism), and this was verified by plots of the charge density difference. Both the typical energy of adsorption area and the feasible temperature of desorption make the BC_7 sheet an effective hydrogen storage system.

4 Physisorption of hydrogen molecule on XC_3 monolayer (X=B, Al, Zn and Ge): First-principles calculations

4.1 Introduction

Graphene has recently received considerable attention due to its many applications. Notably, graphene represents a two-dimensional (2-D) material that is chemically inert [14]. Due to its outstanding properties in electronics, graphene has become widely known. Previous research has shown that graphene can be a suitable material for storing small molecules [19-21]. Therefore, we have designed compact structures with graphene sheets by substituting two carbon atoms with boron, aluminum, zinc and germanium. It would be interesting to understand the interaction between our materials and hydrogen.

4.2 Computational methods

We have used the Quantum Espresso program code [195] with the generalized gradient approximation function, Perdewe-Burkee-Ernzerhof (GGA-PBE) [219]. The pseudopotentials [196,197] were described using projector augmented wave (PAW) methods for the following hydrogen (H), carbon (C) and X (X=Boron, Aluminum, Zinc, Germanium) within the calculations. To adsorb the hydrogen molecule on XC_3 materials, the van der Waals interaction has to be considered. Therefore, the dispersion correction for density functions (DFT-D3) has been employed. For giving a comprehensive image of the electronic states, have been computed based on Perdew-Burke-Ernzerhof (PBE). Using a 5 x 5 x 1 central k grid, self-consistent computations were carried out and a 15.3 Å vacuum distance utilized. A 50 Ry plane wave energy cutoff was employed. By the use of xcrysden and VESTA packets [199,200], the XC_3 and H_2-XC_3 structures are represented. The electron convergence threshold is set at 10^{-10} Ry. Based on the cold friction method of tetrahedron for Brillouin-zone integrations [198], the electron occupancies are defined near the Fermi level. The convergence of forces is assumed to be 10^{-5}(a.u). In order to obtain the activation energy, we used the NEB (nudged elastic ban) method [201] to determine the MEP (The minima energy path) which corresponds to the

migration procedures of hydrogen molecules on the XC_3 monolayers. We forced the molecule to pass between the local minima and the saddle point (transition state).

For the calculation of thermodynamic stability of XC_3 systems, we used formula (4.1) [205]:

$$E_f = E_{XC3} - E_X - E_C \qquad (4.1)$$

Where E_{XC3}, E_X and E_C denote the XC_3 monolayers, pure boron, aluminum, zinc, germanium and carbon energies, respectively.

Both the charge density difference (CDD) as well as the Bader charge analysis (BCA) have identified the electron density change within a particular area, respectively in both visual and numerical terms. The CDD and BCA was calculated by taking the average charge density (charge) of the combination and individual structures. The CDD and BCA are given as expressions in equations (4.2) and (4.3) [207], respectively. As such, they have been employed to identify the apparent mechanism of adsorption occurring in the overall system.

$$\Delta\rho = \rho(XC_3–H_2) - \rho(XC_3) - \rho(H_2) \qquad (4.2)$$

$$\Delta Q = Q(XC_3–H_2) - Q(XC_3) - Q(H_2) \qquad (4.3)$$

In which $\Delta\rho$ and ΔQ represent the changes in the density of charge and charge, respectively. Similarly, ρ_x and Q_x refer to the density of charge and the charge of the x-system. In this paper, the studied systems are XC_3-H_2 total system, XC_3 layers, and H_2 molecule.

In order to investigate the adsorption of H_2 on the XC_3 monolayers film, we studied a single H_2 molecule's adsorption energy on XC_3 via the equation [206]:

$$E_{ads} = (E_{XC_3} + nE_{H_2} - E_{total})/n \qquad (4.4)$$

In which $E_{XC_3}, E_{H_2}, E_{total}$ denotes the total energy of neat XC_3 sheets, isolated H_2 molecule within the same sheets and the adsorbed hydrogen molecule on XC_3 sheets.

The hydrogen storage gravimetric capacity was estimated based on equation (4.5):

$$C_g(\%) = \frac{n_H \times m_H}{(n_H \times m_H) + m_{XC_3}} \times 100 \qquad (4.5)$$

Whereas m_{XC_3} $(m_{XC_3} = (m_C \times n_C) + (m_X \times n_X))$, m_C, m_X, m_H, denotes the molar masses of the components of C, X and H, respectively. n_C, n_X, n_H denotes the elements C, X and H atomic numbers, respectively [208].

To explore that the storage medium (XC_3) is thermally stabilized, the desorption temperature was calculated using equation (4.6):

$$T_D = \Delta H / \Delta S \qquad (4.6)$$

Whereas ΔH denotes H_2 adsorption formation energy at XC_3 surfaces, while ΔS denotes the desorption entropy [209] which is assumed to be around 130.7 J mol^{-1} K^{-1} [210].

4.3 Interaction among XC_3 surfaces and H_2 molecule.

4.3.1 The calculations of adsorption energy

Fig. 4.1 illustrates in detail the optimization of the XC_3 monolayer structures. The black, red and pink solid lines denote the unit cells that we have essentially worked on. The two-dimensional honeycomb lattice of XC_3 is composed of carbon ring atoms (the first honeycomb) connected to rings of X-carbon atoms (the second honeycomb). The space group of the XC_3 layer is P6/mmm, the optimized lattice parameters for BC_3 is 5.172 Å with a bond angle of 120.04°, for AlC_3 is 5.14 Å with a bond angle of 120°, for ZnC_3 is 5.1498 Å with a bond angle of 120° and for GeC_3 is 5.1488 Å with a bond angle of 120° which is a little higher than the reported value for graphene of 4.92 Å [211]. It was found that the calculated Ef is about -21.83 eV/cell unit, -14.47 eV/cell unit, -8.93 -21.83 eV/cell unit, and -21.83 eV/cell unit for BC_3, AlC_3, ZnC_3, and GeC_3, respectively, showing that XC_3 is thermodynamically stable.

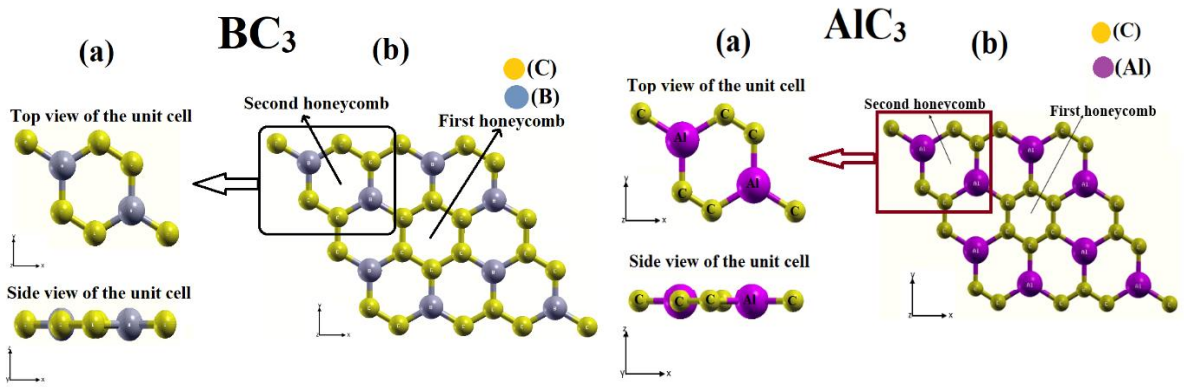

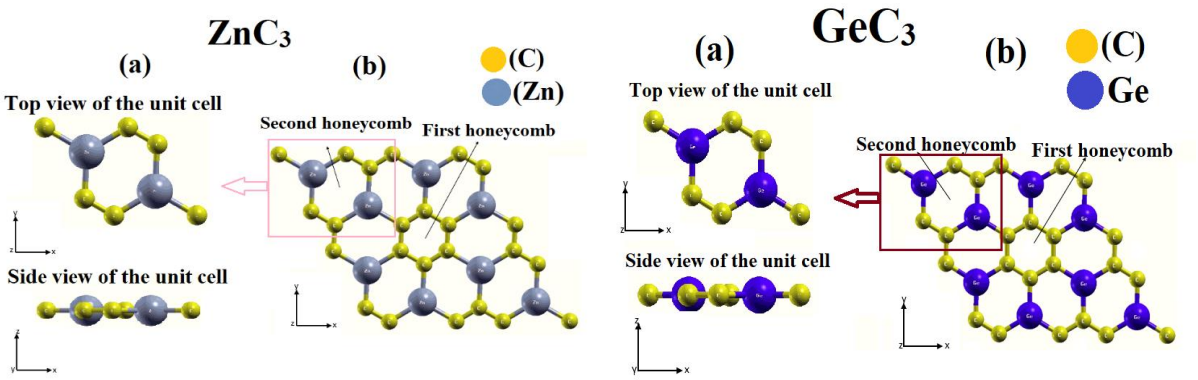

Fig. 4.1: Upper view (a) and side view (b) of the XC_3 unit cell monolayers.

For the purpose of finding the possible steadiest adsorption position, a total of 12 various positions in the high-symmetry pattern shown in **Fig. 4.2** and the distance between two hydrogen atoms was 0.74 Å, 0.7446 Å, 0.7442 and 0.7441 Å for BC_3, AlC_3, ZnC_3 and GeC_3, respectively. We have in fact placed a hydrogen molecule on the unit cell, but in the **Fig. 4.2**, many hydrogen molecules can be seen in each case because of the symmetry. The steadiest adsorption occurred on the carbon hexagon for the whole systems. The computed energy of adsorption at this site was -0.3150 eV, -0.2189 eV, -0.3169 eV, -0.3628 eV for BC_3, AlC_3, ZnC_3 and GeC_3, respectively. The calculated H_2 adsorption energies at various adsorption positions at XC_3 are shown in **Table 4.1**. We noticed from **Table 4.1** that the hydrogen adsorption energies are between -0.2 and -0.6 eV, which is the suitable adsorption energy for hydrogen storage according to DOE studies [212]. **Fig. 4.3** illustrates the total energy curves for the H_2 molecule approaching the XC_3 sheets in twelve different configurations. **Fig. 4.3-(a)** shows the axis of the H_2 molecule perpendicular to the XC_3 sheets for the Carbon-Top (A), Carbon-Carbon-Bridge (B), Carbon-Hollow (C), X-Top (G), X-Carbon-Bridge (H) and X-Hollow (I) configurations, while **Fig. 4.3-(b)** shows the axis of the H_2 molecule parallel to the XC_3 sheets for the Carbon-Top (D), Carbon-Carbon-Bridge (E), Carbon-Hollow (F), X-Top (J), X-Carbon-Bridge (K) and X-Hollow (L) configurations.

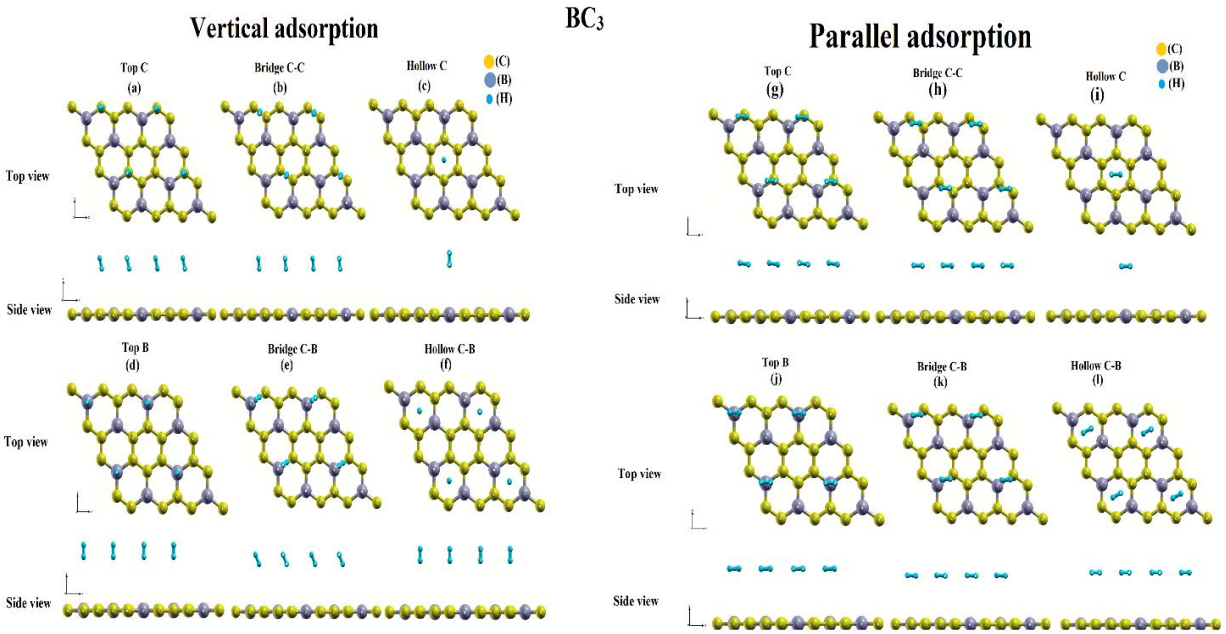
BC3
Vertical adsorption
Parallel adsorption
Top C
(a)
Bridge C-C
(b)
Hollow C
(c)
Top C
(g)
Bridge C-C
(h)
Hollow C
(i)
(C)
(B)
(H)
Top view
Side view
Top B
(d)
Bridge C-B
(e)
Hollow C-B
(f)
Top B
(j)
Bridge C-B
(k)
Hollow C-B
(l)

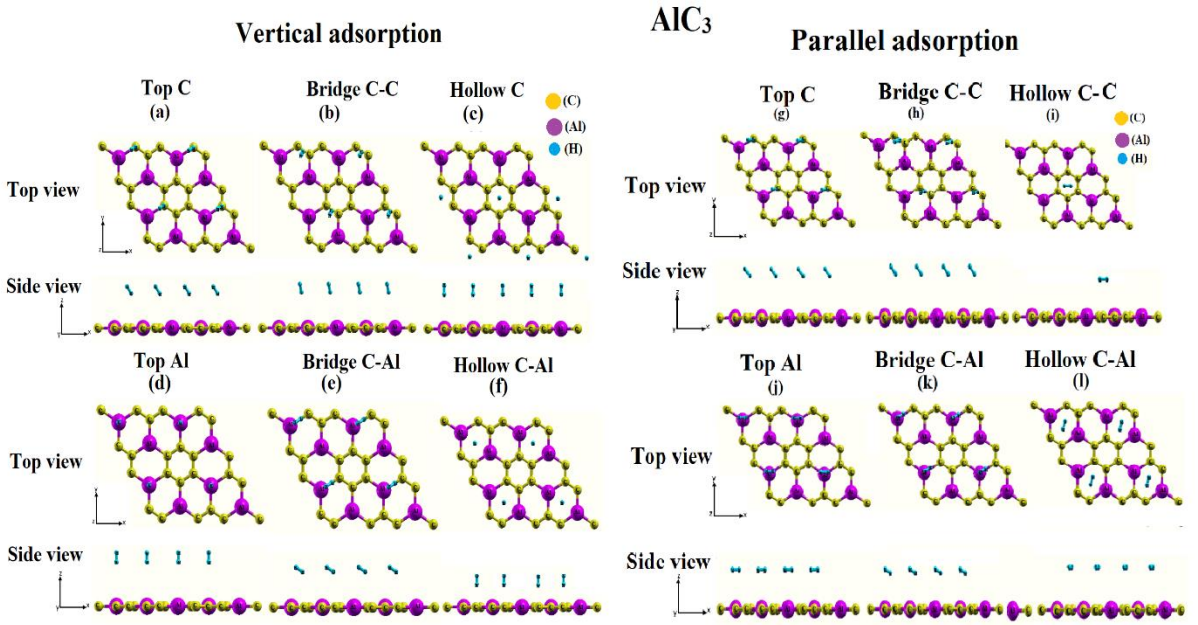
AlC3
Vertical adsorption
Parallel adsorption
Top C
(a)
Bridge C-C
(b)
Hollow C
(c)
Top C
(g)
Bridge C-C
(h)
Hollow C-C
(i)
(C)
(Al)
(H)
Top view
Side view
Top Al
(d)
Bridge C-Al
(e)
Hollow C-Al
(f)
Top Al
(j)
Bridge C-Al
(k)
Hollow C-Al
(l)

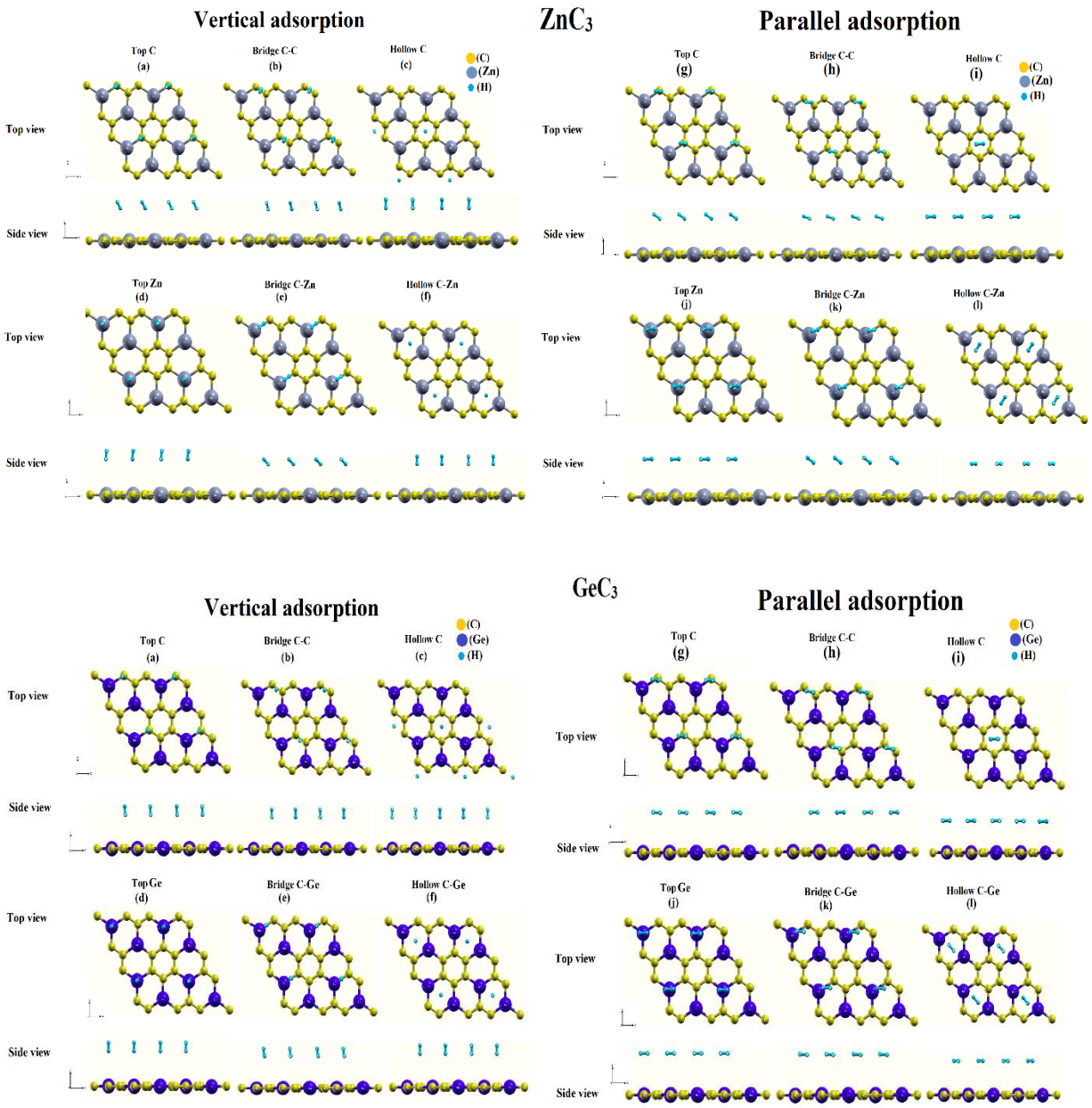

Fig. 4.2: Upper and side views of the H_2 molecule physisorption on the XC_3 monolayers at different configurations.

BC_3

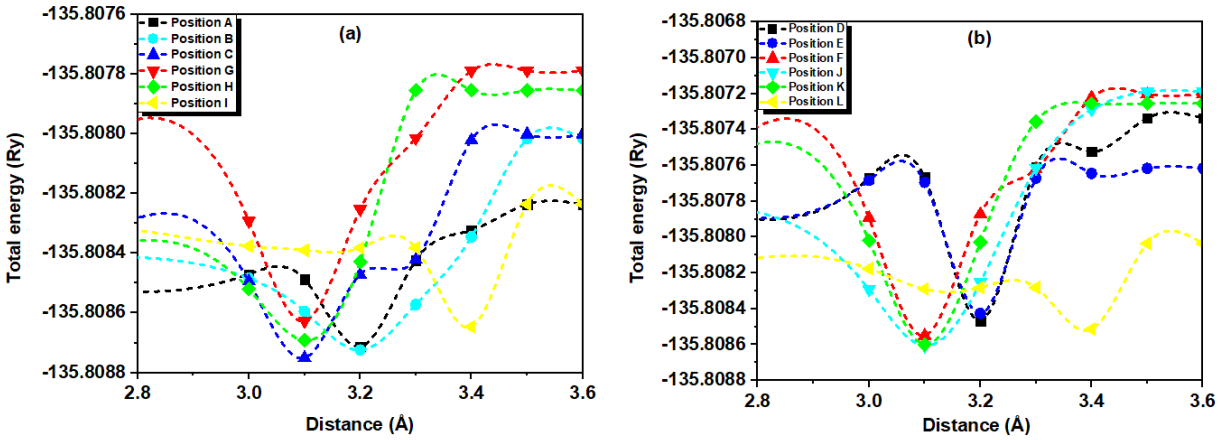

AlC_3

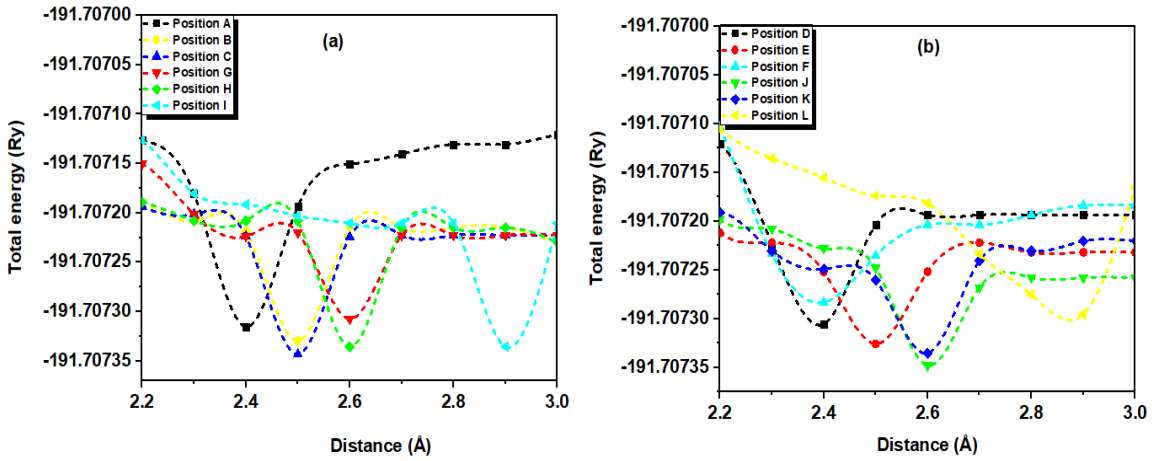

ZnC_3

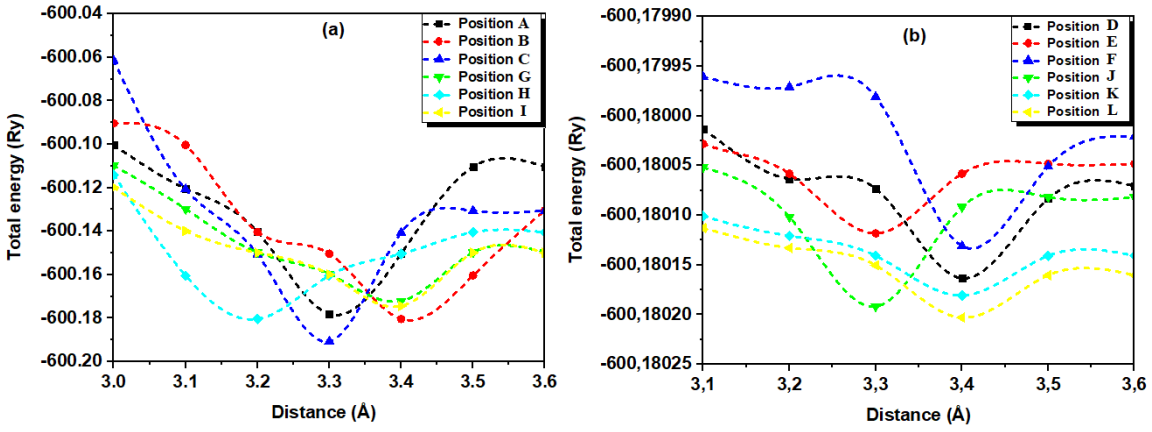

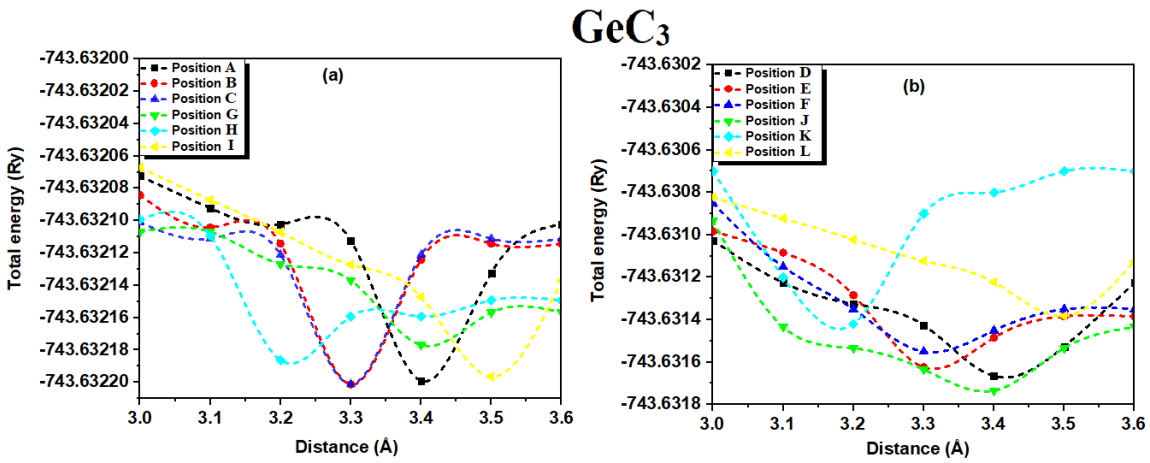

Fig. 4.3: Total energy curves for H_2 molecule approaching to the XC_3 sheets in twelve different configurations.

Table 4.1: Calculations of the most stable distance (Å) as well as the adsorption energy (eV) for the adsorbed H_2 molecule at XC_3 substrates.

	XC_3 sheets							
	BC_3 monolayer		**AlC_3 monolayer**		**ZnC_3 monolayer**		**GeC_3 monolayer**	
	E_{ads} (eV)	**Distance (Å)**	**E_{ads} (eV)**	**Distance (Å)**	**E_{ads} (eV)**	**Distance (Å)**	**E_{ads} (eV)**	**Distance (Å)**
A	- 0.3110	3.20	- 0,2095	2.40	- 0.3125	3.30	- 0.3625	3.40
D	- 0.3090	3.20	- 0,2096	2.40	- 0.3100	3.40	- 0.3556	3.40
G	- 0.2990	3.10	- 0,2001	2.60	- 0.3053	3.40	- 0.3589	3.40
J	- 0.3107	3.10	- 0,2168	2.60	- 0.3141	3.30	- 0.3571	3.40
B	- 0.3120	3.20	- 0,2119	2.50	- 0.3133	3.40	- 0.3627	3.30
E	- 0.3080	3.20	- 0,2117	2.50	- 0.3047	3.30	- 0.3551	3.30
H	- 0.3109	3.10	- 0,2149	2.60	- 0.3139	3.20	- 0.3606	3.20
K	- 0.3106	3.10	- 0,2166	2.60	- 0.3140	3.40	- 0.3498	3.20
C	- 0.3150	3.10	- 0,2189	2.50	- 0.3169	3.30	- 0.3628	3.30
F	- 0.2930	3.10	- 0,2073	2.50	- 0.3062	3.40	- 0.3546	3.30
I	- 0.3099	3.40	- 0,2165	2.90	- 0.3063	3.40	- 0.3624	3.50
L	- 0.3098	3.40	- 0,2089	2.90	- 0.3147	3.40	- 0.3488	3.50

4.3.2 Density of Charge analysis

To portray the H_2 molecule binding scheme on XC_3, the CDDs (**Fig. 4.4**) have been graphed. Referring to the **Fig. 4.4**, there is an electron loss occurs right at the lowest hydrogen atom,

while a charge build-up occurs right at the distant hydrogen atom, resulting to a charge polarization for the hydrogen molecule. Furthermore, a charge shift of the XC_3 sheets to the hydrogen molecule signifies the presence of physisorption of hydrogen molecule from the XC_3 layers. The charge transfer results (**Table 4.2**) confirmed there is a mild charge shifted from XC_3 structures to hydrogen molecule (Van der Waals bond), by 0.01e, 0.02e, 0.03e and 0.01e for the apex of C atom, 0.01e, 0.01e, 0.02e and 0.01e for the middle point of C-C bond atoms, 0.02e, 0.05e, 0.03 and 0.05e for the hollow of C-C hexagon, 0.01e, 0.04e, 0.03e and 0.04e for the top of X atoms, 0.01e, 0.02e, 0.02e and 0.01e for the middle point of C-X atoms, 0.04e, 0.04e, 0.06e and 0.01e for the hollow of C-X hexagon of BC_3, AlC_3, ZnC_3 and GeC_3 respectively. Thus, implying that hydrogen molecule is physisorbed on XC_3 structure.

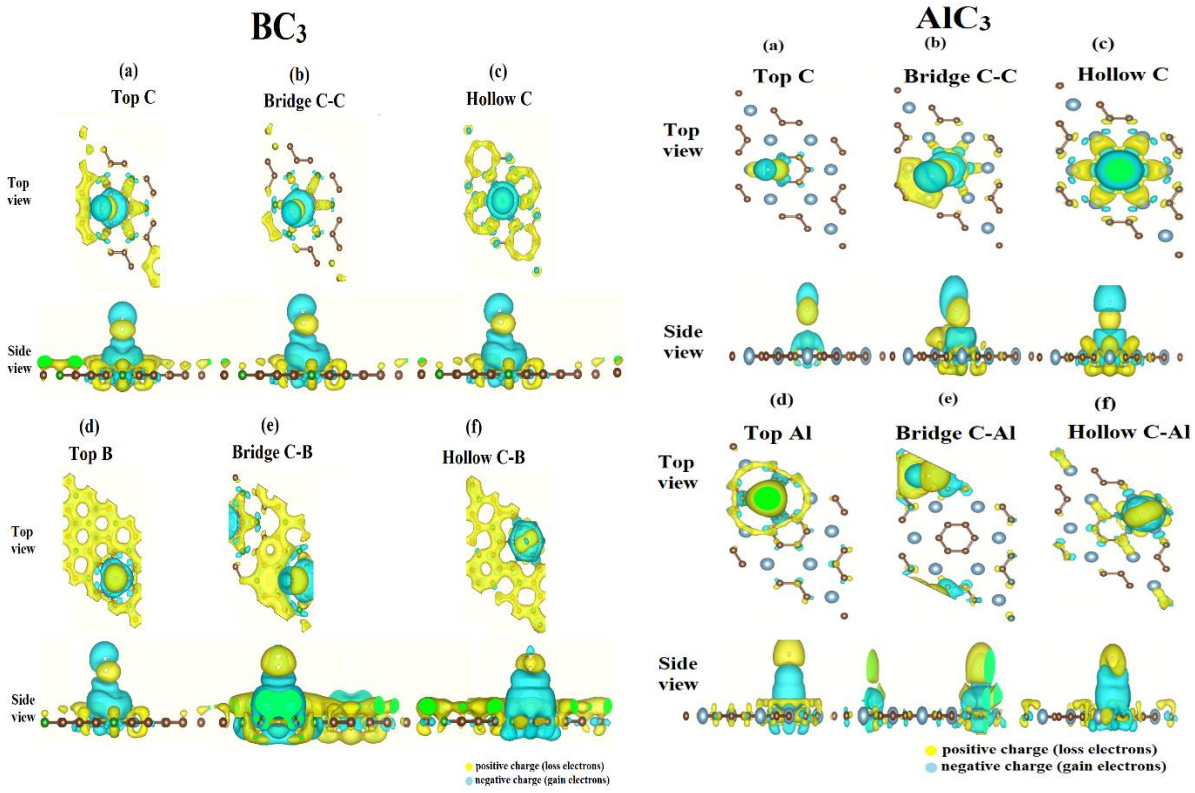

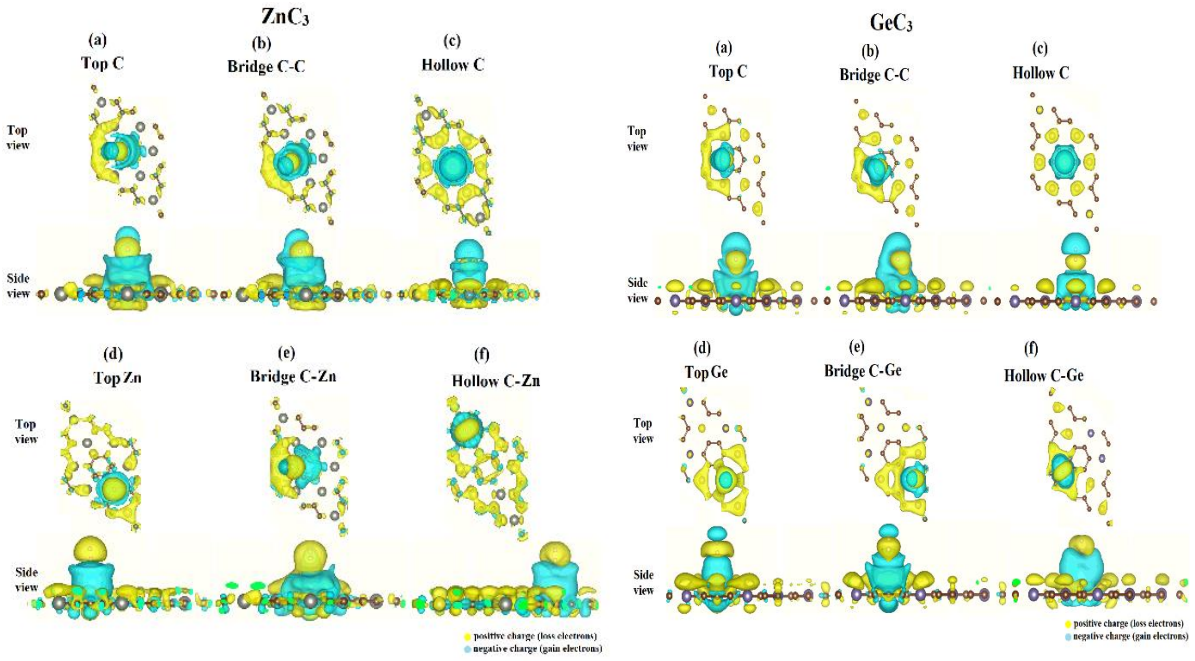

Fig. 4.4: CCD image of H_2 molecule physisorption at XC_3 substrates after adsorption.

Table 4.2: BCA of the physisorbed singular H_2 molecule at XC_3 layers

Adsorption site	**ΔQ**							
	BC_3 monolayer		**AlC_3 monolayer**		**ZnC_3 monolayer**		**GeC_3 monolayer**	
	H' (lowest atom)	**H" (far atom)**	**H' (lowest atom)**	**H" (far atom)**	**H' (lowest atom)**	**H" (far atom)**	**H' (lowest atom)**	**H" (far atom)**
Top C	0.99(+0.01)	1.01	0.98(+0.02)	1.02	0.97(+0.03)	1.03	0.99(+0.01)	1.01
Bridge C–C	0.99(+0.01)	1.01	0.99(+0.01)	1.01	0.98(+0.02)	1.02	0.99(+0.01)	1.01
Hollow C–C	0.98(+0.02)	1.02	0.95(+0.05)	1.05	0.97(+0.03)	1.03	0.95(+0.05)	1.05
Top X	0.99(+0.01)	1.01	0.96(+0.04)	1.04	0.97(+0.03)	1.03	0.96(+0.04)	1.04
Bridge C– X	0.99(+0.01)	1.01	0.98(+0.02)	1.02	0.98(+0.02)	1.02	0.99(+0.01)	1.01
Hollow C– X	0.96(+0.04)	1.04	0.96(+0.04)	1.04	0.94(+0.06)	1.06	0.99(+0.01)	1.01

4.4 Multiple adsorptions of hydrogen molecule on a XC_3 monolayers

4.4.1 Hydrogen molecule enhancement and gravimetric capacity calculation

Following numerous computational studies of different initial H_2 configurations, we further augmented the number of hydrogens on the substrate. This process was performed to reveal the quantity of hydrogen molecules which can be adsorbed on the XC_3 sheets before the destabilization of the system (**Fig. 4.5**). After multiple hydrogen molecule adsorption processes, the distance between the atoms of the hydrogen molecules lengthened slightly by 0.0098 Å, 0.0074 Å, 0.0116 Å and 0.0122 Å for the BC_3, AlC_3, ZnC_3, and GeC_3 substrates respectively. The adsorption energy was identified and traced when numerous hydrogen molecules were added (**Fig. 4.6**). We can notice that the hydrogen molecules maintain their adsorption to the surface with a high binding energy until the 11^{th}, 16^{th}, 17^{th} and 17^{th} molecules up to 0.2552 eV, 0.2152 eV, 0.2679 eV and 0.2787 eV at a distance of 3.62 Å, 3.17 Å, 3.47 Å and 3.52 Å of the BC_3, AlC_3, ZnC_3, and GeC_3 substrates respectively. At the 12^{th}, 17^{th}, 18^{th} and 18^{th} molecule of , the binding energy becomes low 0.103 eV, 0.0681 eV , 0.1220 eV and 0.1168 eV and the distance becomes large 4.86 Å, 4.29 Å, 4.61 Å and 4.82 Å causing the system to become destabilized of the BC_3, AlC_3, ZnC_3, and GeC_3 surfaces respectively (**Table 4.3**) . Employing equation (4.5), the storage capacity of hydrogen based on gravimetric capacity exceeded the demand of 5.5 wt% H_2 to 10.51 wt%, 11.80 wt%, 7.73 wt% and 7.25 wt% of the BC_3, AlC_3, ZnC_3, and GeC_3 layers respectively, and is larger than that obtained previously in ref. [220, 221, 222, 223].

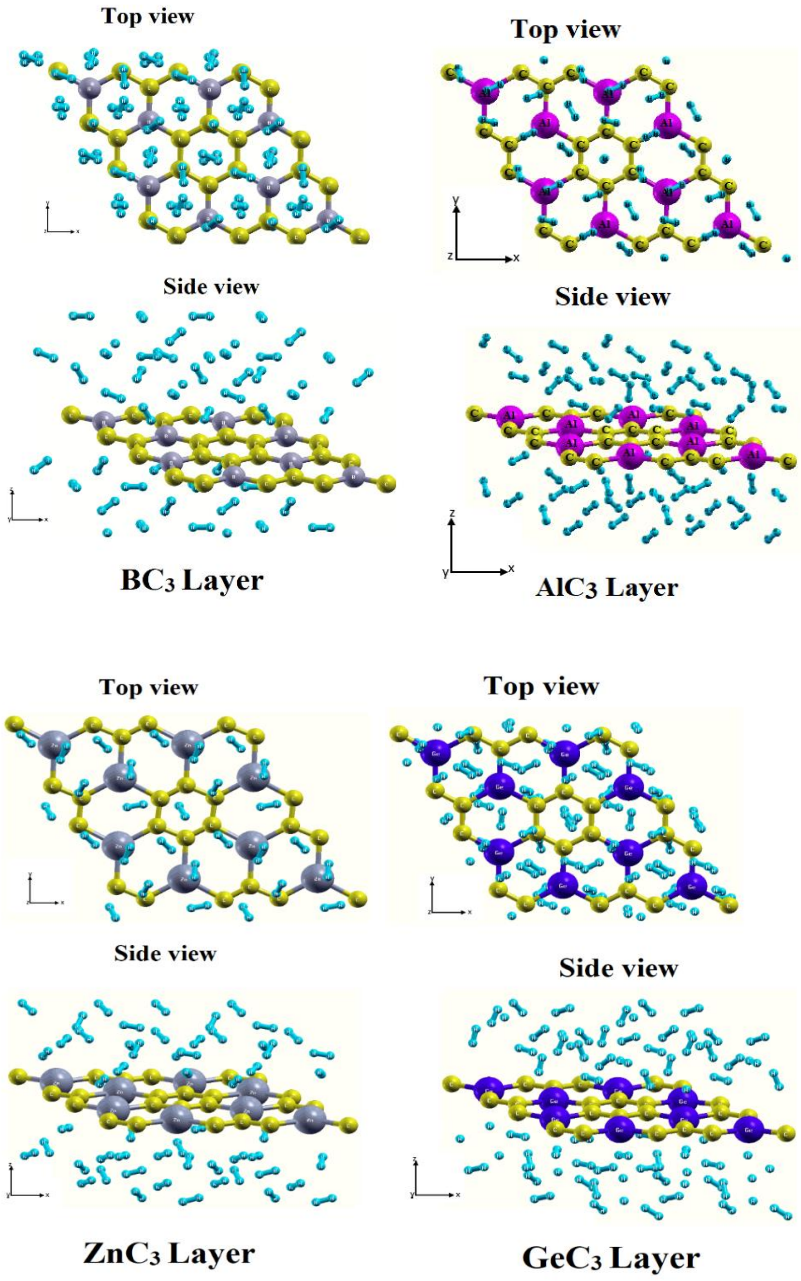

Fig. 4.5: Final setup for the amount of 11, 16, 17 and 17 H_2 on the XC_3 sheets.

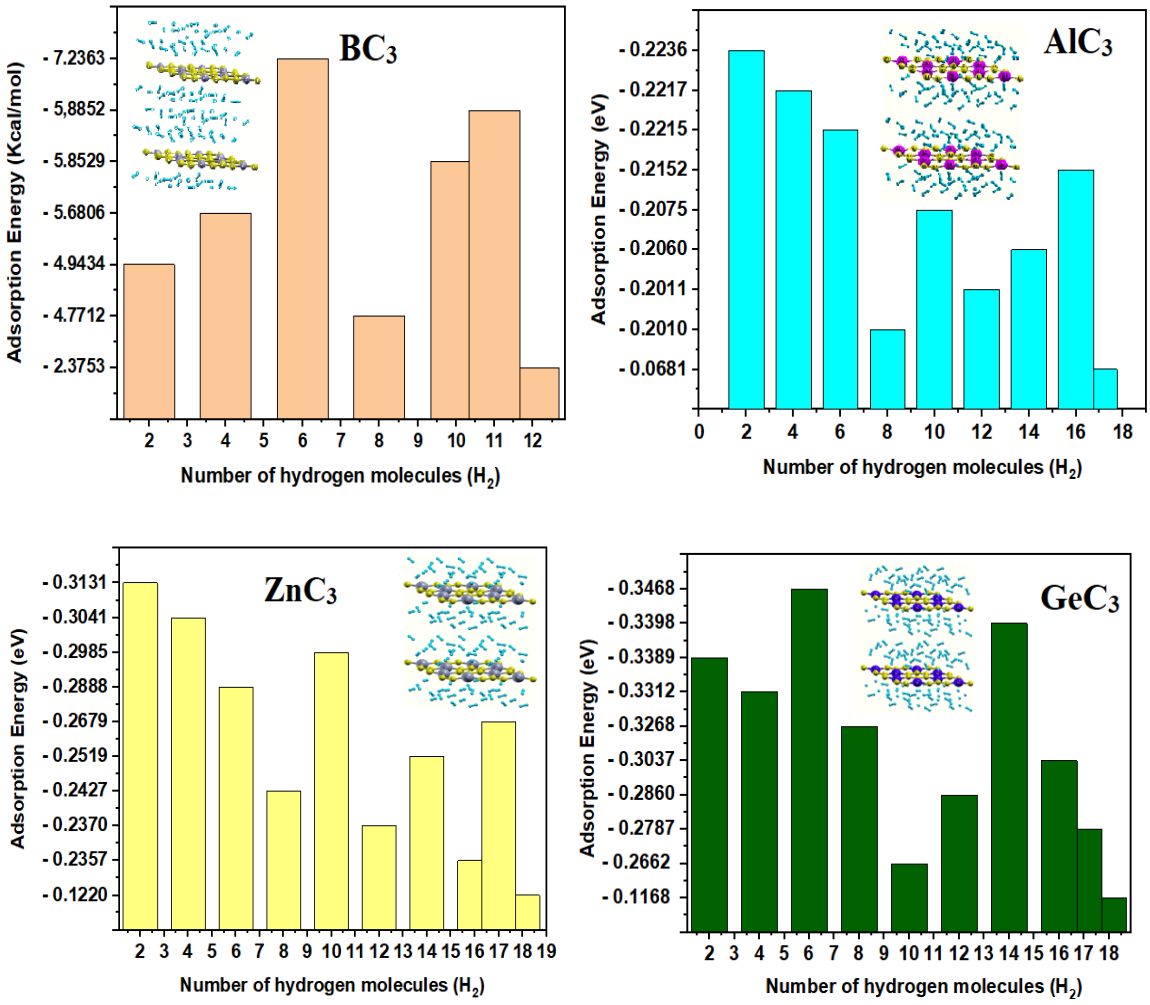

Fig. 4.6: Adsorption energy average.

Table 4.3: The profile of adsorption of H_2 On XC_3 sheet included adsorption energy (eV) and the adsorbate height (Å).

H_2	XC_3							
	BC_3		AlC_3		ZnC_3		GeC_3	
	E_{ads} (eV)	Adsorbate height (Å)	E_{ads} (eV)	Adsorbate height (Å)	E_{ads} (eV)	Adsorbate height (Å)	E_{ads} (eV)	Adsorbate height (Å)
2^{nd} H_2	- 0.2144	3.14-3.12	- 0.2236	3.77-3.77	- 0.3131	3.32-3.32	- 0.3389	3.30-3.30
4th H_2	- 0.2463	2.99-3.15	- 0.2217	2.85-2.85	- 0.3041	3.42-3.42	- 0.3312	3.40-3.40
6th H_2	- 0.3138	3.35-3.40	- 0.2215	2.50-2.50	- 0.2888	3.36-3.36	- 0.3468	3.43-3.40
8th H_2	- 0.2069	3.89-4.08	- 0.2010	3.76-3.76	- 0.2427	3.22-3.22	- 0.3268	3.46-3.41
10th H_2	- 0.2538	3.46-3.39	- 0.2075	3.24-3.24	- 0.2985	3.65-3.65	- 0.2662	3.66-3.66
11th H_2	- 0.2552	3.62	- 0.2065	3.35-3.45	- 0.2873	3.55-3.55	- 0.2475	3.50-3.53

12th H_2	- 0.1030	4.86	- 0.2011	3.73-3.73	- 0.2370	3.75-3.75	- 0.2860	3.20-3.23
14th H_2	--	--	- 0.2060	3.76-3.76	- 0.2519	3.52-3.52	- 0.3398	3.62-3.40
16th H_2	--	--	- 0.2152	3.17	- 0.2357	3.15-3.15	- 0.3037	3.20-3.35
17th H_2	--	--	- 0.0681	4.29	- 0.2679	3.47	- 0.2787	3.52
18th H_2	--	--	--	--	- 0.1220	4.61	- 0.1168	4.82

4.4.2 De-hydrogenation temperature

Once the structural properties of adsorption of H_2 molecule onto XC_3 sheets were ascertained, further investigation of the thermodynamic properties of this adsorption was carried out, especially with respect to the stability as well as to the desorption temperature of the system. We have determined the desorption temperature of H_2 molecule T_D following the standard thermodynamic equation (4.6), the obtained results are presented in **Table 4.4**.

Table 4.4: The profile of adsorption of H_2 On XC_3 sheet included T_D(K) temperature of dehydrogenation (desorption) and ΔH (kJ mol^{-1} K^{-1}) the formation energy.

H_2	**XC_3**							
	BC_3		**AlC_3**		**ZnC_3**		**GeC_3**	
	ΔH (kJ mol^{-1} K^{-1})	**T_D (K)**	**ΔH (kJ mol^{-1} K^{-1})**	**T_D (K)**	**ΔH (kJ mol^{-1} K^{-1})**	**T_D (K)**	**ΔH (kJ mol^{-1} K^{-1})**	**T_D (K)**
2nd H_2	- 20.70	172.50	- 21.59	179.92	- 30.23	251.91	- 32.72	272.67
4th H_2	- 23.78	198.17	- 21.40	178.33	- 23.36	244.68	- 31.97	266.42
6th H_2	- 30.30	252.50	- 21.38	178.17	- 27.88	232.37	- 33.48	279
8th H_2	- 20.00	166.67	- 19.40	161.67	- 23.43	195.28	- 31.55	262.92
10th H_2	- 24.50	204.17	- 20.03	166.92	- 28.82	240.17	- 25.70	214.17
11th H_2	- 24.64	205.33	- 20.01	166.74	- 27.84	231.98	- 23.98	199.85
12th H_2	- 9.950	82.92	- 19.43	161.92	- 22.88	190.69	- 27.61	230.08
14th H_2	--	--	- 19.89	165.75	- 24.32	202.69	- 32.80	273.33
16th H_2	--	--	- 20.80	173.33	- 22.76	189.64	- 29.32	244.92
17th H_2	--	--	- 6.57	54.75	- 25.87	215.55	- 26.91	224.25
18th H_2	--	--	--	--	- 11.78	98.161	- 11.28	94

From the enthalpy values in **Table 4.4**, we discerned a greater thermodynamic stability of H_2/XC_3 in comparison with H_2/graphene. Hence, XC_3 monolayers enhances the low temperature of desorption of pure graphene.

4.4.3 Hydrogen molecule reversible storage

Reversible H_2 adsorption/liberation at room temperature is extremely relevant in terms of H_2 storage applications in practice. Typically, for H_2 molecules, the temperature of desorption (T_D) rises with increasing energy of adsorption (**Fig. 4.7**). At the present study, for H_2 molecules of various adsorption numbers at ZnC_3 layer, the temperature of desorption (T_D) has been determined by means of equation (4.6), the details are presented in **Table 4.4**. We find that the temperature of desorption for various systems under diverse numbers of H_2 varies from approximately 160 to 273 K, with a mean rate of T_D of approximately 205.33 K, 173.33 K, 215.55 K and 224.25 K for the BC_3, AlC_3, ZnC_3, and GeC_3 surfaces respectively. The computed desorption of temperature is 205.33 K, 173.33 K, 215.55 K and 224.25 K with 11 H_2, 16 H_2, 17 H_2 and 17 H_2 molecules adsorbed, since their mean energy of adsorption is -0.2552 eV, -0.2152 eV, -0.2679 eV and -0.2787 eV for the BC_3, AlC_3, ZnC_3, and GeC_3 layers respectively. This calculated T_D value is significantly greater (>7 times) compared to the hydrogen critical point (33 K). This finding suggests that the monolayers XC_3 might function successfully as a substrates to store hydrogen reversibly beyond a temperature of 205.33 K, 173.33 K, 215.55 K and 224.25 K.

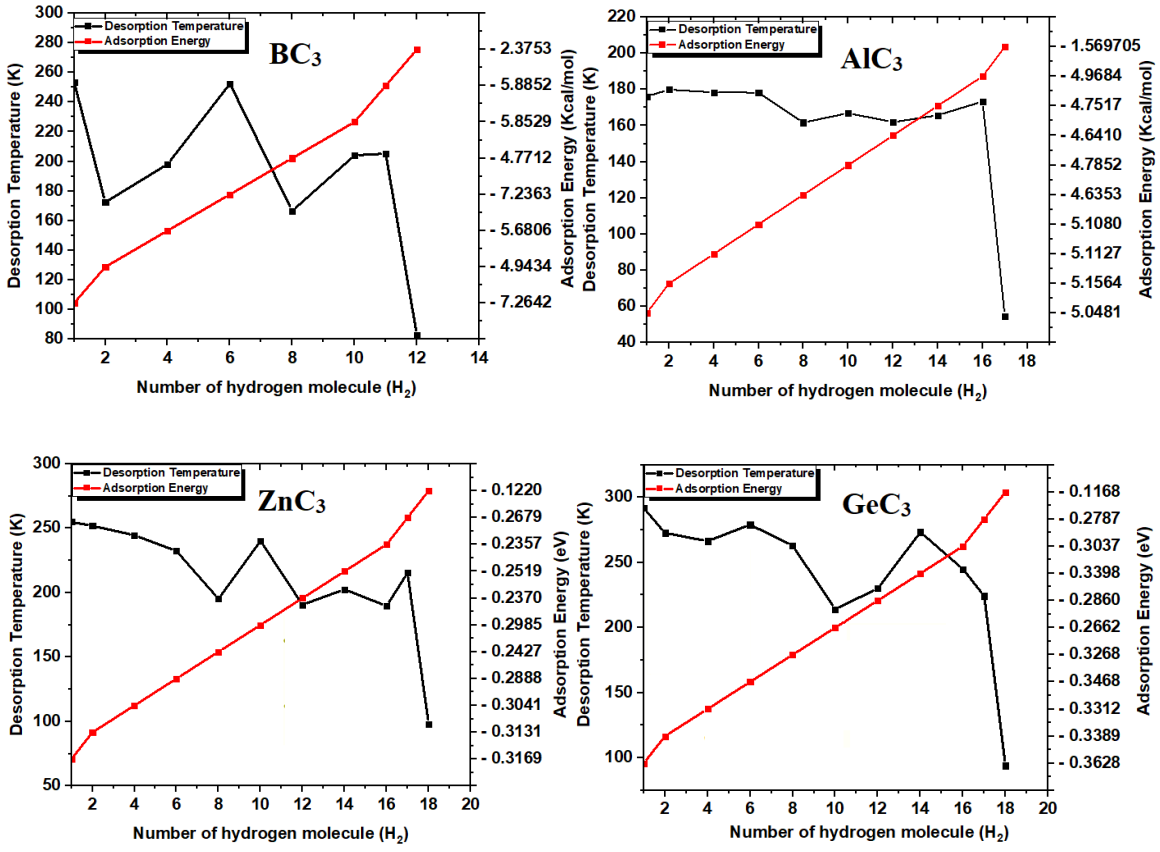

Fig. 4.7: Variation of desorption temperature of XC_3 sheets as a function of the number of adsorbed H_2 molecules with adsorption energy.

4.5 Density of states analysis

Here we study the adsorption of hydrogen at XC_3 sheets. As previously discussed, by a polarization mechanism, the hydrogen molecule was physisorbed. The density of states calculation confirmed the interaction between H_2 and the XC_3 sheets. From the total density of states (**Fig. 4.8-(a)**) before adsorption, the BC_3 and AlC_3 layers behaves in a semiconducting way with an energy of bandgap reaching 0.6707 eV and 1.3669 eV respectively, the ZnC_3 behaves as a metal due to the existence of electrons at the Fermi level (E_f) and the GeC_3 behaves in a semi-metallic way due to the absence of electrons at the Fermi level. After adsorption (**Fig. 4.8-(b)**) it can be noticed that the adsorption of H_2 does not change the nature of the substrates, it keeps their nature. From the partial density of states after adsorption, we can see that the valence band is mainly composed of a hybridization between the C−2p and H−1s states for all systems, except for the ZnC_3 layer which shows another hybridization with the previous ones, a strong hybridization between the Zn−3d and H−1s states. In general, the more the electron is shifted to the negative energy, the more stable the system is [206,214]. Therefore, we can say that our systems are stable after adsorbing the hydrogen molecules, due to the shift of atomic states to negative energies.

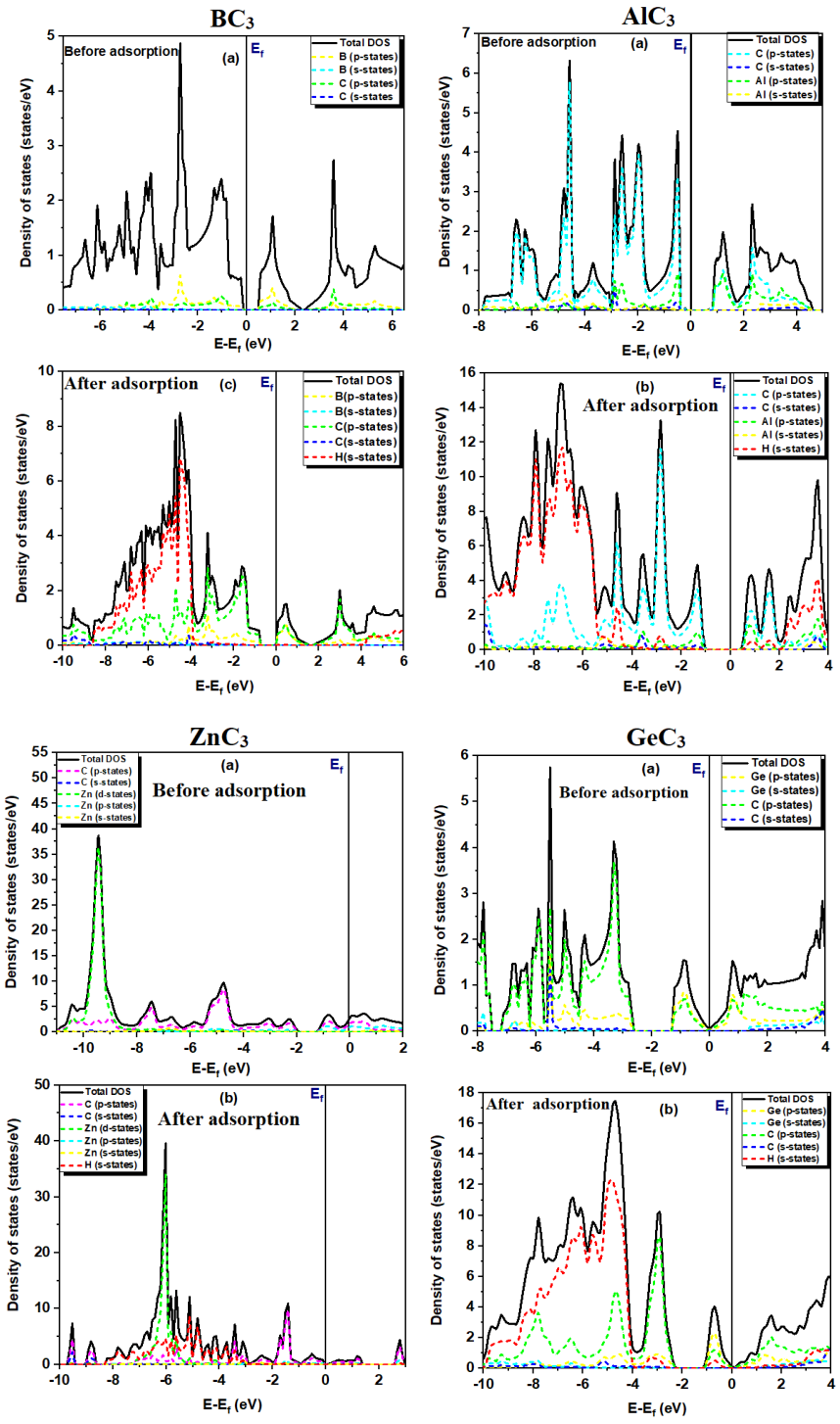

Fig. 4.8: TDOS (total density of states) and PDOS (partial density of states) estimated of XC_3 layer.

4.6 Hydrogen molecule diffusion on the XC_3 monolayers

The studies of the diffusion barriers ΔE_{barr} for H_2 molecule crossing the XC_3 sheets from the most stable position which is the site C, have been estimated as the difference from the beginning state to the adsorbed transition state, i.e., through the position A, B, G, H or I. Via

the NEB method, the calculation of the barrier was plotted in **Fig. 4.9** and the results are shown in **Table 4.5**. Due to the small energy barriers, the adsorbed hydrogen molecules are predicted to be fully mobile across the XC_3 surfaces.

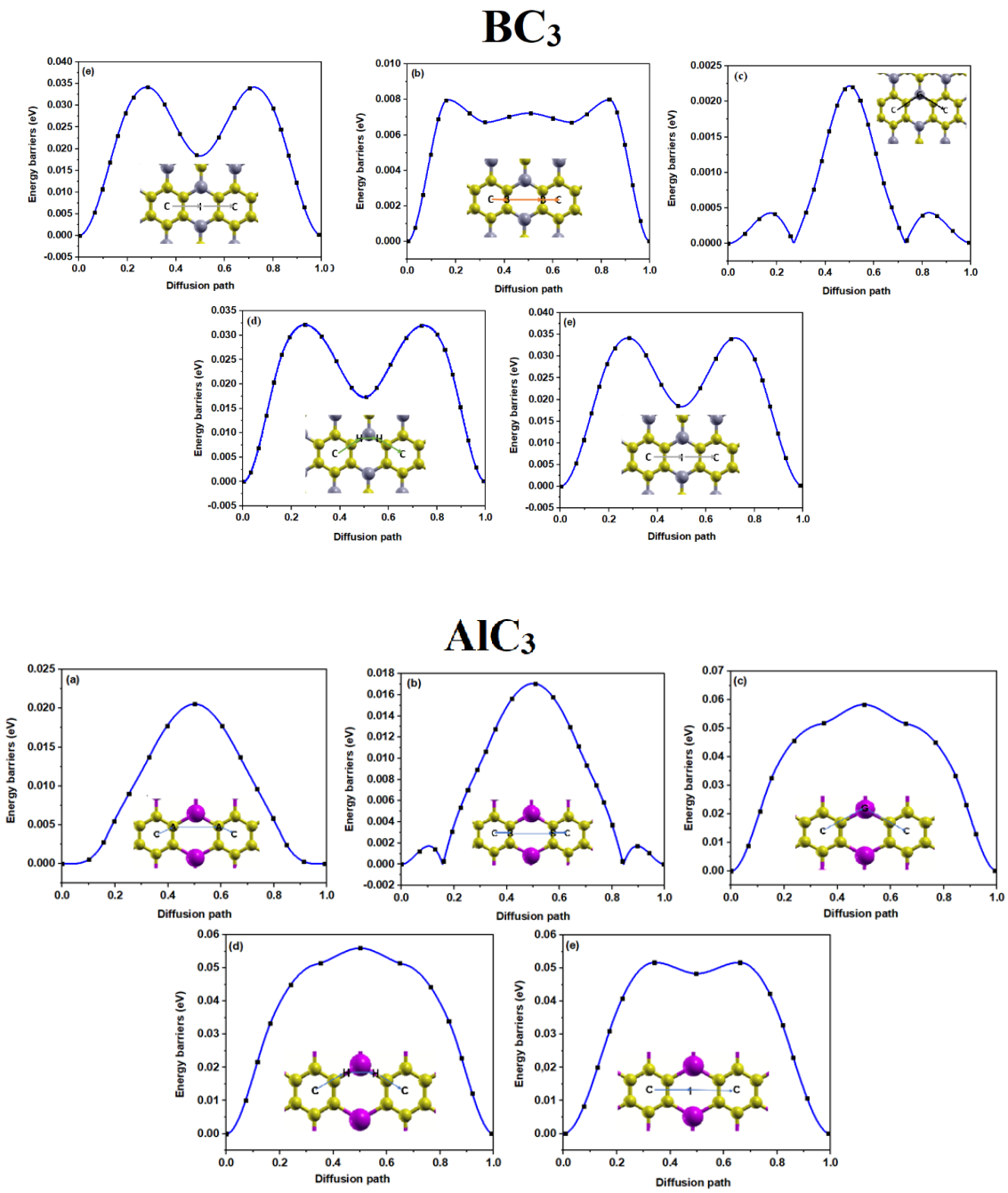

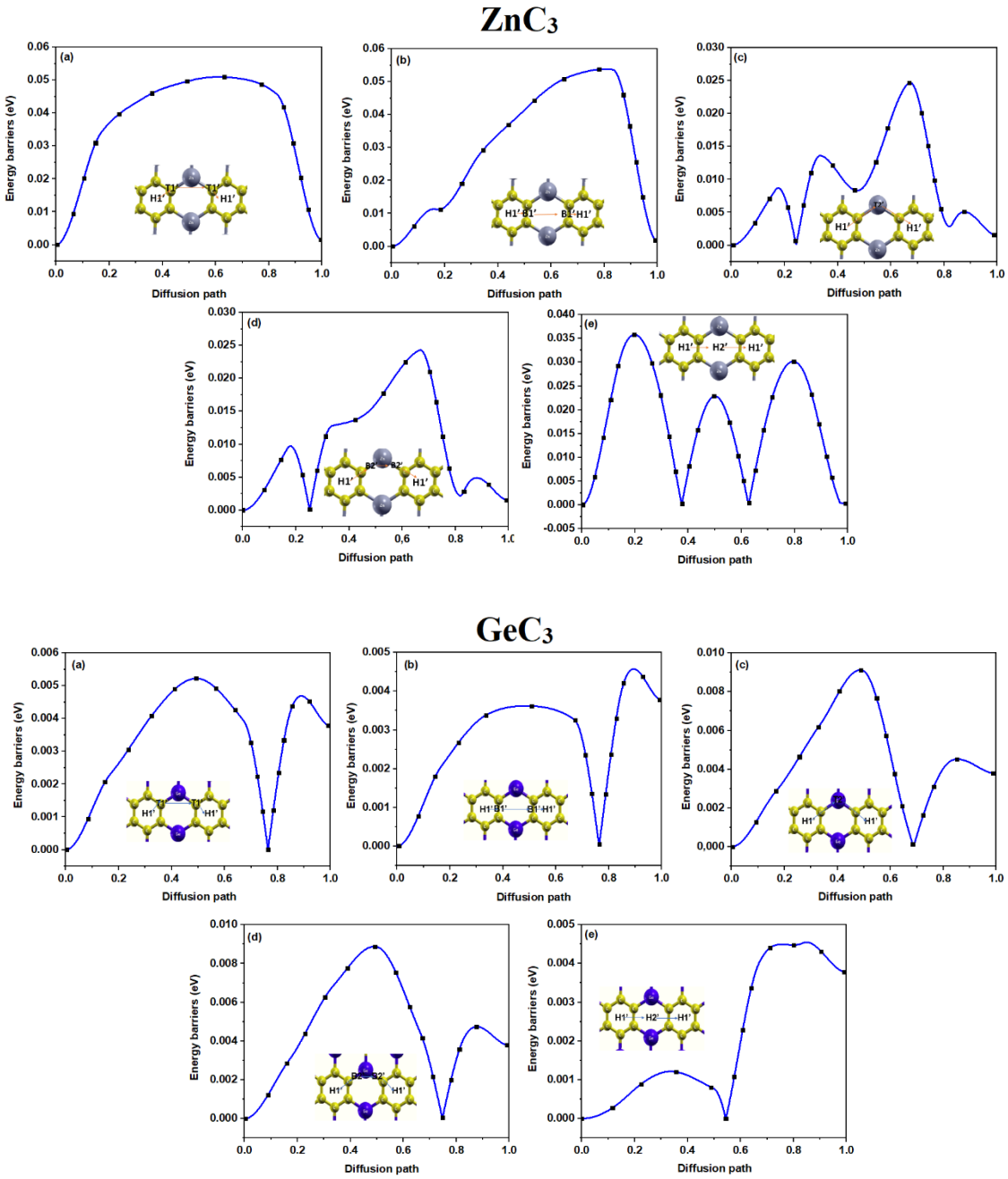

Fig. 4.9: H_2 molecule diffusion path at XC_3 surface from the primary physisorption site to the transition site.

Table 4.5: The energy barriers of H_2 molecule diffusion on XC_3 layers from diverse beginning to ending positions

First state	Primary intermediate state	Second intermediate state	Final state	Activation energy (eV) (BC_3)	Activation energy (eV) (AlC_3)	Activation energy (eV) (ZnC_3)	Activation energy (eV) (GeC_3)
C	**A**	**A**	**C**	0.0064	0.02	0.051	0.0052
C	**B**	**B**	**C**	0.0079	0.0163	0.053	0.0042

C	**G**	**--**	**C**	0.0022	0.0565	0.022	0.0090
C	**H**	**H**	**C**	0.032	0.055	0.023	0.0086
C	**I**	**--**	**C**	0.034	0.0472	0.0357	0.0044

4.7 Conclusion

To summarize, we have carried out computations to study the storage of H_2 at the XC_3 monolayers. Through our findings, we found a strong adsorption of H_2 molecules by a polarization mechanism to the XC_3 monolayers with the mean energy of adsorption of H_2 between -0.20 and -0.35 eV. The diffusion process of our molecule on the substrate shows a low activation energy that allows the molecule to migrate on the surface so easily up to 0.0022 eV, 0.0163 eV, 0.022 eV and 0.0042 eV for the BC_3, AlC_3, ZnC_3, and GeC_3 surfaces respectively. The study revealed a high gravimetric capacity up to 10.51 wt%, 11.80 wt%, 7.73 wt% and 7.25 wt% as a new 2D materials for hydrogen storage. The hydrogenation/dehydrogenation (desorption) temperature reaches 205.33 K, 173.33 K, 215.55 K and 224.25 K of BC_3, AlC_3, ZnC_3, and GeC_3 surfaces respectively. The desorption temperatures of H_2 molecules indicate that the monolayer XC_3 could function as a reversible hydrogen storage substrates. Therefore, the results reveal that the XC_3 monolayers are an efficient and promising reversible hydrogen storage materials with high gravimetric capacity under feasible conditions.

General Conclusion

Conclusion

Because of the finite amount of fossil fuels and its effects on the weather and ecology, the exploration of alternative, clean, abundant and sustainable energy sources is becoming a global priority. Although renewable energies including solar, wind and hydrogen have the ability to satisfy the current energy demand, ongoing issues remain the need to identify materials that are capable of storing and/or transforming energy efficiently and cheaply. The hydrogen provides a neat answer to the crucible of the environment. Being a highly versatile energy carrier, H_2 has the capability to provide a comprehensive, integrated, multi-sectoral, at low cost, clean energy option to help solve the environmental issue and ensure the Earth's energy future. Nonetheless, the mass adoption of economic hydrogen has been slow owing to insufficient motivation as well as the technical challenges involved in storing hydrogen. The goal of this thesis was to enhance hydrogen storage conditions in carbon-based materials, particularly graphene-based materials. According to the literature, it is mentioned that, in the United States Department of Energy (DOE), for hydrogen storage to be industrially effective, the suitable binding energy of hydrogen should be between 0.2 eV and 0.6 eV for each hydrogen molecule. Hence, graphene is not a suitable tank for hydrogen storage applications because of the weak binding energy which out of the range of 0.2 and 0.6 eV/H_2. In the case of physisorption, the VD (volumetric density) depends on the possibility of building compact structures with graphene to improve the chance of being a candidate for hydrogen storage. In the first calculations we examined the physisorption of H_2 molecule on BC_7 structure by first-principles calculations, we have found that the E_{ads} adsorption energy was close to -0.2081 eV, wherein the distance with the highest stability is 3.40 Å. The adsorption of the H_2 molecule at different configurations at BC_7 structure retained its metallic behavior. The investigation of the diffusion paths among the distinct configurations revealed a hydrogen molecule ability to transmit among the sites, that are parted by a low energy barrier of 0.0022 eV. It was demonstrated that the BC_7 layer can adsorb 11 H_2 molecules, having a gravimetric capacity of 10.40 wt%. The hydrogenation/dehydrogenation (desorption) temperature was found as 177.00 K. The H_2 molecule desorption temperatures and gravimetric capacity indicates that the monolayer BC_7 might work as a hydrogen reversible storage substrate. Hence, the findings reveal BC_7 monolayer to be a prospective, effective, reversible and great gravimetric capacity for storing H_2 in feasible conditions. We did the same calculations on BC_3 surface, it was found from the calculations that the adsorption energy is about - 0,3150 eV, whereas the 3.10 Å is the closest stable distance. The density of state calculation shows that upon adsorption of H_2 molecules onto the BC_3 surface, it kept its semiconducting behavior with both methods the Marzarie Vanderbilt and the Tetrahedron method. An investigation of the migration paths between the different positions shown a capability of hydrogen molecule to diffuse between the positions, separated by a small barrier of energy amounting to 2.25 meV. The BC_3 sheet was

demonstrated to possess the capability of adsorbing 11 hydrogen molecules, with a gravimetric capacity of 10.51 wt%, with a desorption temperature of 205.33 K. According to results, the BC_3 sheet can be a very interesting prospect for hydrogen storage. We also have investigated through the first principal calculations the adsorption of hydrogen molecule on AlC_3 monolayer, the calculations appears that the adsorption energy E_{ads} was about -0,2189 eV, where the most stable distance was 2.50 Å. The hydrogen molecule adsorption at various positions on AlC_3 surface maintained its semiconducting character. The examination of the diffusion paths between the various sites indicated an ability of the hydrogen molecule to migrate between the sites, which were spaced by a slight energy barrier of 0.0163 eV. It was shown that AlC_3 monolayer possess the ability to adsorb 16 hydrogen molecules, with 11.8 wt% as gravimetric capacity, as well as a desorption temperature of 173.35 K. Based on the findings, the AlC_3 monolayer may be a promising candidate for hydrogen storage. We have studied the interaction of ZnC_3 substrate and H_2 molecule, the have revealed that the E_{ads} adsorption energy was close to - 0.3169 eV, wherein the distance with the highest stability was 3.30 Å. The adsorption of the H_2 molecule at different configurations at ZnC_3 structure retained its metallic behavior. The investigation of the diffusion paths among the distinct configurations revealed a hydrogen molecule ability to transmit among the sites, that were parted by a low energy barrier of 0.022 eV. It was demonstrated that the ZnC_3 layer can adsorb 17 H_2 molecules, having a gravimetric capacity of 7.73 wt%. The hydrogenation/dehydrogenation (desorption) temperature was found as 215.55 K. The H_2 molecule desorption temperatures and gravimetric capacity indicated that the monolayer ZnC_3 might work as a hydrogen reversible storage substrate. Hence, the findings revealed ZnC_3 monolayer as a prospective, effective, reversible and great gravimetric capacity for storing H_2 in feasible conditions. Finally, we have examined the physisorption of H_2 molecule on GeC_3 structure by first-principles calculations, we have found that the E_{ads} adsorption energy was close to - 0.3628 eV, wherein the distance with the highest stability was 3.30 Å. The adsorption of the H_2 molecule at different configurations at GeC_3 structure retained its semi-metallic behavior. The investigation of the diffusion paths among the distinct configurations revealed a hydrogen molecule ability to transmit among the sites, that were parted by a low energy barrier of 0.0042 eV. It was demonstrated that the GeC_3 layer can adsorb 17 H_2 molecules, having a gravimetric capacity of 7.25 wt%. The hydrogenation/dehydrogenation (desorption) temperature was found as 224.25 K. The H_2 molecule desorption temperatures and gravimetric capacity indicated that the monolayer GeC_3 might work as a hydrogen reversible storage substrate. Hence, the findings revealed GeC_3 monolayer as a prospective, effective, reversible and great gravimetric capacity for storing H_2 in feasible conditions. Due to this finding, we have enhanced the properties of transport, electronics and storage of hydrogen molecule compared with graphene.

Bibliography

[1] United Nations, World Population Prospects 2019, 2019, pp. 49–78.

[2] E. S. Hanley, J. P. Deane, B. P. Gallachóir, Renewable and Sustainable Energy Reviews 2018, 82, 3027–3045.

[3] IEA, Global Energy & CO_2 Statuts Report, tech. rep. March, 2018.

[4] U.S. EIA, Annual Energy Outlook 2019 with projections to 2050 2019, 44, 1–64.

[5] British Petroleum Company, The Editor BP Statistical Review of World Energy 2019.

[6] M. R. Allen, O. P. Dube, W. Solecki, F. Aragón–Durand, W. Cramer, S. Humphreys, M. Kainuma, J. Kala, N. Mahowald, Y. Mulugetta, R. Perez, M. Wairiu, K. Zickfeld, 1-Farming and Context, tech. rep., 2018, pp. 47–92.

[7] R. Tuckett, US EIA - Short-Term Energy Outlook 2018, 1–48.

[8] British Petroleum, BP statistical review of world energy. London, tech. rep., 2018, p. 40.

[9] J. Burck, U. Hagen, F. Marten, N. Höhne, C. Bals, 2019.

[10] L. H. U. W. Abeydeera, J. W. Mesthrige, T. I. Samarasinghalage, Sustainability (Switzerland) 2019, 11, 1–25.

[11] Freeman, Journal of Chemical Information and Modeling 2013, 53, 1689–1699.

[12] IRENA, Hydrogen: a renewable energy perspective, 2019, pp. 1–52.

[13] U.S. Energy Information Administration, 2020.

[14] C. Sealy, Graphene-CNT superstructure holds promise for hydrogen storage, Nano Today. 4 (1) (2009) 6-6.

[15] G. Zini, P. Tartarini, Wind-hydrogen energy stand-alone system with carbon storage: Modeling and simulation, Renewable Energy. 35 (11) (2010) 2461-2467.

[16] I. Lopez-Corral, E. Germán, A. Juan, M. A. Volpe, G. P. Brizuela, Hydrogen adsorption on palladium dimer decorated graphene: a bonding study, international journal of hydrogen energy. 37 (8) (2012) 6653-6665.

[17] J. H. Cho, S. J. Yang, K. Lee, C. R. Park, Si-doping effect on the enhanced hydrogen storage of single walled carbon nanotubes and graphene, international journal of hydrogen energy. 36 (19) (2011) 12286-12295.

[18] L. Yu, X. Pan, X. Cao, P. Hu, X. Bao, Oxygen reduction reaction mechanism on nitrogen-doped graphene: A density functional theory study, Journal of Catalysis. 282 (1) (2011) 183-190.

[19] Y. Gao, N. Zhao, J. Li, E. Liu, C. He, C. Shi, Hydrogen spillover storage on Ca-decorated graphene, International journal of hydrogen energy. 37 (16) (2012) 11835-11841.

[20] L. Hu, X. Hu, X. Wu, C. Du, Y. Dai, J. Deng, Density functional calculation of transition metal adatom adsorption on graphene, Physica B: Condensed Matter. 405 (16) (2010) 3337-3341.

[21] U. Lange, T. Hirsch, V. M. Mirsky, O. S. Wolfbeis, Hydrogen sensor based on a graphene–palladium nanocomposite, Electrochimica Acta. 56 (10) (2011) 3707-3712.

[22] H. P. Zhang, X. G. Luo, X. Y. Lin, X. Lu, Y. Leng, Density functional theory calculations of hydrogen adsorption on Ti-, Zn-, Zr-, Al-, and N-doped and intrinsic graphene sheets, international journal of hydrogen energy. 38 (33) (2013) 14269-14275.

[23] H. P. Zhang, X. G. Luo, X. Y. Lin, X. Lu, Y. Leng, Density functional theory calculations of hydrogen adsorption on Ti-, Zn-, Zr-, Al-, and N-doped and intrinsic graphene sheets, international journal of hydrogen energy. 38 (33) (2013) 14269-14275.

[24] H. Cavendish, Philosophical Transactions of the Royal Society of London 1766, 56, 141–184.

[25] F. G. Brickwedde, Physics Today 1982, 35, 34–39.

[26] M. L. Oliphant, P. Harteck, Rutherford, Transmutation effects observed with heavy hydrogen [1], 1934.

[27] U.S. Department of Energy, Hydrogen Storage | Department of Energy, tech. rep. 1, 2012, n/a.

[28] A. Züttel, Naturwissenschaften 2004, 91, 157–172.

[29] Y. Manoharan, S. E. Hosseini, B. Butler, H. Alzhahrani, B. T. F. Senior, T. Ashuri, J. Krohn, Applied Sciences (Switzerland) 2019, 9, DOI 10 . 3390 / app9112296.

[30] J. O. Abe, A. P. Popoola, E. Ajenifuja, O. M. Popoola, International Journal of Hydrogen Energy 2019, 44, 15072–15086.

[31] A. Sorokowska, P. Sorokowski, P. Hilpert, K. Cantarero, T. Frackowiak, K. Ahmadi, J. D. Pierce Jr, Preferred interpersonal distances: a global comparison, Journal of Cross-Cultural Psychology. 48(4) (2017) 577-592.

[32] US Department of Energy, U.S Drive 2017, 1–29.

[33] DOE Technical Targets for Fuel Cell Systems and Stacks for Transportation Applications | Department of Energy, 2020.

[34] M. M. Whiston, I. L. Azevedo, S. Litster, K. S. Whitefoot, C. Samaras, J. F. Whitacre, Proceedings of the National Academy of Sciences of the United States of America 2019, 116, 4899–4904.

[35] U.S. Department of Energy, 2014, 1–8.

[36] H Barthelemy, M Weber, F Barbier, International Journal of Hydrogen Energy 2017, 42, 7254–7262.

[37] D Mori, K Hirose, International Journal of Hydrogen Energy 2009, 34, 4569–4574.

[38] Linde AG, Cryogenic tanks | Linde Engineering, 2012.

[39] J. R. Travis, D. Piccioni Koch, Journal of Energy Storage 2015, 2, 47–53.

[40] E. D. Bloch, W. L. Queen, R. Krishna, J. M. Zadrozny, C. M. Brown, J. R. Long, Hydrocarbon separations in a metal-organic framework with open iron (II) coordination sites, science. 335(6076), (2012) 1606-1610.

[41] R. Ahluwalia, T. Hua, J.-K Peng, S. Lasher, K. McKenney, J. Sinha, M. Gardiner, International Journal of Hydrogen Energy 2011, 35, 4171–4184.

[42] H. Barthelemy, M. Weber, F. Barbier, International Journal of Hydrogen Energy 2017, 42, 7254–7262.

[43] S. Orimo, Y. Nakamori, J.R. Eliseo, A. Zuttel, C.M. Jensen, Chem. Rev. 107 (2007) 4111–4132.

[44] Y. Kojima, T. Ichikawa, H. Fujii, Complex hydrides, Encyclopedia of Electrochemical Power Sources, in: J. Garche, C. Dyner, P. Moseley, Z. Ogumi, D. Rand, B. Scrosati (Eds.), Elsevier, Amsterdam, vol. 3, 2009.

[45] V.P. Balema, J.W. Wiench, K.W. Dennis, M. Pruski, V.K. Pecharsky, J. Alloys Compd. 329 (2001) 108–114.

[46] J. Wang, A.D. Ebner, J.A. Ritter, J. Am. Chem. Soc. 128 (2006) 5949–5954.

[47] Y. Kojima, Y. Kawai, T. Haga, M. Matsumoto, A. Koiwai, J. Alloys Compd. 441 (2007) 189–191.

[48] B. Bogdanovic, M. Schwickardi, J. Alloys Compd. 253 (1997) 1–9.

[49] R.A. Zidan, S. Takara, A.G. Hee, C.M. Jensen, J. Alloys Compd. 285 (1999) 119–122.

[50] B. Bogdanovic, R.A. Brand, A. Marjanovic, M. Schwickardi, J. Tolle, J. Alloys Compd. 302 (2000) 36–58.

[51] H. Morioka, K. Kakizaki, S.-C. Chung, A. Yamada, J. Alloys Compd. 353 (2003) 310–314.

[52] M. Fichtner, O. Fuhr, O. Kircher, J. Alloys Compd. 356 (2003) 418–422.

[53] A. Züttel, P. Wenger, S. Rentsch, P. Sudan, P. Mauron, C. Emmenegger, J. Power Sources 118 (2003) 1–7.

[54] A. Züttel, S. Rentsch, P. Fischer, P. Wenger, P. Sudan, P. Mauron, C. Emmenegger, J. Alloys Compd. 356 (2003) 515–520.

[55] A. Züttel, Mitig. Adapt. Strat. Glob. Change 12 (2007) 343–365.

[56] J. H. Hubbell, S. M. Seltzer, National Institute of Standards and Technology, Physics National Report No. NISTIR. (1995) 5632.

[57] Y. Nakamori, H. Li, K. Miwa, S. Towata, S. Orimo, Mater. Trans. 47 (2006) 1898–1901.

[58] Y. Nakamori, K. Miwa, A. Ninomiya, H.W. Li, N. Ohba, S. Towata, A. Zuttel, S. Orimo, Phys. Rev. B 74 (2006).

[59] M. Dornheim in Thermodynamics - Interaction Studies - Solids, Liquids and Gases, InTech, 2011.

[60] Principi, G.; Agresti, F.; Maddalena, A.; Lo Russo, S. Energy 2009, 34, 2087–2091.

[61] Yang, J.; Sudik, A.; Wolverton, C.; Siegel, D. J. Chem. Soc. Rev. 2010, 39, 656–675.

[62] Gross, K. J.; Thomas, G. J.; Jensen, C. M. J. Alloys Compd. 2002, 330, 683–690.

[63] Bogdanovic, B.; Sandrock, G. MRS Bull. 2002, 27, 712–716.

[64] Sakintuna, B.; Lamari-Darkrim, F.; Hirscher, M. Int. J. Hydrog. Energy 2007, 32, 1121–1140.

[65] Jain, I. P.; Jain, P.; Jain, A. J. Alloys Compd. 2010, 503, 303–339.

[66] Chen, P.; Xiong, Z. T.; Luo, J. Z.; Lin, J. Y.; Tan, K. L. Nature 2002, 420, 302–304.

[67] Al-Kukhun, A.; Hwang, H. T.; Varma, A. Ind. Eng. Chem. Res. 2011, 50, 8824–8835.

[68] Uribe, F. A.; Gottesfeld, S.; Zawodzinski, T. A. J. Electrochem. Soc. 2002, 149, A293–A296.

[69] Zhang, X. Y.; Pasaogullari, U.; Molter, T. Int. J. Hydrog. Energy 2009, 34, 9188–9194.

[70] Kissinger, H. E. Anal. Chem. 1957, 29, 1702–1706.

[71] H. T. Hwang, A. Varma, Hydrogen Storage Methods for Fuel Cell Vehicles: Current Status. (2015).

[72] M. A. CHIKDENE, 1989, 22.

[73] A. Züttel, Naturwissenschaften 2004, 91, 157–172.

[74] M. G. Nijkamp, J. E. Raaymakers, A. J. Van Dillen, K. P. De Jong, Applied Physics A: Materials Science and Processing 2001, 72, 619–623.

[75] U.S. Department of Energy, Hydrogen Storage | Department of Energy, tech. rep. 1, 2012, n/a.

[76] Q. Lai, Y. Sun, T. Wang, P. Modi, C. Cazorla, U. B. Demirci, J. R. Ares Fernandez, F. Leardini, K. F. Aguey-Zinsou, Advanced Sustainable Systems 2019, 3, 1–64.

[77] J. K. Bristow, J. M. Skelton, K. L. Svane, A. Walsh, J. D. Gale, Physical Chemistry Chemical Physics 2016, 18, 29316–29329.

[78] V. R. Bakuru, M. E. DMello, S. B. Kalidindi, ChemPhysChem 2019, 20, 1177– 1215.

[80] J. Liang, Y. B. Huang, R. Cao, Coordination Chemistry Reviews 2019, 378, 32–65.

[81] T. B. Lee, D. Kim, D. H. Jung, S. B. Choi, J. H. Yoon, J. Kim, K. Choi, S. H. Choi, Catalysis Today 2007, 120, 330–335.

[82] A. C. Dillon, M. J. Heben, Applied Physics A: Materials Science and Processing 2001, 72, 133–142.

[83] A. C. Dillon, K. M. Jones, T. A. Bekkedahl, C. H. Kiang, D. S. Bethune, M. J. Heben, Nature 1997, 386, 377–379.

[84] Y. Basdogan, S. Keskin, CrystEngComm 2015, 17, 261–275.

[85] C. W. Huang, H. C. Wu, Y. Y. Li, Separation and Purification Technology 2007, 58, 219–223.

[86] S. Isobe, T. Ichikawa, J. I. Gottwald, E. Gomibuchi, H. Fujii in Journal of Physics and Chemistry of Solids, Vol. 65, Pergamon, 2004, pp. 535–539.

[87] A. Chambers, C. Park, R. T. K. Baker, N. M. Rodriguez, Journal of Physical Chemistry B 1998, 102, DOI 10.1021/jp980114l.

[88] M. Hirscher, M. Becher, M. Haluska, A. Quintel, V. Skakalova, Y. M. Choi, U. Dettlaff-Weglikowska, S. Roth, I. Stepanek, P. Bernier, A. Leonhardt, J. Fink in Journal of Alloys and Compounds, Vol. 330-332, Elsevier, 2002, pp. 654–658.

[89] T. Heine, L. Zhechkov, G. Seifert, Physical Chemistry Chemical Physics 2004, 6, 980–984.

[90] H. Imamura, N. Sakasai, T. Fujinaga, Journal of Alloys and Compounds 1997, 253-254, 34–37.

[91] A. Curia, M. Aguerrido, K. Langohr, G. Hough, Survival analysis applied to sensory shelf life of yogurts–I: Argentine formulations, Journal of food science. 70(7) (2005) s442-s445.

[92] R. Ströbel, J. Garche, P. T. Moseley, L. Jörissen, G. Wolf, Journal of Power Sources 2006, 159, 781–801.

[93] M. Hirscher, B. Panella, Journal of Alloys and Compounds 2005, 404-406, 399– 401.

[94] Y. Xia, Z. Yang, Y. Zhu, Journal of Materials Chemistry A 2013, 1, 9365–9381.

[95] H. Kabbour, T. F. Baumann, J. H. Satcher, A. Saulnier, C. C. Ahn, Chemistry of Materials 2006, 18, 6085–6087.

[96] O. V. Pupysheva, A. A. Farajian, B. I. Yakobson, Nano Letters 2008, 8, 767–774.

[97] N. S. Venkataramanan, A. Suvitha, H. Mizuseki, Y. Kawazoe, 2012, 43.

[98] C. Liu, Y. Chen, C. Z. Wu, S. T. Xu, H. M. Cheng, Carbon 2010, 48, 452–455.

[99] H. M. Cheng, Q. H. Yang, C. Liu, Carbon 2001, 39, 1447–1454.

[100] Lee, C., Wei, X., Kysar, J.W., Hone, J., 2008. Measurement of the elastic properties and intrinsic strength of monolayer graphene. Science 321, 385–388.

[101] Novoselov, K.S., Geim, A.K., Morozov, S.V., et al., 2005. Two-dimensional gas of massless Dirac fermions in graphene. Nature 438, 197–200.

[102] Zhang, Y., Small, J.P., Amori, M.E.S., Kim, P., 2005. Electric field modulation of galvanomagnetic properties of mesoscopic graphite. Physical Review Letters 94, 176803.

[103] PapageorgiouIan, D.G., Kinloch, A., Young, R.J., 2017. Mechanical properties of graphene and graphene-based nanocomposites. Progress in Materials Science 90, 75–127.

[104] Bolotina, K.I., Sikes, K.J., Jianga, Z., et al., 2008. Ultrahigh electron mobility in suspended graphene. Solid State Communications 146, 351–355.

[105] Wang, L., Meric, I., Huang, P.Y., et al., 2013. One dimensional electrical contact to a two-dimensional material. Science 342, 614.

[106] G. Zini, P. Tartarini, Wind-hydrogen energy stand-alone system with carbon storage: Modeling and simulation, Renewable Energy. 35 (11) (2010) 2461-2467.

[107] C. Sealy, Graphene-CNT superstructure holds promise for hydrogen storage, Nano Today. 4 (1) (2009) 6-6.

[108] J. H. Cho, S. J. Yang, K. Lee, C. R. Park, Si-doping effect on the enhanced hydrogen storage of single walled carbon nanotubes and graphene, international journal of hydrogen energy. 36 (19) (2011) 12286-12295.

[109] L. Yu, X. Pan, X. Cao, P. Hu, X. Bao, Oxygen reduction reaction mechanism on nitrogen-doped graphene: A density functional theory study, Journal of Catalysis. 282 (1) (2011) 183-190.

[110] V. Tozzini and V. Pellegrini, J. Phys. Chem. C, 115 25523 (2011)

[111] S. Patchkovskii J S. Tse, S N Yurchenko, L Zhechkov, T Heine, and G Seifer. PNAS 102, 10439 (2005) [100] A Zuttel P. Sudan, Ph. Mauron, T. Kiyobayashi, Ch. Emmenegger, L. Schlapbach, Int J of Hydrogen Energy, 27, 203-2012 (2002)

[112] Y Miura, W Dino, H Nakanishi, J Appl Phys, 93, 3395 (2003)

[113] T. Zecho, A Güttler, X Sha, B Jackson, and J KüppersJ. Chem. Phys. 117, 8486 (2002)

[114] L. Jeloaica, V. Sidis, Chem. Phys. Lett. 300, 157 (1999)

[115] X. Sha, B. Jackson, Surf. Sci. 496, 318 (2002)

[116] Y Ferro, F. Marinelli, A Allouche, J Chem Phys, 116, 8124 (2002)

[117] N Rougeau, D Teillet-Billy, V Sidis, Chem Phys Lett 431, 135-138 (2006)

[118] Z Sljivancanin, E Rauls, L Hornekaer, W Xu, F besenbacher and B Hammer, J Chem Phys 131, 084706 (2009)

[119] L. Hornekaer Ž. Šljivančanin, W. Xu, R. Otero, E. Rauls, I. Stensgaard, E. Lægsgaard, B. Hammer, and F. Besenbacher. Phys. Rev. Lett. 96, 156104 (2006)

[120] L. Hornekaer, E. Rauls, W. Xu, S Šljivančanin, R. Otero, I. Stensgaard, E. Lægsgaard, B. Hammer, and F. Besenbacher.. Phys. Rev. Lett. 97, 186102 (2006)

[121] A. Andree, M Le Lay, T Zecho, J Küpper Chem. Phys. Lett. 425, 99 (2006)

[122] L. Hornekaer, W. Xu, R. Otero, E. Lægsgaard, F. Besenbacher. Chem. Phys. Lett. 446, 237 (2007)

[123] D Stojkovic, P Zhang, P E. Lammert, and V H. Crespi, Phys Rev B 68, 195406 (2003)

[124] S Casolo, O M Løvvik, R Martinazzo, and G F Tantardini, J Chem Phys 130, 054704 (2009)

[125] T Roman W A Dino, H Nakanishi, H Kasai, T Sugimoto, K Tange, Carbon 45 203-228 (2007)

[126] Y Ferro, D. Teillet-Billy, N. Rougeau, V. Sidis, S. Morisset, and A Allouche Phys Rev B 78, 085417 (2008)

[127] R. Balog, B Jørgensen, J Wells, E Lægsgaard, P Hofmann, F Besenbacher and L Hornekær J. Am. Chem. Soc. 131, 8744 (2009)

[128] N.P. Guisinger, G M Rutter, J N Crain, P. N. First and J A. Stroscio Nano Letters 9, 1462 (2009)

[129] J.O Sofo A S Chaudhari, G D Barber, Phys Rev B, 75 153401 (2007)

[130] D.C. Elias R. R. Nair, T. M. G. Mohiuddin, S. V. Morozov, P. Blake, M. P. Halsall, A. C. Ferrari, D. W. Boukhvalov, M. I. Katsnelson, A. K. Geim, and K. S. Novoselov Science 323 610 (2009)

[131] R. Balog, B Jørgensen, L Nilsson, M Andersen, E Rienks, M Bianchi, M Fanetti, E Lægsgaard, A Baraldi, S Lizzit, Z Sljivancanin, F Besenbacher, B Hammer, T G. Pedersen, P Hofmann and L Hornekær Nat. Mat. 9, 315 (2010)

[132] V. Tozzini, and V. Pellegrini, Phys. Rev. B 81, 113404 (2010)

[133] P. Sessi, J R. Guest, M Bode and N P. Guisinger Nano letters 9, 4343 (2009)

[134] V. Tozzini, V. Pellegrini, Prospects for hydrogen storage in graphene, Physical Chemistry Chemical Physics. 15(1) (2013) 80-89.

[135] L. W. Jones, "Toward a liquid hydrogen fuel economy". University of Michigan. 13 March 1970, http://deepblue.lib.umich.edu/bitstream/ 2027.42/5800/5/bac5758.0001.001.pdf.

[136] B. Ulf, "Does a Hydrogen Economy Make Sense?" Proceedings of the IEEE, Vol. 94, No. 10, October 2006.

[137] D. R. Hartree, Mathematical Proceedings of the Cambridge Philosophical Society 1928, 24, 111–132.

[138] J. C. Slater, Physical Review 1928, 32, 339–348.

[139] J. A. Gaunt, Mathematical Proceedings of the Cambridge Philosophical Society 1928, 24, 328–342.

[140] J. C. Slater, Note on hartree's method [5], 1930.

[141] V. Fock, Zeitschrift für Physik 1930, 61, 126–148.

[142] V. Fock, Zeitschrift für Physik 1930, 62, 795–805.

[143] L. H. Thomas, Proc. Cambridge Phil. Roy. Soc. 23, 542 (1927).

[144] E. Fermi, Rend. Accad. Naz. Lincei 6, 602 (1927).

[145] P. A. M. Dirac, Proc. Cambridge Phil. Roy. Soc. 26, 376 (1930).

[146] E. Teller, Rev. Mod. Phys. 34, 627 (1962).

[147] P. Hohenberg and W. Kohn, Phys. Rev. 136, B864 (1964).

[148] M. Levy, Proc. Nat. Acad. Sci. USA 76, 6062 (1979).

[149] R. O. Jones and O. Gunnarsson, Rev. Mod. Phys. 61, 689 (1989).

[150] N. D. Mermin, Phys. Rev. 137, A1441 (1965).

[151] E. Runge and E. K. U. Gross, Phys. Rev. Lett. 52, 997 (1984).

[152] W. Kohn and L. J. Sham, Phys. Rev. 140: A1133 (1965).

[153] D. R. Hartree, Proc. Cam. Phil. Soc. 24, 89 (1928).

[154] V. Z. Fock, Z. Phys. 61, 209 (1930).

[155] M. Y. Song, D. R. Mumm, S. N. Kwon, S. H. Hong, and J. S. Bae, J. Alloys Compd. 416, 239(2006).

[156] G. Barkhordarian, T. Klassen, and R. Bormann, J. Phys. Chem. B 110, 11020(2006).

[157] T. Vegge, L. S. Hedegaard-Jensen, J. Bonde, T. R. Munter, and J. K. Nørskov, J. Alloys Compd. 386, 1(2005).

[158] A. J. Du, S. C. Smith, X. D. Yao, and G. Q. Lu, J. Phys. Chem. B 110, 21747(2006).

[159] W. P. Kalisvaart, P. Vermeulen, O. Lyedovskykh, D. Danilov, P. H. L. Notten, J. Alloys Compd. 446, 648 (2007).

[160] W. P. Kalisvaart, H. J. Wondergem, A.F. Bakker, P. H. L. Notten, J. Mater. Res. 22, 1640 2007).

[161] W. P. Kalisvaart, M. Latroche, F. Cuevas, P. H. L. Notten, J. Solid State Chem. 181, 1141(2008).

[162] N. W. Ashcroft and N. D. Mermin, Solid State Physics (Thomson Learning, Inc., 1976).

[163] C. Kittel, Introduction to Solid State Physics (New York: John Wiley & Sons, Inc., 1996).

[164] D. R. Hamann, M. Schl¨uter, and C. Chiang, Phys. Rev. Lett. 43, 1494 (1979).

[165] G. B. Bachelet, D. R. Hamann, and M. Schl¨uter, Phys. Rev. B 26, 4199 (1982).

[166] N. Troullier and J. L. Martins, Phys. Rev. B 43, 1993 (1991).

[167] D. Vanderbilt, Phys. Rev. B 41, 7892 (1990).

[168] K. Laasonen, A. Pasquarello, R. Car, C. Lee, and D. Vanderbilt, Phys. Rev. B 47, 10142 (1993).

[169] P. E. Bl¨ochl, Phys. Rev. B 50, 17953 (1994).

[170] G. Kresse and D. Joubert, Phys. Rev. B 59, 1758 (1999).

[171] L. Malakkal, B. Szpunar, J. C. Zuniga, R. K. Siripurapu, J. A. Szpunar, An interface to quantum espresso, In Proceedings of the 3rd World Congress on Integrated Computational Materials Engineering (ICME 2015) (pp. 155-162), Springer, Cham. (2015).

[172] P Giannozzi, O Andreussi, T Brumme, O Bunau, M. B. Nardelli, M Calandra, R Car, C Cavazzoni, D Ceresoli, M Cococcioni, N Colonna, I Carnimeo, A. D. Corso, S de Gironcoli, P Delugas, R. A. DiStasio, A Ferretti, A Floris, G Fratesi, G Fugallo, R Gebauer, U Gerstmann, F Giustino, T Gorni, J Jia, M Kawamura, H.-Y. Ko, A Kokalj, E Küçükbenli, M Lazzeri, M Marsili, N Marzari, F Mauri, N. L. Nguyen, H.-V. Nguyen, A Otero-de-la Roza, L Paulatto, S Poncé, D Rocca, R Sabatini, B Santra, M Schlipf, A. P. Seitsonen, A Smogunov, I Timrov, T Thonhauser, P Umari, N Vast, X Wu, S Baroni, Journal of Physics: Condensed Matter 2017, 29, 465901.

[173] S. Baroni, P. Giannozzi, A. Testa, Physical Review Letters 1987, 59, 2662–2665.

[174] H. J. Monkhorst and J. D. Pack, Phys. Rev. B 13, 5188 (1976).

[175] S. Er, Hydrogen storage materials: a first-principles study. (2009).

[176] J. W. Gibbs, Elementary Principles in Statistical Mechanics (C. Scribner's sons, 1902).

[177] Y. Marcus, M.J. Kamlet, W. Taft, Linear solvation energy relationships: standard molar Gibbs free energies and enthalpies of transfer of ions from water into nonaqueous solvents, The Journal of Physical Chemistry. 92 (12) (1988) 3613-3622.

[178] S.V. Alapati, J.K. Johnson, D.S. Sholl, Identification of destabilized Metal Hydrides for Hydrogen Storage Using First Principles Calculations, The Journal of Physical Chemistry B. 110(17) (2006) 8769-8776.

[179] Wurmser, R., & Filitti-Wurmser, S. (1950). L'énergie de formation des complexes dissociables enzyme-substrat et antigène-anticorps. Biochimica et Biophysica Acta, 4, 238-243.

[180] Gerl, M. (1970). Energie de formation de monolacunes dans les metaux de transition. Journal of Physics and Chemistry of Solids, 31(2), 315-319.

[181] Gerl, M. (1970). Energie de formation de monolacunes dans les metaux de transition. Journal of Physics and Chemistry of Solids, 31(2), 315-319.

[182] P. Atkins and J. de Paula, Atkins' Physical Chemistry (New York: Oxford University Press Inc., 2002).

[183] H. J´onsson, G. Mills, and K. W. Jacobsen, Nudged Elastic Band Method for Finding Minimum Energy Paths of Transitions, in Classical and Quantum Dynamics in Condensed Phase Simulations (Singapore: World Scientific, 1998).

[184] G. Henkelman and H. J´onsson, J. Chem. Phys. 113, 9978 (2000).

[185] G. Henkelman, B. P. Uberuaga, and H. J´onsson, J. Chem. Phys. 113, 9901 (2000).

[186] D. Sheppard, R. Terrell, and G. Henkelman, J. Chem. Phys. 128, 134106 (2008).

[187] R. A. Olsen, G. J. Kroes, G. Henkelman, A. Arnaldsson, and H. J´onsson, J. Chem. Phys. 121, 9776 (2004).

[188] R. S. Mulliken, J. Chem. Phys. 23, 1833 (1955).

[189] J. Meister and W. H. E. Schwarz, J. Phys. Chem. 98, 8245 (1994).

[190] R. Bader, Atoms in Molecules: A Quantum Theory. (USA: Oxford University Press, 1994).

[191] F. L. Hirshfeld, Theor. Chim. Acta 44, 129 (1977).

[192] G. Henkelman, A. Arnaldsson, and H. J´onsson, Comput. Mater. Sci. 36, 354 (2006).

[193] E. Sanville, S. D. Kenny, R. Smith, and G. Henkelman, J. Comput. Chem. 28, 899 (2007).

[194] J. E. Lowther, Potential super-hard phases and the stability of diamond-like boron–carbon structures, Journal of Physics: Condensed Matter. 17 (21) (2005) 3221

[195] P. Giannozzi, S. Baroni, N. Bonini, M. Calandra, R. Car, C. Cavazzoni, R.M. Wentzcovitch, QUANTUM ESPRESSO: a modular and open-source software project for quantum simulations of materials, Journal of physics: Condensed matter, 21(39) (2009) 395502.

[196] P. E. Blochl, Projector augmented-wave method, Phys. Rev. B, 50 (24) (1994) 17953.

[197] G. Kresse, D. Joubert, From ultrasoft pseudopotentials to the projector augmented-wave method, Physical review b. 59(3) (1999) 1758.

[198] P. E. Blöchl, O. Jepsen, O. K. Andersen, Improved tetrahedron method for Brillouin-zone integrations. Physical Review B, 49(23), 16223.

[199] A. Kokalj, Computer graphics and graphical user interfaces as tools in simulations of matter at the atomic scale, Comput. Mater. Sci. 28 (2) (2003) 155–168.

[200] K. Momma, F. Izumi, VESTA 3 for three-dimensional visualization of crystal, volumetric and morphology data, J. Appl. Crystallogr. 44 (6) (2011) 1272–1276.

[201] G. Henkelman, B. P. Uberuaga, H. Jonsson, ´ A climbing image nudged elastic band method for finding saddle points and minimum energy paths, J. Chem. Phys. 113 (22) (2000) 9901–9904.

[202] J. P. Perdew, Y. Wang, Phys. Rev. B: Condens, Matter Mater. Phys, (1992).

[203] H. Zhang, W. X. Li, First-principles investigation of surface and subsurface H adsorption on Ir (111), The Journal of Physical Chemistry C. 113(51) (2009) 21361-21367.

[204] S. Grimme, Semiempirical GGA-type density functional constructed with a long-range dispersion correction, Journal of computational chemistry. 27(15) (2006) 1787-1799.

[205] A. Hashmi, M. U. Farooq, I. Khan, J. Son, J. Hong, Ultra-high capacity hydrogen storage in a Li decorated two-dimensional C 2 N layer, Journal of Materials Chemistry A. 5(6) (2017) 2821-2828.

[206] J. Labrousse, K. Belasfar, A. El Kenz, A. Benyoussef, Ultra-high capacity of physisorption of hydrogen molecule on AlC3 monolayer: First-principles calculations, FlatChem. (2021) 100291

[207] K. I. M. Rojas, C. V. Al Rey, J. L. Moreno, M. David, N. B. Arboleda Jr, Ca and K decorated germanene as hydrogen storage: An ab initio study. international journal of hydrogen energy. 43(9) (2018) 4393-4400.

[208] J. Labrousse, K. Belasfar, A. El Kenz, A. Benyoussef, Hydrogen molecule capacity physisorption on BC3 monolayer: First-principles calculations, Diamond and Related Materials. 119 (2021) 108583.

[209] C. M. Ramos-Castillo, J. U. Reveles, M. E. Cifuentes-Quintal, R. R. Zope, R. De Coss, Ti4-and Ni4-doped defective graphene nanoplatelets as efficient materials for hydrogen storage, The Journal of Physical Chemistry C. 120(9) (2016) 5001-5009.

[210] S.V. Alapati, J.K. Johnson, D.S. Sholl, Identification of destabilized Metal Hydrides for Hydrogen Storage Using First Principles Calculations, The Journal of Physical Chemistry B. 110(17) (2006) 8769-8776.

[211] D. C. Elias, R. R. Nair, T. M. G. Mohiuddin, S. V. Morozov, P. Blake, M. P. Halsall, K. S. Novoselov, Control of graphene's properties by reversible hydrogenation: evidence for graphane, Science. 323(5914) (2009) 610-613.

[212] DOE Technical Targets for Fuel Cell Systems and Stacks for Transportation Applications | Department of Energy, 2020.

[213] X. L. Lei, G. Liu, M. S. Wu, B. Xu, C. Y. Ouyang, B. C. Pan, Hydrogen storage on calcium-decorated BC7 sheet: a first-principles study, International journal of hydrogen energy. 39 (5) (2014) 2142-2148.

[214] J. Joo, H. Kim, S.S. Han, Volume shrinkage of a metal–organic framework host induced by the dispersive attraction of guest gas molecules, Physical Chemistry Chemical Physics. 15 (43) (2013) 18822-18826.

[215] F. Costanzo, P. L. Silvestrelli, F. Ancilotto, Physisorption, diffusion, and chemisorption pathways of H2 molecule on graphene and on (2, 2) carbon nanotube by first principles calculations, Journal of chemical theory and computation. 8(4) (2012) 1288-1294.

[216] J. Petucci, C. LeBlond, M. Karimi, G. Vidali, Diffusion, adsorption, and desorption of molecular hydrogen on graphene and in graphite, The Journal of chemical physics. 139(4) (2013) 044706

[217] E.H. Song, S.H. Yoo, J. J. Kim, S.W. Lai, Q. Jiang, S.O. Cho, External electric field induced hydrogen storage/release on calcium-decorated single-layer and bilayer silicene, Physical Chemistry Chemical Physics. 16 (43) (2014) 23985-23992.

[218] J.D. Pack, H.J. Monkhorst, " Special points for Brillouin-zone integrations"—a reply, Physical Review B. 16 (4) (1977) 1748.

[219] J. P. Perdew, K. Burke, M. Ernzerhof, Generalized gradient approximation made simple, Phys. Rev. Lett. 77 (18) (1996) 3865.

[220] Y. Li, T. Hussain, A. De Sarkar, R. Ahuja, Hydrogen storage in polylithiated BC3 monolayer sheet, Solid state communications. 170 (2013) 39-43.

[221] Z.M. Ao, Q. Jiang, R.Q. Zhang, T.T. Tan, S. Li, Al doped graphene: a promising material for hydrogen storage at room temperature, Journal of Applied Physics. 105 (7) (2009) 074307.

[222] J. Gu, X. Zhang, L. Fu, A. Pang, Study on the hydrogen storage properties of the dual active metals Ni and Al doped graphene composites, International Journal of Hydrogen Energy. 44 (12) (2019) 6036-6044.

[223] C. M. Ramos-Castillo, J. U. Reveles, M. E. Cifuentes-Quintal, R. R. Zope, R. De Coss, Ti4-and Ni4-doped defective graphene nanoplatelets as efficient materials for hydrogen storage, The Journal of Physical Chemistry C. 120(9) (2016) 5001-5009.

Abstract

Hydrogen provides a clean, abundant, and most energy-efficient fuel without emissions when operated in a fuel cell or combustion engine, making it an ideal fuel. Nevertheless, hydrogen's enormous potential remains unrealized, mainly because of the problems associated with hydrogen storage and production on a commercial scale. There are many ways to store hydrogen, carbon-based materials being one of them, we chose to improve the transport, electronic and storage properties of graphene by building compact structures with graphene sheets. Physisorption of H_2 molecule on BC_7, BC_3, AlC_3, ZnC_3, and GeC_3, shows a large gravimetric capacity of 10.40 wt%, 10.51 wt%, 11.8 wt%, 7.73 wt% and 7.25 wt%, respectively. The hydrogenation/dehydrogenation (desorption) temperature for the previous surfaces was found as 177.00 K, 205.33 K, 173.35 K, 215.55 K, 224.25 K, respectively. The H_2 molecule desorption temperatures and gravimetric capacity indicates that the monolayers BC_7, BC_3, AlC_3, ZnC_3, and GeC_3 might work as a hydrogen reversible storage substrates. Hence, the findings reveal the previous substrates monolayers to be a prospective, effective, reversible and great gravimetric capacity for storing H_2 in feasible conditions.

Keywords : Monolayer, Hydrogen adsorption, First-principles calculation, Desorption temperature, Gravimetric capacity, Activation energy.

Résumé

Lorsqu'il est utilisé dans une pile à combustible ou un moteur à combustion, l'hydrogène est un combustible propre, abondant et très efficace sur le plan énergétique, sans émissions, ce qui en fait un combustible idéal. Néanmoins, l'énorme potentiel de l'hydrogène reste inexploité, principalement en raison des problèmes liés au stockage et à la production d'hydrogène à l'échelle commerciale. Il existe de nombreuses façons de stocker l'hydrogène, les matériaux à base de carbone étant l'une d'entre elles, nous avons choisi d'améliorer les propriétés de transport, d'électronique et de stockage du graphène en construisant des structures compactes avec des feuilles de graphène. La physisorption de la molécule d'H_2 sur BC_7, BC_3, AlC_3, ZnC_3, et GeC_3, montre une grande capacité gravimétrique de 10,40 % en poids, 10,51 % en poids, 11,8 % en poids, 7,73 % en poids et 7,25 % en poids, respectivement. La température d'hydrogénation/déshydrogénation (désorption) pour les surfaces précédentes a été trouvée à 177,00 K, 205,33 K, 173,35 K, 215,55 K, 224,25 K, respectivement. Les températures de désorption des molécules d'H_2 et la capacité gravimétrique indiquent que les monocouches BC_7, BC_3, AlC_3, ZnC_3 et GeC_3 pourraient fonctionner comme des substrats de stockage réversible de l'hydrogène. Par conséquent, les résultats révèlent que les monocouches de substrats précédentes constituent un moyen prospectif, efficace, réversible et de grande capacité gravimétrique pour le stockage de l'hydrogène dans des conditions réalisables.

Mots-clés : Monocouche, adsorption d'hydrogène, calcul des premiers principes, température de désorption, capacité gravimétrique, énergie d'activation.